Smith, B., Jordan, M., Steinberger, B., Puskas, C., Farell, J., Waite, G., Husen, S., O'Connell, R. J., Klingele, E. (2009): Geodynamics of the Yellowstone hotspot and mantle plume: Seismic and GPS imaging, kinematics and mantle flow. - Journal of Volcanology and Geothermal Research, 188, 1-3, 26-56

DOI: 10.1016/j.jvolgeores.2009.08.020

Elsevier Editorial System(tm) for Journal of Volcanology and Geothermal Research
Manuscript Draft

Manuscript Number: VOLGEO2707

Title: Geodynamics of the Yellowstone Hotspot and Mantle Plume: Seismic and GPS Imaging, Kinematics, Mantle Flow

Article Type: Review Article

Keywords: mantle plume; tomography; volcanism; earthquakes; dynamics; intraplate; kinematics; convection; hotspot; plume; Yellowstone; Snake River Plain

Corresponding Author: Professor Robert B. Smith, PhD

Corresponding Author's Institution: University of Utah

First Author: Robert B. Smith, PhD

Order of Authors: Robert B. Smith, PhD; Michael Jordan; Bernhard Steinberger; Christine M Puskas; Jamie Farrell; Gregory P Waite; Stephan Husen; Wu-Lung Chang; Richard O'Connell

Abstract: The Yellowstone hotspot resulted from interaction of a mantle plume with the overriding North America plate highly modifying the lithosphere by magmatic-tectonic processes and producing the 17 Ma Yellowstone-Snake River Plain (YSRP) volcanic system. The accessibility of the YSRP has allowed large-scale geophysical experiments to seismically image the hotspot and to evaluate its kinematic and dynamic properties using geodetic measurements. Tomography reveals a Yellowstone crustal magma body with 8-15% melt that is fed by an upper-mantle plume extending from 80 km to 660 km deep and tilting 60° west. Contemporary deformation of the Yellowstone caldera is dominated by SW-extension at up to ~3 mm/yr, a fourth of the total Basin-Range opening rate, but with superimposed volcanic uplift and subsidence at decade scales, averaging ~2 cm/yr and unprecedented caldera uplift from 2004-2008 at up to 7 cm/yr. Convection models reveal eastward upper-mantle flow beneath Yellowstone at relatively high rates of 5 cm/yr and opposite in direction to the overriding N. American Plate. This strong flow deflects the ascending plume melt into a tilted configuration, i.e., the plume is caught in a mantle "wind". Dynamic models of the Yellowstone plume revealed relatively low excess temperatures, up to 120°K, with up to 1.5% melt, properties consistent with a weak buoyancy flux of ~0.25 Mg/s. The flux is several times smaller than for oceanic plumes, but it produced a ~600-km wide topographic ~300-m high swell. Employing the plume-geometry we extrapolated the location of the Yellowstone mantle-source southwestward to its initial position at 17 million years beneath eastern Oregon and the southern edge of the LIP Columbia Plateau basalt field suggesting a common origin. Our model suggests that the original plume head rose vertically behind the subducting Juan de Fuca plate, but at ~12 Ma it lost the protection of the subducting plate and encountered cooler, thicker continental lithosphere and became affected by the eastward upper-mantle flow. Regionally, excess gravitation potential energy of the swell drives the SW motion of the YSRP lithosphere that becomes part of a general clockwise rotation pattern of intraplate western U.S. tectonism. Our models thus demonstrate that plume-plate processes of the YSRP have

"continentalized" oceanic lithosphere enhancing intraplate extension and highly modifying topography, deep into the continental interior. Our results demonstrate that the dynamic properties of the Yellowstone hotspot deserved its recognition as a "window into the Earth's interior".

# Geodynamics of the Yellowstone Hotspot and Mantle Plume: Seismic and GPS Imaging, Kinematics, Mantle Flow

Smith[a], Robert B., Michael Jordan[a,f], Bernhard Steinberger[b], Christine M. Puskas[a], Jamie Farrell[a], Gregory P. Waite[a,c], Stephan Husen[a,d], WuLung Chang[a], and Richard O'Connell[e]

[a]Department of Geology and Geophysics, University of Utah, Salt Lake City, Utah.
[b]Center for Geodynamics, Norwegian Geological Survey, Trondheim, Norway.
[c]Department of Geological and Mining Engineering and Sciences, Michigan Technological University, Houghton, Michigan.
[d]Swiss Seismological Service, Swiss Federal Institute of Technology, Zurich, Switzerland.
[e]Department of Earth and Planetary Sciences, Harvard University, Boston, Ma.
[f] SINTEF Petroleum Research, Seismic and Reservoir Technology,Trondheim, Norway

*Corresponding author. Department of Geology and Geophysics, 135 S. 1460 E., rm. 702, University of Utah, Salt Lake City, Utah, 84112; E-mail address: r.smith@earth.utah.edu.

## Abstract

The Yellowstone hotspot resulted from interaction of a mantle plume with the overriding North America plate, highly modifying the lithosphere by magmatic-tectonic processes and producing the 17 Ma Yellowstone-Snake River Plain (YSRP) volcanic system. The accessibility of the YSRP has allowed large-scale geophysical experiments to seismically image the hotspot and to evaluate its kinematic and dynamic properties using geodetic measurements. Tomography

reveals a Yellowstone crustal magma body with 8-15% melt that is fed by an upper-mantle plume extending from 80 km to 660 km deep and tilting 60º west. Contemporary deformation of the Yellowstone caldera is dominated by SW-extension at up to ~3 mm/yr, a fourth of the total Basin-Range opening rate, but with superimposed volcanic uplift and subsidence at decadal scales averaging ~2 cm/yr and unprecedented caldera uplift from 2004-2008 at up to 7 cm/yr. Convection models reveal eastward upper-mantle flow beneath Yellowstone at relatively high rates of 5 cm/yr and opposite in direction to the overriding North American Plate. This strong flow deflects the ascending plume melt into a tilted configuration, i.e., the plume is caught in a mantle "wind". Dynamic models of the Yellowstone plume revealed relatively low excess temperatures, up to 120°K, with up to 1.5% melt, properties consistent with a weak buoyancy flux of ~0.25 Mg/s. The flux is several times smaller than for oceanic plumes, but it produced a ~600-km wide topographic ~300-m high swell. Employing the plume-geometry we extrapolated the location of the Yellowstone mantle-source southwestward to its initial position at 17 million years beneath eastern Oregon and the southern edge of the LIP Columbia Plateau basalt field suggesting a common origin. Our model suggests that the original plume head rose vertically behind the subducting Juan de Fuca plate, but at ~12 Ma it lost the protection of the subducting plate and encountered cooler, thicker continental lithosphere and became affected by the eastward upper-mantle flow. Regionally, excess gravitation potential energy of the swell drives the SW motion of the YSRP lithosphere that becomes part of a general clockwise rotation pattern of intraplate western U.S. tectonism. Our models thus demonstrate that plume-plate processes of the YSRP have "continentalized" oceanic lithosphere, enhancing intraplate extension and highly modifying topography of the continental interior. Our results demonstrate that the dynamic properties of the Yellowstone hotspot deserve recognition as a "window into the Earth's interior”.

**Keywords**: mantle plume, tomography, volcanism, earthquakes, dynamics, intraplate, kinematics, convection, hotspot, plume, Yellowstone, Snake River Plain

## 1. Introduction

In its isolation from a plate boundary, the Yellowstone hotspot is the classic example of a continental hotspot. Age-transgressive volcanism has systematically modified the composition of the overriding North America plate, creating the 700 km long Yellowstone-Snake River Plain (YSRP) volcanic province over the last 17 Ma (Fig. 1, 2). The Yellowstone hotspot is the youthful part of this dynamic system centered on the Yellowstone volcanic field and its magmatic processes of have played an important role in the intraplate Cenozoic evolution of the western U.S. However, lithospheric structure of the YSRP and its hotspot-related magmatic processes, effects on surface deformation and seismicity have been poorly understood and widely debated, largely because of a lack of definitive data.

The focus of this paper is on the youngest component of the 1.8 Ma Yellowstone volcanic field, centered at Yellowstone National Park (Fig. 3), because of the importance of characterizing its active volcano-tectonic properties that bear on the evolution of the entire YSRP. With the availability of new seismic and GPS data summarized here, we model and interpret Yellowstone upper mantle and lithospheric structure, magmatic sources, and swell deformation. We also address kinematic and dynamic interactions within this system and how it has affected the rest of western U.S.

We first review our current knowledge of the Yellowstone hotspot and its volcano-tectonic field (hereafter called Yellowstone). We then present the seismic imaging of lithospheric structure focused on the origin and properties the Yellowstone hotspot, its mantle melt properties and evidence for a plume, and the resultant kinematics and dynamics from geodetic measurements. We conclude with a discussion of the large-scale properties of whole mantle convective flow and how mantle flow has influenced the geometry and location of the Yellowstone plume as well as on the dynamics of an upper mantle plume origin for Yellowstone.

**1.1 Hotspots and Plumes**

Largely because of their presumed association with the Earth's deep interior, plumes of ascending magma have been commonly thought of as the sources of volcanic hotspots, i.e. areas of long-lived concentrated volcanism (Wilson, 1963; Dietz and Holden; 1970, Crough, 1978). While most of Earth's volcanism is associated with plate boundaries including mid-ocean ridges or subduction zones, some hotspots occur within plates (Fig. 1). Yellowstone is an example of a continental hotspot and is located on the western side of the North American plate, about 1000 km from its nearest plate boundary. Because of its accessibility, large-scale geophysical experiments were readily implemented and provide the key data used in this paper.

Hotspots have distinct physical properties. The most notable feature is that the passage of a plate over a plume results in a linear, time-transgressive volcanic chain and broad topographic swells (Ito and van Keken, 2007). Geochemically, the compositions of intruded and erupted hotspot magmas generally contain a component of mantle-derived melt, while the plume properties differ from the surrounding mantle in terms of composition, density, and temperature. Because they are hotter and less dense than typical mantle rock, plumes rise buoyantly and create a corresponding topographic swell at the surface. Combined with the low-density plume, the swell creates a mass deficit at the hotspot that can be produce a notable gravity and geoid signature. Moreover, modeling the dynamics of both the shallow and deep mantle requires information on such factors as thermal buoyancy, lithologic heterogeneity, and laterally varying rheology.

The significance of hotspots can be seen in the Earth's gravity field (Tapley et al., 2005), where strong, long-wavelength positive anomalies are associated with the Hawaii, Iceland, and Yellowstone hotspots (Fig. 1). The magnitude of the Yellowstone anomaly of ~35 MGal is thought to reflect reduced density of the lithosphere and asthenosphere across the 1000 km width of the hotspot. The Yellowstone hotspot is associated with a strong geoid anomaly of -7 m with respect to the NAD83 ellipsoid and +15 m compared to the surrounding region over an area with a 1000 km diameter, approximately the same dimensions as topographic swells of oceanic hotspots (Fig. 1). An interpretation of the geoid anomaly is that it represents an amalgam of isostatically uncompensated high topography and a broad lithospheric-asthenospheric low-density zone.

The traditional hotspot hypothesis argues that plumes result from conduits of magma, 100 to 200 km wide, that ascend through the mantle and produce long-lived volcanism at the surface. As a lithospheric plate moves across the plume, a volcanic center is displaced from the plume source and dies, while a new center forms above the plume in a cycle that propagates a characteristic chain of volcanic centers that grow older with horizontal distance from the plume. This process formed the age-transgressive 6000-km long Hawaiian-Emperor seamount chain in the Pacific Ocean over the past 80 million years. Continental volcanic features associated with hotspots include, beside Yellowstone, the European Eifel and Massif Central volcanic fields, and extinct African hotspots expressed by volcanic mountains (Burke, 1996). For the details of hotspot geology, we recommend an objective summary of hotspots, melting anomalies, and plume arguments by Ito and van Keken (2008).

The plume-plate process presumably also produced the time transgressive 16-17 Ma Yellowstone-Snake River Plain-Newberry silicic volcanic field of the western U.S., the focus of this paper (Fig. 2). The northwest time-progression of the Newberry volcanic system and the High Lava Plains of Oregon (Jordan et al., 2004; Camp and Ross, 2004) is the west or mirror-imaged branch of the YSRP and we will not include a discussion of it in this paper as it is beyond the scope of this paper and breadth of the data acquired in the Yellowstone Geodynamics project.

In traditional thinking, plumes of buoyant mantle partial melt ascend from near the core-mantle boundary in near-vertical conduits and become entrained in convective flow (Morgan, 1972). But new mantle flow models (Steinberger et al., 2004) reveal that plume tracks rise upward through convecting mantle flow and follow circuitous paths, i.e., material rises buoyantly along curved paths that follow the directions of mantle flow. Thus hotspots are not necessarily fixed and non-vertical mantle flow can tilt a plume by as much as 60º, as we show in our later discussions in Section 4-6.

However the plume hypothesis is not without conjecture. One reason is that narrow plume conduits have not been imaged by seismic tomography. Practical limitations are from the lateral extent of seismic networks and the low density of seismographs that prevent the resolution needed to resolve anomalous low wave speed bodies deeper than ~1000 km and less than ~100 km in diameter. This has been a practical restriction in imaging low-velocity plume bodies from the core-mantle boundary to the lithosphere. In the last decade, many articles have been published on the application of seismic methods to seismic studies and imaging of plumes. We will not go into details of the methodology and limitations, but refer the reader to a recent review of tomographic methodology by Nolet et al (2007).

There are multiple ideas on the origin of plumes. A widely held hypothesis argues that plumes form as upwellings associated with upper mantle convection, i.e. from the bottom of the transition zone at the 660-km discontinuity that separates the upper and lower mantle. Another theory is that plumes originate in the lower mantle from whole or partial-mantle convection. We will discuss aspects of these models in Section 6 of our paper.

### 1.2 The Yellowstone Geodynamics Project

The Yellowstone Geodynamics Project included a large-scale field experiment that was planned to give the seismic and geodetic data used for studies presented here. The project focused on a much larger scale than had done been before and included the entire Yellowstone hotspot, the eastern Snake River Plain, and surrounding 600 km by 600 km area (Fig. 4). Data from the field projects were then used to model the dynamic properties of the Yellowstone plume and the regional kinematic and dynamic properties of the western U.S. influenced by the Yellowstone hotspot.

Additional data was derived from long-term volcano and earthquake monitoring by regional seismic networks and detailed seismic and geodetic studies of Yellowstone National Park. The 25-station Yellowstone seismic network began operation in 1973 and covers Yellowstone National Park and the surrounding area to 50 km. This network is primarily supported by the USGS- and NPS-funded Yellowstone Volcano Observatory. Field GPS measurements were made biannually from 1987 to 1995, and a network of permanent GPS stations was implemented in Yellowstone and the eastern Snake River Plain starting in 1996.

The Yellowstone Geodynamics Project operated from 1999 to 2005 and included extensive seismic data acquisition, processing, analysis, modeling, and interpretation. The data acquisition phase of the project consisted of operation of a temporary 80-station broadband and short-period array (50 temporary IRIS-PASSCAL stations and a special 30-station PASSCAL telemetered array) over an area ~800 km in diameter centered on Yellowstone (Fig. 4) (see Waite et al., 2005 for a detailed description of this project). The installation of 15 permanent GPS stations was also implemented along ~160 temporarily occupied GPS sites (Fig. 4) (see Puskas et al., 2007a for a detailed description of this project). In addition we also employed seismic data from regional seismic networks and data from the University of Utah and EarthScope PBO GPS networks to supplement our analyses.

### 1.3 Other Seismic Plume Studies

Past studies have not definitively seismically imaged a mantle plume. Most focused large-scale tomographic studies have relied on permanent and temporary deployments of seismic stations, i.e. on the islands of Iceland and Hawaii and for the Eifel volcanic field, Europe (Allen et al., 2002, Wolfe et al., 2002, and Ritter et al., 2001, respectively). Images from these studies reveal low P-wave velocity bodies beneath these areas of active volcanism but could not resolve plume-like bodies that could be reliably traced to depths greater than ~400 km. The main limitation of these studies was that their seismic arrays were not wide enough to resolve seismic arrivals over the range of incidence angles required to sample deep velocity anomaly, a condition that can smear velocity anomaly over a large depth range without resolving a distinct image.

Early tomographic studies revealed a complex velocity structure in the crust and upper mantle beneath the Snake River Plain, southwest of the Yellowstone hotspot. Structural heterogeneity of the mid-crust was interpreted to represent compositional variability associated with the bimodal rhyolite-basaltic volcanism leaving a mid-crustal high density, high velocity mafic sill along the entire SRP composed of hundreds of individual sill intrusions (Sparlin et al., 1982; Annen et al., 2006; Shervais et al., 2006).

Variability in upper mantle structure including mafic crustal underplating of the SRP associated with melting (Saltzer and Humphreys, 1997). More recent work suggests that a narrow, low-velocity feature extends from the upper mantle into the top of the transition zone (Waite et al., 2006, Yuan and Dueker, 2005). The shallow upper mantle anomaly is present over a distance of more than 400 km, from the eastern extent of the Snake River Plain the northeast Yellowstone caldera. The anomaly is strongest at depths of 50 to 200 km with peak anomalies of -2.3% for $V_p$ and -5.5% for $V_s$ (Waite et al., 2006). The velocity reductions are interpreted to represent 1-2% partial melt at excess temperatures of ~170 K (Jordan, et al. 2004, 2005; Schutt and Humphreys, 2004).

Receiver function studies indicate that the mantle transition zone, which separates the upper from the lower mantle, tends to be thinner when the hot rock of a plume intersects it, raising the 660 km discontinuity to shallower depths and depressing the 410 km discontinuity (Bina and Hellfrich, 1996). Initial transition-zone studies showed significant topography of the 410 discontinuity beneath the Snake River Plain (Dueker and Sheehan, 1997). More recent studies show that the 410 discontinuity deepens by 10 km near the intersection of the low velocity anomaly identified by Waite et al. (2006). Fee and Dueker's (2004) analysis showed that the 660 km discontinuity shallows by ~20 km beneath Yellowstone, a property that we used as a constraint for the tomography and dynamic modeling of the plume properties,

Seismic anisotropy by shear wave splitting measurements of the YSRP show that fast S-wave speeds of the upper mantle are aligned primarily with the direction of apparent plate motion, except for stations in the Yellowstone caldera, which reveal rotation of splitting directions around the crustal magma chamber (Waite et al., 2005). This method separates polarity components of shear waves from distant seismic sources and assumes that olivine crystals have their fast axes aligned with mantle flow, producing a difference in the velocity of seismic waves with azimuth through birefringence. Moreover the fast-axes were not significantly perturbed as expected in circular pattern for a strong mantle plume. This observation lead to Waite et al., (2005) to concludes that a strong plume, i.e., with a high buoyancy flux, was not responsible for the Yellowstone hotspot.

To evaluate the contemporary deformation field of the Yellowstone hotspot, GPS measurements were made to determine the directions of crustal motion. These data are used to distinguish volcanically induced deformation from tectonic deformation and with additional new data from other projects to evaluate the velocity field of the western U.S. particularly on the overall kinematics.

The kinematic data are then used to model the dynamic properties of the hotspot such as composition, temperature, hydrous content, etc. and to evaluate the effect on the regional deviatoric stress field from mass variations related to plume-plate interactions.

These properties were then compared to new models of plumes rising in a convecting mantle and to models of plume deflection following the methodology of (Steinberger and

O'Connell, 1998) and (Steinberger, 2000). This methodology employs numerical models of whole mantle convection assuming that mantle flow is driven kinematically by the motion of the overlying plates and dynamically by internal density variations estimated from seismic tomography models.

We conclude by speculating on the history of the Yellowstone plume source at the transition zone source depth and its effect on the 16-17-million year history of the YSRP system. This was done by extrapolating the mantle source backward in time and space to evaluate its correlation with the surface volcanic features of the YSRP, the High Lava Plains, and the Columbia Plateau basalt field.

## 2. Volcano-Tectonic Setting of Yellowstone

The Yellowstone volcanic field (Fig. 2) is located at the northeastern end of a 700 km-long, age-progressive, bimodal basalt-rhyolite system that defines the track of the Yellowstone hotspot (Armstrong et al., 1975). A mirror image of the YSRP extends northwest across the High Lava Plains to the Newberry caldera, Oregon (Geist and Richards, 1993). The latter zone, while not as volcanically voluminous as the SRP, reflects a similar silicic volcanic history associated with sub-lithosphere source of magmatism.

An arcuate shaped area of high topography, active faulting, and earthquakes that we call the tectonic parabola surrounds the subsided and seismically quiet Snake River Plain. The SRP is seismically quiescent at the M3+ level and lacks faulting but has notable Late Quaternary basaltic dikes of similar orientation to regional faults (Fig. 2). The dikes are hypothesized to structurally extend the crust at the same rate as the surrounding area of the northern Basin-Range by non-explosive eruption of Holocene basalts covering older rhyolite flows (Rodgers et al., 1990; Parsons et al., 1998).

The Yellowstone hotspot has been the source of voluminous rhyolite tuffs and lavas, with eruptions often having volumes of hundreds to thousands of cubic kilometers and representing some of the most voluminous Quaternary volcanism on Earth over the history of the Yellowstone-Snake River Plain volcanic field. More than 140 giant silicic eruptions have been identified by the tephrachronology of ash flow tuffs associated with Yellowstone hotspot volcanism (Perkins and Nash, 2002). YSRP volcanism is similar to other Late Cenozoic silicic volcanic centers of the Basin and Range province but have rhyolites with higher magmatic emplacement temperatures and include theoleiitic rather than alkali olivine basalts, a characteristic shared with basalts of the Columbia Plateau and the High Lava Plains (Perkins and Nash, 2002).

The active component of the Yellowstone volcanic field is characterized by youthful 2 Ma caldera-forming silicic magmatism, a high topographic swell, and a geoid anomaly, the latter of which extends outward hundreds of kilometers and has the same scale as oceanic hotspots (Smith and Braile, 1994; Smith and Siegel, 2000) (Fig. 1). Moreover, Yellowstone is recognized as a globally significant volcano-tectono system (Christiansen, 2001) that originates from a vigorous sub-crustal source of heat. Three caldera-forming explosive eruptions at 2, 1.6, and 0.6 Ma formed the currently active Yellowstone volcanic field (Fig. 5). More than 50 post-caldera rhyolite flows have since covered the Yellowstone Plateau, the youngest 70 000 years ago (Christiansen, 2001). In addition, the Yellowstone caldera exhibits extraordinary high heat flow (Fig. 6), high rates of seismicity and earthquake swarms, including a M7.5 earthquake in 1959, unprecedented decade-long periods of uplift and subsidence at rates of up to 2.5 cm/yr, and the world's greatest display of geysers and hot springs at Yellowstone National Park (e.g. Pierce and Morgan, 1992; Smith and Braile, 1993, 1994; Morgan et al., 1995).

The YSRP is an area of pronounced high heat flow that stands out regionally amongst the thermal provinces of North America (Blackwell et al., 2006). The averaged regional heat flux of the Snake River Plain is ~150 $mWm^{-2}$, 50% higher than the Basin-Range to the south and three times higher than the background flux of the Rocky Mountains to the east (Fig. 6). But the extraordinarily high heat flow of ~2000 $mWm^{-2}$ of the Yellowstone volcanic field is more than 30-40 times the heat flow of continents. About 25% of the total flux is due to conductive heat transfer fed by thermal conduction from crustal magma sources (to be discussed later) that in turn are fed by magmas from the Yellowstone mantle plume.

Throughout Yellowstone heat flow is highly variable because it is dominated by shallow convective fluid flow associated with movements of hydrothermal fluids and shallow magma migration (Fournier, 1989). While the averaged convective heat flux is about 2000 $mWm^{-2}$, it can attain extremely high values in thermal basins. Because of the highly lateral variability in convective flow, standard heat flow measurements can only be made in a few restricted sites (Fig. 6). The best example is from the heat flow studies of the northern Yellowstone Lake that is underlain by an active hydrothermal area (Morgan et. al, 1977; Smith and Blackwell, 2000). In this area hundreds of meters of lake sediments provide a thermal blanket capturing the total conductive and convective flux in localized area of hot springs, some as high as 20 000 $mWm^{-2}$, more than 300 hundred times the average flux of continents.

This extraordinarily high heat flow is thus the result of active volcanism from crustal and mantle magma sources that in turn can cause large variations in density and thus stress potential and deviatoric stresses, which can lead to earthquakes, faulting, and crustal deformation (see

DeNosaquo et al., 2008, this volume, for a discussion of densities and the influence of heat flow of the YSRP).

Visitors to Yellowstone expecting rugged Rocky Mountains are often surprised by the undulating, relatively flat, forested topography of the Yellowstone Plateau, much of which is ~500 m above the surrounding area. This flat terrain is the product of youthful Yellowstone volcanism that has filled and smoothed out the pre-existing topography with rhyolite and basalt flows and by glaciation, which has scoured off its sharp topographic features and filled the lakes with sediments.

Yellowstone is famous for the world's greatest concentration of hydrothermal features, with over 10 000 geysers, hot springs, and fumaroles (Fig. 7). These features are the manifestations of the enormous heat flow resulting from hot water circulating along fracture systems in the upper crust and heated by crystallizing magma at a depth of 10-15 km (Fournier, 1989; Husen et al., 2004). The majority of Yellowstone's hydrothermal systems are located within the Yellowstone caldera; however significant hydrothermal systems are located outside the caldera including the Norris-Mammoth Corridor and Hot Springs Basin.

Although Yellowstone volcanic activity has been attributed to a conduit-like mantle plume (e.g., Morgan, 1972; Smith and Sbar, 1974; Anders and Sleep, 1992; Armstrong et al., 1975), others have suggested an upper mantle origin. Smith (1977) ascribed it to intraplate lithospheric extension that allowed hot, buoyant magma to rise from the upper mantle. Christiansen and McKee (1978) suggested that YSRP magmatism is related to a transition from extended crust to the south to less extended crust to the north. King and Anderson (1995) modeled Yellowstone volcanism as a result of asthenospheric flow perturbed by the cratonic root. And Humphreys et al. (2000) suggest an upper mantle convective system of propagating melt production associated with North America plate motion.

Earliest suggestions of a mantle source for Yellowstone magmatism were based on earthquake imaging from a sparse seismic array (Iyer et al., 1981). Most recently Yuan and Dueker (2005) and Waite et al., (2006) have used the initial data from the 1999-2005 geodynamics experiment, described in Section 1.2, to infer a mantle plume structure to depths of ~450 km.

However, relative to the Columbia River and contemporaneous Steens Basalts of Oregon, the subsequent Yellowstone-Snake River olivine theoleiitic basalts and high-alumina olivine theoleiitic basalts of the High Lava Plains have: 1) a major contribution from depleted (MORB-like) mantle (Carlson and Hart, 1988; Hart and Carlson, 1987), and 2) a sub-continental lithospheric mantle component (Leeman, 1982; Hart and Carlson, 1987). In addition, a primitive mantle component commonly associated with the lower mantle is evidenced by elevated $^3He/^4He$ values of hydrothermal waters and radiogenic isotope signatures of Yellowstone basalts of (Craig et al., 1978; Doe et al., 1982; Leeman, 1982; Kennedy et al., 1985 and Leeman et al., 2008, this volume). Thus, petrologic and geochemical data suggest a sub-crustal magmatic origin with contributions from the mantle, a depleted asthenosphere, and old continental lithosphere. These properties require unusually high temperatures.

Volcanism of the Yellowstone hotspot trend differs from typical mantle plume-related volcanism in several ways: 1) the associated Newberry hotspot has migrated northwestward across the High Lava Plains at rates comparable to that of Yellowstone but with much smaller eruptive volumes, nonetheless producing a petrologically similar mirror-image age progression of bimodal volcanism (Fig. 2) , 2) parallel upper-mantle thermal anomalies of comparable seismic velocity reduction further south in the Basin and Range Province, 3) a lack of clear age progression among the related YSRP basalts from Quaternary eruptions extending the length of the YSRP from Yellowstone to the Cascades, and 4) Yellowstone magmatism and the northern margin of Basin-Range extension are interrelated.

The relationship of the Yellowstone hotspot volcanics to the voluminous LIP (Large Igneous Province) Columbia River 17 Ma basalt volcanism is problematic. While flood basalts are commonly associated with the onset of hotspot activity, the Columbia River basalts are less voluminous than most flood basalt provinces, they lie to the north of the commonly projected trace of the Yellowstone hotspot, and they are only the most active part of a long, narrow zone of nearly simultaneously active basaltic fissures that extend south into central Nevada (Fig. 2).

In addition to the origin of the Yellowstone hotspot, we are also interested in the relations among the young and ongoing tectonic and magmatic processes that are actively reconstructing and modifying the lithosphere. Yellowstone hotspot volcanism is superimposed on the tectonics of the 30 Ma Basin and Range province, an 800-km wide province of active faulting and extension driven by the gravitational collapse of a thickened lithosphere in response to cessation of subduction at the southwest plate margin and the development of the Pacific-North America transform boundary. Basin-Range extension is in turn superimposed on relic structures of crustal compression and thickening associated with 80 to 45-Ma Laramide and Sevier orogenies.

In short, the origin of the Yellowstone hotspot has been enigmatic. Is it a plume originating in the shallow or deep mantle? How much of its character is a result of upper mantle processes in a highly modified Archean lithosphere? How does mantle flow affect the geometry and structure of the plume? These are important problems that this paper will address.

Moreover Yellowstone is a window into the processes of lithospheric construction, destruction, and magmatism. And Yellowstone is leaving a record that can be compared with hypothesized hotspot-continent interactions that have been commonly invoked for similar features around the world.

## 2.1 Yellowstone Seismicity

The Yellowstone region is one of the most seismically active areas of the Intermountain west and Rocky Mountains and occupies much of the central and northern Intermountain Seismic Belt (ISB) (Smith and Sbar, 1974, Smith and Arabasz, 1991). Seismicity in this belt, which separates the active tectonism of the interior western U.S. from the stable part of the North American plate, is the result of a combination of extensional tectonism and local spatial and temporal variations in stress related to the magmatic and hydrothermal systems.

The Yellowstone seismic network spans the entire caldera and surrounding faults of the Yellowstone Plateau (Fig. 8). More than 30 000 earthquakes for the period 1973 to 2007 were recorded (Fig. 9), most of which had magnitudes less than 4 (Waite and Smith, 2004). We specifically note that depths of earthquakes and crustal tomographic images are with respect to a datum of 2 km, the average elevation of the Yellowstone Plateau.

Notably, Yellowstone has experienced large earthquakes including the August 1959 $M_S$7.5 Hebgen Lake, MT, earthquake, which was the largest historic earthquake of the western U.S. interior (Fig. 9 and 10a). It was located 25 km northwest of the north rim of the Yellowstone caldera (Doser, 1985) and its relationship to regional stresses associated with the Yellowstone swell are problematic.

The Hebgen Lake earthquake broke along a pair of west-trending normal faults totaling 40-km long with up to 5.7 m of slip and resulted in the deaths of 28 people. In contrast, the Yellowstone caldera is characterized by frequent and smaller earthquakes, the largest the $M_L$6.1 Norris Junction earthquake (Pitt et al., 1979), which was also the largest recorded event to occur within the Yellowstone caldera. Caldera rim faults (Fig. 10b) extend for tens of kilometers around the caldera and while they are not seismically active, they may have the potential for large earthquakes related to loading from stress changes caused by magmatic processes.

Seismicity in Yellowstone is characterized by extensive earthquake swarms punctuated with large scarp-forming M 7 earthquakes, described above. Yellowstone historic seismicity is evaluated from precisely relocated hypocenters of the Yellowstone earthquake catalog, November 1972 to December 2007 (Husen and Smith, 2004). Hypocenters have been relocated using new three-dimensional P-wave velocity models and probabilistic earthquake location of Husen et al. (2004). In addition, new coda magnitudes for events between 1984 and 2007 were computed with an improved coda magnitude equation. Earthquakes were relocated using a nonlinear, probabilistic solution to the earthquake location problem.

The most intense seismicity in the Yellowstone region occurs northwest of the Yellowstone caldera between the Hebgen Lake fault and the northern rim of the caldera (Fig. 9). Cumulative seismic moment release in this region is an order of magnitude higher than inside the Yellowstone caldera (Puskas et al., 2007a). Epicenters in the northwestern part of Yellowstone form two distinct bands: one extending in an E-W direction from Hebgen Lake to Norris Geyser Basin, the other extending in a general NW-SE direction from Hebgen Lake to the northern rim of the Yellowstone caldera. The majority of earthquakes in this area occur between 5 and 10 km depth but focal depths > 12 km are observed close to Hebgen Lake (Fig.11).

The largest historic earthquake swarm in Yellowstone, which began in October 1985, also occurred in the area northwest of the Yellowstone caldera. The activity during this swarm migrated away from the caldera at about 150 m/d, at a time when the deformation of the caldera was changing from uplift to subsidence. This evidence suggested the swarm was triggered by the pore pressure diffusion away from the caldera, possibly following an episodic release of trapped fluids (Waite and Smith, 2002). Many of the earthquakes in the E-W band north of the caldera also occurred during swarms, but they did not typically exhibit a migration of activity (Waite, 1999; Farrell, 2007). Most of these earthquake swarms occur as individual clusters within the band of general seismicity (Fig. 9).

Seismicity in the Yellowstone region correlates with the Late Quaternary Hebgen, Madison, and Gallatin faults (Smith and Arabasz, 1991; Miller and Smith, 1999). Some of the faults have been mapped and dated (Fig. 5 and 9), but active seismogenic structures are thought to be buried under rhyolitic flows that postdate the latest caldera-forming eruption. These faults are theorized to have experienced a significant increase in Coulomb failure stress due to the rupture of 1959 $M_S$7.5 Hebgen Lake earthquake (Chang and Smith, 2002), explaining the intense seismicity of northwestern Yellowstone National Park. The areas of largest increase in Coulomb failure stress coincide very closely with the two seismicity bands stretching east from Hebgen Lake to Norris Geyser Basin and southeast from Hebgen Lake to the northern rim of the Yellowstone caldera. The modeled increase in failure stress decreases beyond Norris Geyser Basin and beyond the northern rim of the caldera (Chang and Smith, 2002).

Another explanation for the high seismicity in northwest Yellowstone is thought to be from stresses arising from postseismic relaxation of the lower crust and upper mantle as a response to the Hebgen Lake Fault earthquake (Chang and Smith, 2008). Relaxation can increase normal stress along faults in the Hebgen Lake area, hence encouraging the occurrence of local earthquakes, as evidenced by current GPS N-S extensions across the fault zone of 2-3 mm/yr (Puskas et al., 2007a) and consistent with the local stress field estimated from local focal mechanisms (Waite and Smith, 2004).

The Yellowstone caldera itself is characterized by shallow and diffuse hypocenters with some individual clusters of earthquakes. The central part of the caldera has relatively low seismicity, and no distinct seismic patterns are associated with the Mallard Lake resurgent dome in the western part of the caldera. The majority of earthquakes in the caldera are less than 4 km deep, with notable northwest and southeast trending zones of earthquakes parallel to the post caldera volcanic vents (Fig. 5) (Husen and Smith, 2004). Some of the earthquake clusters inside the Yellowstone caldera are associated with major hydrothermal areas such as Upper and Lower Geyser Basins, West Thumb Geyser Basin, the central part of the Yellowstone Lake, and the Mud Volcano area (Fig. 9). The pronounced shallowing of focal depths beneath the Yellowstone caldera has been explained by a decrease in depth of the brittle-ductile transition zone, as discussed in Section 2.2.

Intense seismicity is also associated with the Norris Geyser Basin close to the northern rim of the Yellowstone caldera. Seismicity associated with hydrothermal areas commonly occurs as swarm-like behavior clustering in time and space (Upper Geyser Basin, central part of Yellowstone Lake), and sometimes seismicity is persistent in time (West Thumb Geyser Basin, Lower Geyser Basin) (Farrell, 2007).

Cumulative seismic moment release is significant for some of the hydrothermal areas, e.g. West Thumb Geyser Basin, Mud Volcano area, and central part of the Yellowstone Lake, as compared to the background seismicity. Focal depths of earthquakes close to hydrothermal areas are generally shallow, < 4 km depth, and are in part associated with pressurization of hydrothermal fluids within the upper shallow crust.

In addition to the background seismicity, Yellowstone has experienced triggered earthquakes due to the passage of large-amplitude surface waves from distant earthquakes that cause rapid changes in the stress. Earthquake triggering in Yellowstone from distant earthquakes is known to have occurred due to the 1992 M7.4 Landers earthquake (Hill et al. 1993) and the 2002 M7.9 Denali fault earthquake (DFE) (Husen et. al., 2004a, Husen et. al., 2004b). For example, 250 earthquakes were triggered within the first 24 hours following the passage of the DFE surface waves. Within this first 24-hour period 11 earthquakes with Mc > 2.5 were recorded compared to nine earthquakes with Mc > 2.5 in all of 2002 prior to the DFE (Husen et. al., 2004b). The triggered seismicity slowly decayed over the next few weeks with the magnitudes of triggered events ranging from <0.0 to 3.2.

The DFE also produced pronounced significant changes in geyser activity in Yellowstone. Of the 22 geysers that were being monitored during the winter of 2002-2003, 8 displayed notable changes in their eruption intervals due to the passage of the DFE surface waves (Husen et. al. 2004a).

### 2.2 Effects of High Temperatures On Earthquake Focal Depths

Lateral variations in focal depths of earthquakes of the Yellowstone caldera are thought to reflect variations in the depth to the brittle-ductile transition. In Fig. 11, we show the 80th percentile depth of earthquakes as the brittle-ductile isosurface of constant temperature. Taking the brittle-ductile transition temperature of 450°C, as hypothesized by Smith and Bruhn (1984) for extensional tectonic regimes, allows estimates of the conductive temperature gradient.

This distinctive shallowing of the seismogenic layer beneath the caldera is attributed to high temperatures that reduce the strength of the rock, transforming it from brittle to ductile behavior above a shallow high-temperature source, namely magma. With the caldera, the crust appears to behave in a quasi-plastic state at depths exceeding 4 km at temperatures greater than 350°C to 450°C as determined from petrological constraints. Such hot rocks are incapable of sustaining shear stresses on faults (Smith and Bruhn, 1984). The maximum focal depths of ~15 km occur about 10 km from the west side of the caldera and correspond to a thermal gradient of ~26°C/km. Inside the caldera, the average 80$^{th}$ percentile depth is 4 to 6 km and corresponds to a gradient of 110°C/km to 65°C/km. These values are considered the conductive component of heat flow and would correspond to heat flow values of ~250 $mWm^{-2}$ which is about 6 times smaller than the total conductive and convective heat flow of ~2000 $mWm^{-2}$ and thus requires a convective heat transfer of ~1750 $mWm^{-2}$.

The relative magnitude of thermal convective heat transport is specified by the Nusselt number, defined as the ratio of the convective to conductive heat flow. For Yellowstone, the Nusselt number of 8 compares with the Nusselt number calculated for the Long Valley caldera, CA, of 6 to 8 (Hill, 1992).

### 2.3 Earthquake Hazards

While this paper is not a discussion of earthquake hazard of the region, the historic seismicity plus Late Quaternary fault data form the basis of a companion paper in this volume on the probabilistic seismic hazard analysis by White et al. (2008). Their results reveal that the dominant earthquake hazard of the Yellowstone-Teton region are associated with the large normal faults of the area, the Teton, Red Mountain, Hebgen Lake, Madison, Gallatin and South Arm faults. None of the magmatic-related faults are considered seismogenic although they can produce seismic activity during periods of volcanic activity.

We note a reduction in earthquake hazard within the Yellowstone caldera that is due to the very narrow depth of the seismogenic zone caused the high temperature gradients, that restricts the fault to ~4 km deep and short, i.e., not more than the length of the resurgent dome graben faults of a few km. Comparing these data with the fault-magnitude parameterization of Wells and Coppersmith (1994),the maximum magnitude earthquake for the caldera would not be expected to exceed M6.5 to 6.8. Volcanically induced earthquakes are of course a possibility, but seldom exceed M6.5 for other volcanic areas including the Snake River Plain (Smith et al., 1996). For earthquakes directly associated with a dike intrusion, the maximum magnitudes are estimated to be ~M5.

## 2.4 Crustal Structure

The three-dimensional (3D) P-wave velocity and P- to S-wave velocity ratio structure of Yellowstone has been determined using local-earthquake body-wave tomography from data of the Yellowstone seismic network. Husen and Smith (2004) selected 3374 highest quality, local earthquakes between 1995 and 2001 to invert for the three-dimensional (3D) P-wave velocity, $V_p$, and P- to S-wave velocity ratio ($V_p/V_s$) structure. The results confirm the existence of a low-$V_p$ body at depths from ~8 km to the maximum depth of resolution of ~16 km (Fig. 12). The body is interpreted to represent hot, crystallizing magma beneath the Yellowstone caldera, i.e., a magma chamber.

The low-velocity body, directly beneath the Yellowstone caldera, suggests that it is the source of Yellowstone's volcanism. Its apparent "U upward" shape, with the shallowest part of the velocity beneath the two resurgent domes, may be in part due to the lack of resolution between the shallowest bodies, or it may reflect shallow magma conduits that feed the resurgent domes and hence are the main source of Yellowstone caldera magmatism. For a maximum $V_p$ reduction of ~6 %, the corresponding melt fraction may be as large as 5-10%. Together with the geochemistry, this magma body is thus likely composed of a partial melt of basaltic and granitic composition that has fed Yellowstone's Late Quaternary volcanism and in turn was fed from basaltic magma from a deeper mantle plume.

We note that these data are consistent with model for a silicic magma reservoir that is responsible for Yellowstone's youthful volcanism and overlies a middle and lower crust intruded by plume-derived basalt (Lowenstern and Hurwitz, 2008). Their model, derived from geochemical arguments of $CO_2$ flux and thermal models, suggest that silicic magma is a hybrid of crustal melts and residual liquid formed as mafic magma cools and crystallizes, and that magma rises closest to the surface (5–7 km depth) beneath the resurgent domes.

Another result of this analysis was the imaging of a shallow volume of anomalously low $V_p$ and $V_p/V_s$ in the northwestern part of Yellowstone volcanic field at depths of <2.0 km. Models indicate that this anomaly can be interpreted as porous, gas-filled rock. The close spatial correlation of the observed anomalies and the occurrence of the largest earthquake swarm in historic time in Yellowstone, 1985, suggest that the gas may have originated as magmatic fluids released by crystallization of magma beneath the Yellowstone caldera.

### 2.5 Yellowstone-Snake River Plain Stress Field

The combination of regional extension and magmatic processes at Yellowstone produces a complex deformation pattern (Fig. 13) resulting from tectonic and volcanic processes. Yellowstone has undergone caldera-wide and localized episodes of historic uplift and subsidence (e.g. Wicks et al. 1998; Chang et al., 2007; Puskas et al., 2007a) as well as late Quaternary deformation as evidenced by the youthful volcanism and Holocene paleoearthquakes (Christiansen, 2001; Haller et al., 2004). Fig. 14 shows a summary of horizontal extensional strain and minimum principal stress directions determined from geological and geophysical studies of the region (Zoback and Zoback, 1991; Nabelek and Xia, 1995; Smith et al., 1996; Waite and Smith, 2004; Puskas et al., 2007a). For simplicity, we will approximate the minimum principal stress directions and focal mechanism T-axes as extension directions.

Crustal extension dominates the regional deformation pattern. Extension directions are generally NNE-SSW immediately south of Yellowstone (see White et al, 2008, this volume) and E-W from the Teton Range south into southeastern Idaho, but changes north and west of Yellowstone to NE-SW except in the vicinity of the 1959 Hebgen Lake earthquake where it is closer to N-S or NNE-SSW.

The regional change in extension direction is clearly seen within the Yellowstone Plateau. Focal mechanism T-axes and minimum principal stress directions from focal mechanism inversion are roughly N-S west of Yellowstone but rotate to NNE-SSW north of the Yellowstone caldera and then abruptly rotate to NE-SW at Norris.

The earthquake stress indicators are sparse within or south of the caldera so we include data from local earthquake shear-wave splitting (Waite and Chang, 2007). Fluid-filled cracks are preferentially aligned with crustal stresses, resulting in an anisotropic seismic medium (e.g., Crampin and Chastin, 2003). Shear-wave fast anisotropy directions ($\phi$) were estimated by determining shear-wave splitting from local earthquakes and the maximum and minimum horizontal stress directions from the anisotropy were inferred. Averaged directions of fast anisotropy were measured at each station. These arrows are approximately perpendicular to the directions of maximum horizontal extension interpolated from GPS-measured deformation (Puskas et al., 2007a), focal mechanism T-axes, and minimum principal stress directions.

The influence of post-seismic deformation following the 1959 Hebgen Lake earthquake was suggested as a factor in the abrupt change in the stress direction at Norris (Waite and Smith, 2004). We also note that NW-SE alignments of post-caldera volcanic vents within the caldera likely represent zones of weakness related to structures that predate the 640 000-year-old Yellowstone caldera and its post-caldera rhyolite flows (Ruppel, 1972; Christiansen, 2001; Waite and Smith, 2004). The north to northwest vent alignments appear to link N-S oriented normal faults south of the caldera with N-S oriented normal faults to the north. For example, the Gallatin fault and the Red Mountain Fault zone may be linked by the NW-SE trending alignment of vents through the central caldera.

GPS and InSAR studies (Wicks et al., 1998; Wicks et al., 2006; Chang et al., 2007; Puskas et al., 2007a) have revealed temporal changes in the strain field at Yellowstone, but similar changes have not been identified in the seismically derived measures of stress or strain except in the case of the 1985 swarm. The direction of maximum principal stress rotated from vertical during that swarm to become horizontal and sub-parallel to the direction of earthquake activity migration.

In summary, the stress field of the YSRP is dominated by NE-SW extension that is hypothesized to have begun with inception of Basin-Range tectonism in this area at ~17 Ma. Extension implies minimum horizontal compressional stress that would amplify vertical buoyancy of mantle melt that can enhance YSRP volcanism because of the reduced horizontal compressive stress.

## 3. Crustal Deformation of the Yellowstone Plateau

### 3.1 Geodetic Measurents and Data Processing

Earliest geodetic measurements in Yellowstone were from precise leveling of benchmarks in 1923 in conjunction with road construction. The benchmarks were re-surveyed in 1975-76-77 when the highways were upgraded (Pelton and Smith, 1982). Re-observations of these points discovered the unprecedented uplift of the entire Yellowstone caldera by up to 75 mm.

These observations lead to the establishment of 15 permanent GPS stations that were installed in Yellowstone and the central Snake River Plain and surrounding areas for the Geodynamics project beginning in 1996. In addition ~160 campaign GPS stations were observed at various times in eight surveys (1985, 1987, 1989, 1991, 1993, 1997, 2000, and 2003) over the study area (Fig. 13), (see Puskas et al., 2007a for details of these field projects).

The purpose of the geodetic observations was to measure deformation rates of the Yellowstone volcanic field needed to model fault slip, magmatic fluid migration, and regional extension. The GPS measurements focused primarily on the deformation of the Hebgen Lake, MT, and Teton, WY, faults, the Yellowstone caldera, the eastern Snake River Plain, and the Yellowstone tectonic parabola.

Up to six GPS stations were occupied continuously and served as local reference points. Stations from the International GPS Service (IGS) (Mueller, 1991) were included as additional base reference stations in 1995, 2000, and 2003. Coordinates of the IGS and CGPS stations were available in the global ITRF96 reference frame (Sillard et al., 1998) and allowed the Yellowstone stations to be tied to the global reference frame. These GPS observations generally achieved a precision of <3 mm in the horizontal component and < 10 mm in the vertical component (Puskas et al., 2007a).

### 3.2 Kinematics of Yellowstone from GPS Observations

GPS velocities were determined by calculating changes in station coordinates over time to obtain the station velocities. Velocities were assumed to be linear and calculated for all stations observed for two or more campaigns. The campaigns were sorted into three periods to document temporal changes in Yellowstone: 1987-1995, 1995-2000, and 2000-2003. These observations had horizontal velocity errors of typically 1-2 mm/yr, while vertical errors were ~10 mm/yr for most stations.

At least three stations of the 1987-1995 campaigns were selected as fixed stations, and their coordinates and velocities were tightly constrained to positions and velocities from the 1995-2000 positions and velocities. This was done because the earlier campaigns predated the establishment of the IGS network in 1993. IGS stations were used as reference points and their positions and velocities were constrained in the North America fixed reference frame (Bennett et al. 2001) for the 1995-2000 and 2000-2003 time windows. In this reference frame, it is assumed that there is no deformation in the stable continental interior, and all velocities are with respect to the continental interior, also called stable North America.

The velocities for the three time periods revealed notable deformation changes in horizontal and vertical velocities (Fig. 13). These data show an unexpected pattern of alternating subsidence and uplift of the Yellowstone caldera at up to 2 cm/yr, uplift northwest of the caldera, and regional extension at 2-4 mm/yr across the Hebgen Lake fault zone. During the observing periods, stations southwest of the caldera and outside the aforementioned regions moved southwest, indicating regional extension with respect to stable North America (Fig. 13).

The caldera floor sank from 1987-1995, rose slightly from 1995-2000, and resumed subsidence in 2000-2003 – *evidence of a living breathing caldera*. Subsidence occurred on the long axis of the caldera, reversing a trend of uplift that had been measured by leveling between 1923-1985 (Pelton and Smith, 1982; Dzurisin and Yamashita, 1987; Holdahl and Dzurisin, 1991). Notably, 112 mm maximum subsidence occurred on and around the northern caldera resurgent dome. In 1995, this subsidence stopped, and uplift shifted to the northwest caldera boundary area and continued through 2003, for a total of 117 mm. When subsidence resumed in 2000, the caldera sank an additional 27 mm in a three-year period. This subsidence was concurrent with ongoing uplift to the northwest.

The episodic caldera motions were corroborated by the permanent, but less dense, GPS stations. Five of the permanent sites operated from 2000 and 2003 and showed a net subsidence, while the single station northwest of the caldera had a net uplift.

Vertical displacement fields (Fig. 13) from the individual station velocities clearly correlate with the variations in horizontal spatial deformation. During periods of subsidence, caldera vectors pointed inward toward the long axis, while during periods of uplift vectors diverged radially from the center of uplift. Both these trends were discernible in 2003, when uplift continued at the northwest caldera and subsidence resumed within the caldera.

Notable extension occurred across the Hebgen Lake fault during the study period at rates from 3 to 5 mm/yr, with the highest rate in 1995-2000. This implies that the deformation here may have been influenced by uplift in the northwest caldera. Significant uplift was also observed at most of the stations near the fault (Fig. 13). At least part of this uplift episode that has been explained by post-seismic viscoelastic relaxation of the lower crust and upper mantle following the 1959 M7.5 Hebgen Lake earthquake that produced deformation of up to 2 mm/yr north of the fault (Chang and Smith, 2005).

The Snake River Plain area adjacent to Yellowstone moved southwest at 2.4 ± 0.4 mm/yr from 1995 to 2000. This motion was less than southwest extension rate across the caldera for the same time period, implying compression between the Yellowstone Plateau and the Snake River Plain. However, southwest extension rates across the caldera varied for the different time windows, and the compression may have been a transient phenomenon.

### 3.3 Magmatic Source Modeling of Deformation Data

Volumetric strain modeling was employed to determine the configuration and depths of source bodies responsible for uplift and subsidence of the caldera. The crust of the caldera was divided into a 3D grid with three depth layers. The modeling algorithm related the observed surface motions to volumetric changes of grid blocks by a Green's displacement functions (Vasco et al., 1988). Surface motions, measured by leveling surveys between 1987 and 1993 and InSAR (Interferometric Synthetic Aperture Radar) between 1992 and 2002, were combined with the GPS data for 1987-2003. Total surface motions were obtained from the weighted sum of volume changes in individual grid blocks (Vasco et al., 1990). A linear least squares inversion was used to minimize the sum of squares of the residuals.

For 1992-1995, the modeled volumetric decrease was located on the caldera axis, between the resurgent domes and extended from 6-10 km depth (Vasco et al., 2007). The deflation rate during this interval was $8.7 \times 10^{-3}$ $km^3$/yr for a total volume loss $2.6 \times 10^{-2}$ $km^3$. For 1996-2000, caldera uplift was modeled by volume increase below the northwest caldera boundary at 6-10 km depth. The inflation rate was $4.6 \times 10^{-3}$ $km^3$/yr and the total volume loss was $1.86 \times 10^{-2}$ $km^3$. Additional models were for 2000-2001 and 2001-2002 using InSAR data only. These models imaged volume decrease along the caldera axis at depths of 6-8 km with uplift along the north caldera boundary at 4-6 km deep for 2000-2001 and 2-4 km deep for 2001-2002.

Interestingly, the deeper parts of the volumetric source models overlap with the top of the seismically imaged magma chamber (Husen et al., 2004). This argues that the subsidence source can originate within the upper portions of the magma chamber. The modeling assumes that the volumetric surfaces are continuous with depth which implies that, at least for caldera subsidence, source bodies extend from the near-surface through the brittle-ductile transition at ~6 km to the top of the magma chamber.

Moreover, the shallow inflating volume models of the northwest caldera may be related to a low-velocity zone, < 2 km depth, in the same region (Husen et al., 2004). The low velocities were interpreted as due to porous, gas-filled rock, where the gases were released from the magma chamber.

For fluids to produce crustal uplift, they must be trapped by an impermeable barrier that allows pore pressure to increase. The brittle-ductile transition has been proposed as a barrier to fluid flow (e.g., Fournier and Pitt, 1985; Waite and Smith, 2002, see also Section 3.4). At the near-surface, stratigraphic barriers could impede fluid flow as well.

### 3.4 Temporal Correlation of Earthquakes and Deformation

The correlation of earthquakes and deformation of Yellowstone from 1973 to 2006 is shown in Fig. 15. These data reveal long-term episodes of uplift and subsidence at rates of up to 2.2 cm per year. The discovery of historic Yellowstone uplift from leveling re-observations in 1975-77-76 by Pelton and Smith (1982) was considered an important signal of magmatic activity. However, the rapid change to subsidence at the time of Yellowstone's largest earthquake swarm in fall 1985 (Waite and Smith, 2004) was totally unexpected and prompted us to begin thinking of the causative relationships between earthquakes and magmatism.

For example, the seismicity of Yellowstone is characterized by intense swarms of generally small magnitude ($M_C$<3) earthquakes (Waite and Smith, 2004). The largest swarm occurred in late autumn 1985 adjacent to the northwest rim of the caldera and 10 km southeast of the eastern extent of the 1959 M7.5 Hebgen Lake earthquake rupture. More than 3000 earthquakes were recorded in the swarm during a three-month period. The swarm was concomitant with a major reversal in caldera deformation, two crater-forming explosions, and several observed changes in the behavior of hot springs and geysers (Fig. 15).

Many of the earthquakes of the 1985 swarm were of normal, dip-slip faulting style, which is the expected type of faulting in the eastern Basin-Range extensional regime including Yellowstone. 75% of the focal mechanisms determined for the first month of the swarm were oblique-normal strike-slip, which is unusual for this region of crustal extension. Principal stress axis directions computed from the focal mechanisms, as well as the rate of migration of earthquake activity, were interpreted by Waite and Smith (2004) as consistent with seismicity induced by magmatic dike propagation. It was thus plausible that magmatic or hydrothermal fluid was ejected from beneath the southern resurgent dome to the northwest and induced earthquakes once it reached the brittle crust. The volume loss as fluids escaped could be partially responsible for the change in caldera surface deformation from uplift to subsidence.

Following the 1985 caldera reversal, subsidence continued for a decade until 1995, when the caldera motion began a period of 5 years of minor uplift followed by renewed subsidence until a sudden change to accelerated uplift of the caldera at unprecedentedly high rates. At the inception of the 1995 uplift, seismicity began to increase until the onset of accelerated uplift in late 2004 (Fig. 15).

### 3.5 Accelerated Uplift of the Yellowstone Caldera, 2006-2008

GPS and InSAR measurements revealed that the Yellowstone caldera began an episode of ground uplift in mid-2004 at unexpectedly high rates of up to 7 cm/yr, three times greater than previously observed deformation episodes (Chang et al. 2007). Source modeling of the deformation suggests a near-horizontal expanding magma body over an area 40 x 60 $km^2$, at 9 km beneath the caldera, notably located near the top of the seismically imaged crustal magma chamber.

Importantly, the estimated rate of volumetric expansion of ~0.1 $km^3$/yr for this uplift episode is similar to the magma intrusion rate required to supply the extraordinarily high heat flow of ~2000 $mW/m^2$ of Yellowstone (Fournier, 1989). This evidence suggests that these are the first observations of caldera-wide magma recharge of the Yellowstone volcanic system. In addition tens to hundreds of small earthquakes ($M < 3$) occurred during the deformation period and were concentrated within the modeled dilatation zone while the rest of the caldera experienced low seismicity.

## 4. Tomographic Imaging of the Upper Mantle

In this part of our discussion we evaluate the teleseismic delay-time data that is used to provide new images of the upper mantle structure of the Yellowstone hotspot. New data are modeled and interpreted from a special Yellowstone hotspot seismic array deployment from 1999-2002 of 80 broadband/short period stations that were operated in two PASSCAL-supported deployments (50 temporary stations and the 30-station telemetered array with additional data from 45 stations of the Yellowstone, Montana, and Utah regional seismic networks, with a total of nearly 200 seismic stations). The arrays were deployed in a 500 km by 600 km area centered on Yellowstone for ~11 months each (Fig. 12).

Earlier interpretations from theses data by Yuan and Dueker (2005) and Waite et al. (2005, 2006) revealed a 60° west-dipping low P-wave velocity body to depths of ~450km that was interpreted as a mantle plume. We also note the analysis of anomalous low shear wave velocities of the YSRP system evaluated from surface wave analysis of these to depths of 200 km (Shutt et al., 2008).

In this paper we employ the use of an optimized tomographic inversion (Jordan, 2003; Barth et al., 2007; Wullner et al., 2006) to develop an updated image of the upper mantle seismic structure related to the Yellowstone hotspot. The methodology uses seismic inversion of teleseismic P-wave and S-wave delays constrained by other data such as the seismic structure of the mantle discontinuity structure (Fee and Dueker, 2004), the crustal structure of the Intermountain region (Lynch et al, 1997), the detailed crustal structure of Yellowstone (Husen et al., 2004), and the 2003 GEOID data (Fig. 12).

The delay time data were taken from the earlier study of Waite et al. (2006) consisting of recordings of 103 teleseismic events from the special Yellowstone hotspot network of 85 seismic stations. Based on the estimated accuracy of the timing, the data were sorted into three quality classes (± 0.01 s, ± 0.03 s and ± 0.05 s) for weighting in the inversion scheme. Moreover, the data consistency was extensively tested and problematic data were removed from the data set, resulting in a total of 4,319 travel time residuals from P and PKiKP phases. P-wave travel time residuals were calculated by subtracting the theoretical travel time for the IASP91 model (Kennett and Engdahl, 1991) from the observed travel time. S and SKS data were used in our earlier models but we did not employ the S-wave data in our inversions, but used the $V_s$ results of Waite et al. (2006).

To remove the effect of source mis-location and source structure, we removed the mean residual travel time from all stations for each event. This results in relative travel time residual data, mainly generated by seismic velocity perturbations beneath the station network, which show late arrivals of PKiKP phases associated with underlying low seismic velocities in three main regions, namely the Yellowstone National Park, the Snake River Plain, and the area to the NW of Yellowstone.

For the modeling, we employed the JI-3D inversion method (Jordan, 2003), designed to provide stable and highly resolved models, both in the mathematical and spatial sense. The inversion algorithm is based on a Bayes approach (Tarantola and Valette, 1982; Zeyen and Achauer, 1997), which allows including a priori information, e.g., crustal structure and 1$^{st}$-order discontinuities, in the inversion via an a priori covariance matrix. This is especially important since these features can have a significant effect on the observed delay-time data, but usually cannot be resolved by teleseismic tomography.

The forward calculations of ray paths, travel times, and Frechet derivatives are based on standard ray theory. The full 3D ray tracing is performed iteratively, using a simplex algorithm, and has been adapted from Steck and Prothero (1991). The chosen step length is 100 m and the cut-off for the simplex search $2*10^{-7}$ s. We use 15 harmonics with initial amplitudes of 1 km. These settings are clearly optimized to yield maximum accuracy at the expense of computation time. Though there is an ongoing debate about the validity of standard ray theory in tomographic problems, our reconstruction test modeling as well as other studies that employed the JI-3D method (e.g., Keyser et al., 2002; Jordan, 2003; Barth et al., 2007) show that the use of standard ray tracing provides adequate and realistic results. This is also backed by van der Hilst and de Hoop (2005). To reduce non-uniqueness and to improve stability of the inversion problem we implemented a variable optimized parameterization scheme that is explained in detail below.

### 4.1 Tomographic Model Parameterization

We employed a 1-D IASP91 (Kennett and Engdahl, 1991) homogenous starting model. The model extends to 790 km depth and consists of 22 layers. Layers corresponding to the crustal structure at 14 km depth, the Moho, and the 410 km and 660 km discontinuities, respectively, were included as a priori information with their parameters were fixed during the inversion process by attributing small values in the a priori covariance matrix of the velocity model parameters. The JI-3D program relies on an optimized parameterization (Jordan, 2003) that is variable and performed strictly according to the information distribution in the model space, i.e., the angular distribution of rays.

Blocks and nodes define the 3D velocity model. While a particular block defines the region that contributes to the calculation of the each model parameter, the actual model parameter is defined at the node, located in the center of the block. Because the velocity is interpolated linearly between the nodes, this also avoids artificial velocity jumps at block boundaries. The parameterization itself is an iterative process that uses the diagonal elements of the resolution matrix as a measure to decide if the model parameters are equally well resolved and the inversion is stable. The resulting model is defined by small blocks and dense nodal spacing where the ray distribution has the highest density. The block sizes in our model range from 10 km in the best-sampled areas of the model space to several hundred kilometers at the lateral edges of the model.

Our tomographic inversion incorporated a priori information from known crustal structure and the topography of the Moho and the geometry of the 410 km and 660 km discontinuities. The crustal a priori information comprises P-wave models from high-resolution local earthquake tomography in the Yellowstone National Park area (Husen et al., 2004) and the intermountain region (Lynch et al., 1997). For the remaining model area, the a priori information was provided by the CRUST2.0 model (the model is online at http://mahi.ucsd.edu/Gabi/rem.html) (Basin et al. 2000). After careful assessment of the resolution properties of those models, a common reliable depth range was determined as -3 km to 14 km.

Important contributions to the a priori crustal model are two highly resolved low-velocity bodies (Husen et al., 2004) in the mid to upper crust beneath Yellowstone. An ~8% $V_p$ low-velocity body has been interpreted as a hot body with up to a few percent partial melt and a second shallower body with up to 10% $V_p$ reduction is believed to be a gas body. The Moho topography and velocities also are taken from CRUST2.0, while the topography data at 410 and 660 km were obtained from a model by Fee and Dueker (2004). These data are transformed into velocity contrasts of layers at the respective depths and also treated as a priori information.

**4.2 Tomographic Inversion and Resolution**

To derive the model parameters, we invert the travel-time P-wave delay data, starting with a homogeneous initial model for the non-constrained parameters. Due to the nonlinear nature of the problem, we perform four iterations. The result depends on the a priori variances of the model parameters, or the damping parameters. These are determined by a trial and error approach. Several iterative inversions are calculated for different variances. We define the optimum solution as a simple model that provides a large reduction of the data misfit. Due to the stability of the method a moderate change of the optimum damping merely changes the amplitudes but not the features of the model. Since the resolution depends on the ray distribution, which can change during the iterative inversion, we recheck the resolution matrix to ensure that the model still provides optimum stability conditions, which implies that the diagonal elements of the resolution matrix still are "constant".

The corresponding variance reduction was 30.5%. Although the achieved variance reduction is relatively low, the resolution power of the inversion is not compromised. This low value is due to using large blocks, covering heterogeneous structure, so that the data sampling these blocks often sample different velocity contrasts and thus contradict each other. To reduce the effect of arbitrarily positioned blocks and nodes (with respect to the true structure) we apply an offset and average procedure (Evans and Achauer, 1993) during the last iteration step.

Checkerboard tests are often applied to examine one or more layers at the same time. However, due to the irregular parameterization in our approach, the ability to recover the synthetic input structure depends on the block size and relative position of the cells of the checkerboard with respect to the blocks of the inversion model. Therefore we do not consider checkerboard tests as suitable in this case.

The resolution of an inversion solution can also be assessed using either the full resolution matrix or its diagonal elements to evaluate the spatial distribution of well and less well-resolved model parameters. The inversion method applied here relies on the optimized parameterization, to keep the diagonal elements of the resolution matrix constant. As a consequence, the resolution matrix cannot be used to assess the resolution properties of the inversion since it is designed to possess near identical values, yielding no further insight. Hence we employ reconstruction tests to evaluate the resolution of our inversion results (See figures in the supplementary data).

Reconstruction tests consist of the forward calculation of a data set according to a synthetic structure in the model space utilizing the same source and receiver distribution as in the real inversion. Gaussian errors are added to the resulting data with realistic standard deviations and the data are inverted in the same way as the real data. The inversion result shows how an anomaly at the position of the synthetic input structure can be recovered in terms of location and amplitude and also shows possible smearing along main ray directions.

**4.3 Seismic Images of the Yellowstone Hotspot Mantle**

Our tomographic images (Fig. 17 and 18) reveal prominent upper-mantle low-velocity anomaly bodies beneath Yellowstone and surrounding regions with several distinct features. The

$V_P$ (this study) and $V_S$ (Waite et al., 2006) tomography reveal a strong low-velocity anomaly from ~30 to 250 km beneath the Yellowstone caldera and from 30 to 100 km beneath the eastern Snake River Plain. Peak anomalies are –2.3% for $V_P$ and –5.5% for $V_S$ (Waite et al., 2006). A weaker, smaller-volume anomaly with a peak velocity perturbation of ~–0.75% $V_P$ (and –2.5% $V_S$) (Waite et al., 2006) is imaged from about 250 km depth beneath the caldera to 650 km depth at a position ~100 km WNW of the caldera and dipping 60° (Fig. 19).

A variety of synthetic tests confirm these anomalies (see figures in the supplementary material) and indicate that the resolved amplitudes are too low. According to the findings of the reconstruction tests, we determine the real $V_p$ amplitudes of the low velocity anomalies as -3% between 30 and 200 km depth and -1% between 200 and 650 km depth. These values are included in the schematic representation of the geodynamic plume model in Fig. 20. The combined low-velocity anomaly is interpreted as a plume that extends from the transition zone and that promotes small-scale convection in the uppermost 200 km of the mantle.

In addition to the low-velocity plume structure described above, there are two additional blob-like low velocity bodies in the transition zone in the layers labeled 428 km 528 km and 572 km in Fig. 17. These depths correspond to the respective nodal layers. These structures are also somewhat recognizable in the last two model layers, below the transition zone. We again utilize synthetic tests to determine where these blobs are located and if the image is affected by smearing.

Within the mantle transition zone, small-scale anomalies as small as 50 x100 km and -0.5% velocity contrasts can be reliably resolved, where permitted by the parameterization, with only little upward and some downward smearing. In case of the plume, the latter shows an offset of 100 km in a westward direction and is outside of the region underlying the station network that defined as best resolved. Our tests show that the true velocity reduction within the transition zone again is on the order of -1%. The resolution in the region beneath the transition zone is still sufficient to recover two additional low velocity structures in the southwestern part and southeastern part of the model. However, the corresponding amplitudes are only 30% of the input anomalies. Below the transition zone neither of the weak low velocity anomalies is located in the densely parameterized part of the model any more. The reconstruction tests indicate that they might be caused by downward smearing of the structure within the transition zone.

Considering the absence of local uplift of the 660 km discontinuity boundary, the position of the deepest anomaly outside the network region, and no obvious continuation of the plume-like structure into the lower mantle from global tomography (Montelli et al., 2004, van der Hilst et al., 2005), the anomaly below 660 km may be due to smearing effects from transition zone structure into the lower mantle along the main ray direction and is not considered as reliable a result from our modeling as the shallower structure. Hence, we consider the isosurface in Figs. 19 and 20 as well resolved with a corrected amplitude of -1% instead of -0.5%.

The deeper structure to ~800 km, the maximum depth of our resolution, does not have a strong velocity contrast, but a horizontally wide zone extending beyond the area of our image of increased temperature would raise the 660 km discontinuity in the whole area around Yellowstone. Thus there are no horizontal differences that our data can resolve and that there is no uplift in the local 660 km discontinuity associated with the plume where we see it.

We also note a prominent high-velocity anomaly, +1.2% $V_P$ and +1.9% $V_S$, that is located at ~50 to 200 km depth SE of Yellowstone and coincident with thicker lithosphere of the stable interior. This area is also above a region of prominent Laramide contractional folds and thrusts and part of the Precambrian core of North America. Yuan and Dueker (2005) and Waite et al. (2006) described this structure as potentially the downwelling arm of mantle convection, but the large-scale mantle-convection models described in Section 6 argue that the return flow is nearly horizontal in this region and flowing in an easterly direction. Thus this anomaly may reflect a remnant structure of the tectosphere.

Mantle structure on a broad scale is revealed by whole-mantle tomographic images. A NW-SE cross-section through P-wave model by Montelli et al. (2004) and by van der Hilst et al. (2005) passing through Yellowstone illustrates clearly the location of Yellowstone with a west-dipping low-velocity body of -1% extending to depths of <1000 km. New data emerging from the USArray data (Xue and Allen, 2007; Burdick, 2008; Sigloch et al., 2008;) reveal a 0.5% to 1.2% low velocity body to depths of up to 1000 km underlying most of the western U.S. This pillow of low velocity material may reflect the deep underpinning of the lithospheric thermal upwelling and extension of the Basin and Range province, with a small area of leakage forming the Yellowstone plume source.

The Yellowstone upper-mantle low-velocity layer is also near the boundary of marked lithospheric change where a midmantle low-velocity pillow beneath the Basin-Range to the southwest abuts the North American high-velocity craton to the east. A major high-velocity body apparently continuous with the craton occupies most of the thickness of the upper mantle beneath Yellowstone.

This leads to another possible explanation of the Yellowstone plume origin: permanent weak, but large scale, heating below the 660 km discontinuity, could lead to localized thermal instabilities in the transition zone that appear as blobs of lower velocity (see supplemental material). One or more of those blobs could have turned into the Yellowstone plume. The recent western U.S tomographic image of Burdick et al. (2008) reveals a -1% low velocity body from 660 to ~800 km beneath Yellowstone which is wider than our array could detect. This suggests that a thermal instability from this deeper body could leak melt blobs into the transition zone.

One of those buds could have turned into the Yellowstone plume. The other buds may not develop further since the heat was effectively transported away via the plume conduit. However it is not clear how leaky thermal instability hypothesis fits in with the history of the Yellowstone plume. For example, the buds may be of younger origin than the overall plume as melt derivatives that leak off the main plume stem.

### 4.4 The Source of Plume-Plate Magma Plumbing

An important Yellowstone hotspot problem is understanding the connection between the Yellowstone crustal magma body and the mantle plume source. This results from the lack of knowledge of the seismic structure of the lower crust and upper-most mantle and hence the mantle-crustal plumbing system from current technology. Crustal seismic refraction and regional earthquake studies and the local earthquake tomography do not have sufficient spatial resolution due to: 1) the lack of lower-crustal penetrating horizontal-propagating head waves and the lack of sufficient regional earthquakes, recorded from 200 km to 1000 km distances, required in these studies, 2) the lack of resolution in this depth range for local-earthquake tomography because of the lack of local earthquake sources deeper than the mid-crust, ~ 16 km maximum depth, 3) the lack of resolution for teleseismic tomography because of insufficiently wide angle crossing rays, and 4) the lack of resolution of surface waves due to their inherent longer periods and hence longer wavelength resolving kernels.

However some observations on this problem come from a study using controlled source refraction studies (Lehman et al., 1982). Lehman et al. (1982) recognized that the lower crust of Yellowstone was similar to that of the volcanically unmodified lower crust of surrounding regions. They evaluated the wide-angle reflector from the Moho boundary and found that the travel-times for equivalent ray paths, inside and outside the Yellowstone caldera, are essentially the same. This suggested that: (1) the lower crust was homogenous between the active area of Yellowstone volcanism and the surrounding Archean Rocky Mountain crust, and (2) while recognizing that magmas must have propagated through the Yellowstone lower crust, it did not alter the velocity structure and thus the lower crust did not contain large bodies of remnant melt such as the well-resolved in the middle crust (Husen et al., 2004).

A mid crustal sill at the base of the SRP upper crust was identified by seismic refraction and receiver function studies (Braile et al., 1982; Sparlin et al., 1982, Peng and Humphreys, 1998) and interpreted to be a mafic remnant of the fractionation process that differentiates the Yellowstone magma system into the bimodal basaltic-rhyolitic volcanic rocks of the YSRP. It was modeled as composed of a series of gabbroic lenses inter-fingering with the granitic upper crust (see details of the SRP mid crustal sill gravity and seismic modeling in this volume by DeNosaquo et al., 2008). This geometry and modeling of the velocity-density relationships yields a bulk composition comparable to diorite and a density of 2900 kg/m$^3$. The high-density mid crustal sill varies from 4 to 11 km in thickness, resulting in a series of SE-NW trending gravity highs observed along the axis of the SRP. The sill extends up to 20 km southeast of the volcanic field, causing the asymmetry of the gravity field southeast of the SRP. This suggests that basaltic mantle magma ascends buoyantly to mid-crustal depths, where it attains neutral buoyancy spreads out as a province-wide sill. Hildreth et al. (1991) suggested that isotopically that Yellowstone rhyolites are derived from the melting of young underplated mafic crust rather than felsic upper crust magmas ,possibly from fractionated and re-melted basalts. This petrologic model is consistent with the seismic and gravity models.

Seismic refraction studies of the YSRP (Schilly et al., 1982; Lehmann et al., 1982; Braile et al., 1982; Schutt et al., 2008) provide information on the lower crustal structure of the YSRP and reveal a relatively high-velocity layer beneath Yellowstone but lower velocity beneath the Snake River Plain. On the basis of these generalized data, crustal magma intrusion is characterized by magmas rising buoyantly from the plume source at ~70 km depth through a vertically oriented plexus of basaltic dikes in the upper 30 km of the mantle. These dikes possibly pond at the Moho to produce underplating, but then ascending through the lower crust via another plexus of dikes. As the mafic magma passes through the lower crust, it promotes remelting of the surrounding silicic, granulitic host rock, which also ascends. The magma then differentiates into a mid crustal magma body composed of basalt and rhyolitic melts. Whether the lower crust flows laterally to accommodate the mantle magmas or whether there is a balance between the eruptive volumes and intruded volumes is problematical given the lack of quantitative relationships between the parental and erupted magma volumes, especially those of rhyolitic-basaltic mixes. The seismic data of Husen et al. (2004) suggest that this body is as shallow as 6 km beneath the resurgent domes and extending to at least 16 km, the maximum depth of the resolving paths for local earthquake tomography. Between the crust and mantle plume, 40 to 70 km, the seismic velocity data are ambiguous for the reasons stated above.

**5. Geodynamic Plume Modeling**

Our tomographic images provide a background model for dynamic modeling of the Yellowstone plume. The geodynamic plume models were analyzed for seismic velocity anomalies including the effects of temperature, anisotropy and composition, and also the presence of water or melt (Fig. 20). According to Karato (1993), temperature is the main source of seismic velocity anomalies if no heterogeneities of the chemical composition are present.

While anisotropy can have a significant effect on seismic travel times, it is neglected in this study since olivine fast axis orientation is approximately unidirectional (Waite et al., 2005). In this case, all compressional P-wave travel times from any one event are equally affected and the homogeneous imprint of anisotropy is removed by calculating relative travel time residuals. Therefore we concentrate on temperature and composition in terms of the presence of water and melt.

The presence of a thermal anomaly in the 410–660 km depth range, as allowed in one of the models by Humphreys et al. (2000), would be expected to be accompanied by thinning of the transition zone through depression of the 410 km discontinuity and elevation of the 660 km discontinuity (Bina and Helffrich, 1994). The depths to these discontinuities have been studied using receiver functions for earthquakes recorded on a 500-km-long profile traversing the eastern Snake River Plain and flanking swell at a distance of 200 km southwest of Yellowstone (Dueker and Sheehan, 1997). The results provide no evidence for a coherent thermal anomaly extending throughout the transition zone under the plain, and the results are confirmed by migration reanalysis of the data by using different techniques (Beucler et al., 1999).

Beneath the profile, transition-zone thickness was found to vary by 30–35 km, but the topographies of the two discontinuities are uncorrelated. The most significant feature is a deepening of the 410 km discontinuity by 20 km from the northwest margin of the plain to the eastern boundary of the Basin-Range. It is interpreted as a result of elevated mantle temperature with excess partial melt in the shallow upper mantle (e.g., Bina and Hellfrich 1994). The change in discontinuity depth implies uncorrelated lateral temperature variations of up to 250 K across the Snake River Plain and flanking swell, with maximum temperatures at 400 km depth at a location 150 km southeast of the plain.

Possible non-thermal explanations for the observed topography of the mantle discontinuities include the combined effects of garnet pyroxene phase transformations, chemical layering, and variations in mantle hydration (Dueker and Sheehan, 1997). The fact that the 660 km discontinuity seems to be unaffected by the mantle plume could be also be explained by the discontinuity being equally effected by a widespread thermal body underlying the 660 km discontinuity in the area of our tomographic model.

To assess the dynamic properties of the imaged plume we employed the thermodynamic methodology of Cammarano et al. (2003) and Cammarano and Romanowicz (2007) with the constraints of our velocity and attenuation models. We realize that our geodynamic plume model is for a one-dimensional case, whereas we have parameterized data from a 3D structure, but this model should not affect the overall dynamic processes.

Following Cammarano et al. (2003), we derive models for attenuation and temperatures in a two-step procedure for dry regimes first. We first derive an anelasticity model in terms of depth-dependent $Q_s$-values from the melting curves and temperatures along the geotherm. These $Q_s$-values then are transformed into $Q_p$-values (Anderson and Given, 1982) based on the comparison of compressional and shear wave velocity contrasts by Waite et al. (2006). In the next step we calculate the partial derivatives, following the work of Karato (1993) on olivine polycrystals at upper mantle temperatures and pressures. These are used to estimate the changes in velocity with temperature for a given attenuation or quality factor, respectively, so that the velocity changes can be forward modeled and excess temperatures derived as in Fig. 20.

For the wet regime, we followed Karato and Jung's (1998) explanation of the effect of water on the seismic velocities by enhancing anelastic relaxation and by lowering the melting point. Transition zone minerals can dissolve 2-3% water (Karato and Jung, 1998). Hence we examine the influence on the excess temperatures and attenuation properties that can produce the observed reduction in P-wave speed. Considering the imaged low velocity zone as a plume consisting of an upwelling of hotter mantle originating in the transition zone, the plume will carry water up into the upper mantle. The effects are decreased viscosity, lowered melting point and, when the solidus is reached, partial melting. This process will remove water from the solid minerals and therefore increase properties like shear modulus and seismic velocities (Karato and Jung, 1998). Dehydration will reduce the negative effect of increased temperature on the seismic velocities.

Since S-waves are more affected than P-waves, the dehydration may even compensate for the temperature effect on S-wave velocities. Waite et al. (2006) observe such a "hole" in their low velocity zone at about 200 km depth in their S-wave but not their P-wave model. This is consistent with findings from Kawamoto and Holloway (1997). Partial melting and dehydration may be responsible for the rapid increase in size of the Yellowstone plume above 200-250 km depth. We estimate the attenuation in terms of Q-values for this case following Karato and Jung (1998) who find $Q_{wet}=2.5 \cdot Q_{dry}$, based on the enhanced creep rate and frequency dependence. This is consistent with empirical results from Jackson et al., (1992) for dunite composition.

Also we calculated the corresponding partial derivatives and estimate excess temperatures. Ignoring the effect of the partial melting process, we find excess temperatures of

145°-168°K in the uppermost mantle, 60-72 K in the lower upper mantle, and 78-85 K in the transition zone (see Fig. 20). However, 1% partial melt can lower the compressional wave speed between 1.8% (Faul et al., 1994) and 3.6% (Hammond and Humphreys, 2000) per 1% partial melt. Consequently, the amount of partial melt in the uppermost mantle has to be far less than 1%. Assuming 0.5% melt and the relation of Hammond and Humphreys (2000), this will account for 1.8% velocity reduction leaving -1.2% as a temperature effect.

These observations and models agree well with models derived by Farnetani and Samuel (2004) for so-called "spout" plumes, predicting widely spread ponding beneath the transition zone and only a narrow tail with 120-180 km diameter and 100°-150°K excess temperatures. Moreover this model also matches the global tomography model by Montelli et al. (2004) and could explain our observations of blobs in the transition zone. However, our estimated excess temperatures (dry and wet) are considerably lower than the 200 K determined by Fee and Dueker (2004) from deflections of the 410 km discontinuity.

## 6. Deflection of the Yellowstone Plume in Large-Scale Mantle Flow

Guided by the tomographic images of the tilted upper mantle body and geodynamic models of mantle properties, we can evaluate the effect of mantle flow on the orientation of the hypothesized Yellowstone plume.

Based on theoretical, experimental, and numerical results (e.g., Whitehead and Luther, 1975; Olson and Singer, 1985; Griffiths and Campbell, 1990) the following standard view of a mantle plume has evolved: initially, a plume head rises from a source region in a thermal boundary layer (often assumed above the core-mantle boundary, but in the case of Yellowstone perhaps more appropriately at the boundary between upper and lower mantle at a depth of 660 km). It remains connected with the source region through a conduit and molten material continues to flow through the conduit to the base of the lithosphere. Volcanism may occur at the surface above the plume-plate interaction, and when volcanic products are carried away with the lithosphere moving over it, a hotspot track is created.

If there is large-scale flow in the mantle this plume conduit will "blow in the wind" and become tilted (Richards and Griffiths, 1988). The tilt will depend on the large-scale mantle flow and buoyant rising speed of material within the conduit, and can thus be computed based on models for both. Comparison of the computed conduit shape with observations obtained through seismic tomography, and of the predicted hotspot track with the observed distribution of volcanism in space and time, can thus provide important insights regarding mantle flow and plume conduit rising speed. More generally, such analysis determines whether a mantle plume is an appropriate explanation for a particular intraplate volcanic center. Locations of intraplate volcanism, such as in Yellowstone, are often attributed to mantle plumes (Wilson, 1963; Morgan, 1972), but other upper mantle-lithosphere interactions have been proposed as the source of Yellowstone volcanism as described in section 2 (Smith, 1977; Christiansen and McKee, 1978; King and Anderson, 1995; Humphreys et al., 2000).

Here we contrast the predicted plume conduit shapes for various modeling assumptions with a tomography model of the Yellowstone plume in the upper mantle. We also compare the predicted hotspot track with geometry and age progression of volcanism along the Snake River Plain, the presumed track of the Yellowstone hotspot (e.g., Pierce and Morgan, 1992; Smith and Braile, 1993). The general features of our plume model have been explained by Steinberger and O'Connell (1998). Regarding specific parameters and characteristics, we will mostly follow the work of Steinberger and Antretter (2006), which has been extended to 44 hotspots (including

Yellowstone) by Boschi et al. (2007). While the full model description is given in these papers, we are here mostly interested in the plume conduit in the upper mantle, and thus give a simplified description.

If we disregard time dependence, lateral variations, and the vertical components of large-scale flow, we expect that the conduit becomes tilted if the horizontal mantle flow velocity at depth $z$, $v(z)$, differs from flow $v(z_0)$ at source depth $z_0$. More specifically, if conduit rising speed at depth $z$ is $v(z)$, the conduit takes a time $dt = dz/v_r(z)$ to rise through a layer of thickness $dz$. During this time, it will get displaced relative to the source by an amount $dx = (v(z) - v(z_0))dt = (v(z) - v(z_0))/v_r(z)dz$. Integrating from depth $z_0$ to depth $z$ thus yields a total displacement

$$x(z) = \int_{z_0}^{z} \left(v(z) - v(z_0)\right)/v_r(z)\,dz \qquad (1)$$

For a source depth at the upper-lower mantle boundary, this implies that conduit tilt in the upper mantle should be in the direction of upper mantle flow, relative to flow at source depth, and that the tangent of conduit tilt should be the same order of magnitude as the ratio of horizontal upper mantle flow, relative to flow at source depth, to buoyant rising speed. Under these simplifying assumptions, the shape of the conduit remains constant, but the conduit moves with the flow at source depth. The predicted azimuth and age progression along the hotspot track thus depends on the difference vector between plate motion and flow at source depth.

However, if we initiate the computation with a vertical conduit, the effect of the conduit being progressively tilted by mantle flow introduces a further component of hotspot motion in the direction of upper mantle flow until steady state is reached. If a deeper source depth such the core-mantle boundary is assumed, then steady-state is not reached and the conduit will experience tilting in both the lower and upper mantle, with different directions and magnitudes of tilt at depth depending on differences in mantle flow, thus contributing an additional component to hotspot motion.

There are various parameters influencing flow in the mantle, but the largest uncertainties arise from variations in the mantle density models derived from seismic tomography, subduction history, and viscosity structure. We will use different models to obtain a realistic range of flow and plume conduit shape predictions, and consider several models of plate motion for hotspot track predictions.

Computation of large-scale mantle flow is done with the method of Hager and O'Connell (1979, 1981), employing prescribed plate motions as surface boundary conditions and internal density heterogeneities, both expanded in spherical harmonics, to compute flow. Density variations are converted from global tomography models following Steinberger and Calderwood (2006) or inferred from subduction history (Steinberger, 2000) and are named Smean (Becker and Boschi, 2002), SAW24B16 (Megnin and Romanowicz, 2000) and TX2007 (Simmons et al., 2006)

An example of a flow model is shown in Fig. 21. Computed upper mantle flow in the vicinity of Yellowstone is eastward. This eastward flow is part of a large-scale convection cell, from an upwelling underneath the Pacific towards downward flow due to the subducted Farallon slab beneath central and eastern North America. The viscosity model primarily used in our models (VM1) was derived by Steinberger and Calderwood (2006) and was based on fitting the geoid and other observational constraints, and consistent with mineral physics. VM2 is a simpler model (Becker et al., 2006) also used in our mantle flow computations. Specifics and parameters of the flow model follow Steinberger and Antretter (2006). This eastward flow in the upper mantle gives a first indication that we should expect an eastward-tilted Yellowstone plume conduit (i.e., coming up from the west).

Fig. 22 shows that this eastward flow component is strongest in the upper mantle and transition zone but decreases with depth until the bottom of the transition zone at 660 km. The flow direction and depth dependence are general features common to a large number of models. However there are variations among the models, with flow direction ranging between southeastward and northeastward, and variable flow speeds.

For the preferred model of Steinberger and Antretter (2006), plume conduit diameter in the upper mantle and transition zone is about 100 km, and buoyant rising speed increases from about 2 cm/yr at a depth of 660 km to 10 cm/yr at 400 km and remains approximately constant through the upper mantle. Total rise time from a depth of 660 km is about 12 Ma. Given typical upper mantle horizontal flow speeds (relative to flow at 660 km) of a few cm/yr (see Fig.22), we expect a conduit tilted by a few hundred kilometers, and that the surface plume position is displaced relative to the position at a depth of 660 km approximately towards the east, between southeast and northeast.

The comparison of observations with actual computations more or less confirms this expectation: Fig. 23a shows results for the case of plumes coming from 660 km depth with no assumption about the initial conduit made, i.e., all conduit elements originate at depth 660 km and the plume conduit is already tilted when the plume first reaches the surface. Tilts are in directions similar to upper mantle flow, and amounts of tilt vary between less than 100 and ~250 km. Differences between predicted hotspot tracks and the corresponding fixed-hotspot track, shown in Fig. 22, approximately correspond to the amount of plume source displacement due to the horizontal flow component at a depth of 660 km. Differences between this case and the simplified model discussed in the introduction are due to time dependence and the vertical component of the flow field

Computed tilts are somewhat steeper (~150 to 400 km), but generally in the same direction in the case shown in Fig. 23b where plumes rise from the lowermost mantle with an initially vertical conduit (at 15 Ma). This larger tilt can be attributed to the cumulative effect of tilting in the lower mantle added to tilting in the upper mantle. For the plume model based on tomography model SAW24B16, both direction and amount of predicted tilt approximately agrees with the tomographic observations reported here (Figs. 17 and 18 ). Computed hotspot tracks for the case of a whole-mantle plume tend to be longer (i.e. with the predicted 15 Ma location further from Yellowstone) than in Fig. 23a. This is due to the effect of the initially vertical conduit becoming tilted in the upper and lower mantle.

For models with an initially vertical conduit but plume initiation ages older than 15 Ma, the predicted age progressions become more similar to that shown in Fig. 23a as the "blowing over" effect of upper mantle flow causes the conduit shape to converge with the initially tilted plume models. In the case of plumes rising from the lowermost mantle, the predicted conduit tilt becomes stronger with greater age, as tilting in the lower mantle contributes to the total tilt. Predicted tracks are very similar in Fig. 23a and Fig. 23b, because in both cases, the effect of the initially vertical conduit becoming "blown over" by the upper mantle "wind" is important.

We find the best agreement between predicted and observed azimuth and age progression of the hotspot track can be achieved with eastward flow in the upper mantle. The best agreement between predicted and observed conduit shape can be achieved with southeast flow, as with models TX2007 and SAW24B16. Both are within the range of our flow models. Moreover the amount of tomographically observed tilt can be better matched with our models by having the plume originate in the lower mantle. However, a larger tilt can also result from a slower buoyant rising speed and smaller conduit diameter. Increasing temperature dependence of viscosity could decrease the conduit rising speed and diameter. Such a stronger temperature dependence would for example result if a linear stress-strain relationship (diffusion creep) was assumed in the upper mantle rather than dislocation creep with a non-linear stress-strain relationship with stress exponent $n = 3.5$ (as done by Steinberger and Antretter, 2006, whose model we adopt here).

To summarize the effect of the mantle flow on plume conduit tilt, we plot in Fig. 24 the flow and conduit for a lowermost mantle plume source from an earlier model superimposed on a background of S-wave velocity structure (Steinberger, 2000). For this model the plume origin would be at longitude 120°W, beneath the Oregon Coast and displaced 1100 km west at Yellowstone. The modeled plume location at ~660 km depth is at ~115°W, beneath the Oregon High Lava Plain and the Columbia Plateau basalt field. If Yellowstone plume volcanism initiated with the Columbia Plateau flood basalts, then this coincidence of plume position at the base of the transition zone implies an initially vertical plume in the upper mantle.

## 7. Yellowstone Geoid Anomaly

Just as the earth's topographic field responds to crustal loads, the long-wavelength gravity field and topography generally reflects deeper mantle sources. To analyze this feature we examine the Earth's geoid field. Most of the local geoid features are due to topographic variation, but deep density variations form an important source of the Yellowstone anomaly.

The large-scale isostatic properties of the YSRP can be seen in the GEOID03 model for the U.S. (Fig. 25). The model was constructed from a combination of gravity data and orthometric heights determined by geodetic surveys, with the resulting equipotential surface reflecting an amalgam of topographic relief and density variation within the earth (see Milbert, 1991 for explanation).

To model the Yellowstone geoid signal we assumed the geoid height was due to the static uplift due to density variations. We recognized that dynamic processes could also contribute to the signal but that it was negligible given the weak buoyancy flux that we determined for the Yellowstone plume model. Using the observed geoid height for the Yellowstone anomaly, we calculated the B-value, or relation between seismic velocity perturbations and mantle density variations ($\otimes V_p/\otimes\rho$) (e.g., Birch, 1961, Lees and VanDecar, 1991) at different depths of the plume conduit by the forward modelling method developed by Emile Klingele (2006, personal communication) based on Tsuboi, 1954. The resulting B-values are then used to interpret the composition, temperature, pressure, and melt within the plume. For example Schmitz et al. (1997) found a correlation between B-values and degree of partial melt. The overall objective of our modelling was to evaluate the contribution of the Yellowstone plume to the geoid anomaly relative to other local and regional tectonic and topographic sources and determine its melt percentage.

We parameterized the geometry and density of the Yellowstone geoid model by converting the velocity perturbation structure of Yellowstone plume, described above, to density variations as a starting model. While the separate derivation of density structure from either velocity perturbations or geoid data is highly non-unique, the combination of both leads to a more constrained solution.

Forward modelling of the density variation was done on a two-dimensional profile, A-A' crossing the Yellowstone hotspot from NW to SE (Fig. 25a). The density model was initially divided into nine bodies extending from 14 km to 660 km in depth, but only the top four segments were found to contribute significantly to the model (Fig. 25b). Each body was given a velocity perturbation based on the results of the reconstruction tests from the tomographic inversion. Since the true background velocities of the tomographic model are not known, the absolute velocity perturbations are based on the whole earth velocity IASP91 P-wave velocity model. 80 000 forward models were run with varying B-value combinations.

Since both the reference values for the geoid data and the velocity and density models are not well resolved, the observed and the forward calculated geoid data have to be compared on a relative basis. To do so, we shift the forward modelled geoid profile so that its maximum amplitude matches the peak of the observed geoid profile (Fig. 25c). This does not affect the lateral position or the shape of the geoid.

The geoid data were obtained from the U.S. National Oceanic and Atmospheric Administration website (www.ngs.noaa.gov/GEOID) along the profile at a 5 km spacing. The data are plotted in Fig. 25a. The profile A-A' coordinates were adapted to the profile from the seismic tomography model. The origin of the Yellowstone tomography coordinate system is located at kilometer 700 along the profile. Since the geoid signal shows high frequency components that are not associated with a deep plume model and are likely are of local tectonic or topographic origin, we applied a one-dimensional filter to the geoid data using an optimum window length of 300 km to remove short wavelength crustal contributions. Since regional effects are obvious in the data but are not contained in the model, we only calculated the misfit between 250 km and 1000 km along the profile (Fig. 25c). Only the plume effect is calculated and the surrounding velocity and density variations are not taken into account.

Density variations were forward calculated from the velocity perturbations assuming initial B-values between 2 and 6 for each body. The B-value, can be an indicator of the presence of partial melt. The effect on the geoid of the resulting density structure was calculated separately for each body based on the algorithms of Tsuboi (1954). The results were then superimposed to give the full geoid signal. The B-values of bodies 5 to 9 were fixed to a median B-value of 3.0, since the corresponding variation between the minimum and maximum effect on the geoid surface expression is about 0.3 m for body 5 and even less for the deeper bodies.

To assess the modelling result, we calculated the RMS misfit between the observed and the modelled geoid data for each of the forward models (Fig. 25c). The models were sorted so that the minimum misfit occurs in model number 1 and the maximum misfit occurs in model 80 000. The resulting model of density variations for bodies 1-4 is given in Table 1, together with the corresponding B-values for selected optimal solutions. The comparison between the B-values for bodies 1 and 2 shows that their mean value is approximately constant at 3.5. This implies that the modelling cannot distinguish between the geoid signals caused by body 1 and body 2. The optimum B-values for bodies 3 and 4 are small, implying a larger density variation $\Delta\rho$ per velocity contrast $\Delta V_p$ than for bodies 1 and 2. We interpret that the B-values to thus reflect notable density decreases of 1.3% to 3.6% in the upper part of the plume relative to the commonly assumed density of 3400 kg/m$^3$ of the upper mantle. The largest density anomaly is in the upper mantle at depths of 150 km to 170 km, the same depth range as the velocity anomaly.

As the temperature reaches the melting point, the seismic velocities decrease rapidly, while the densities only decrease slowly, resulting in increased B-values (Schmitz et al., 1997). We interpret the models to indicate that partial melt is present in bodies 1 and 2, but this interpretation is less justified for bodies 3 and 4. Since the absolute velocities and densities are not known we do not determine the exact percentage of partial melt here. However, the modelling results of relatively high B-values in bodies 1 and 2 (14 km to 110 km depth) and consistently lower B-values in bodies 3 and 4 (110 km to 285 km depth) indicate significant differences between those two regions within the plume. This correlates well with our interpretation of a plume in a wet state, where partial melt is present in the uppermost part of the plume. Below that, the plume was dehydrated by the melting process, reducing the negative effect on the amplitudes of seismic velocity perturbations but only slightly changing the density variations. This results in smaller B-values suggesting possible dehydration already below 110 km depth.

## 8. Yellowstone-Snake River Plain Kinematics and Dynamics

To evaluate the large-scale effects of the Yellowstone hotspot on the western U.S., we have determined the contemporary velocity field from over 2100 GPS measurements and 245 fault-slip rates. These data were input into the dynamic modeling codes of Haines and Holt (1993) and Haines et al. (1998). The GPS velocities were compiled from 22 studies across the western U. S., while fault-slip rates greater than 0.2 mm/yr were obtained from the USGS Quaternary Fault and Fold Database and other sources (Haller et al., 2002; Chang and Smith, 2002; McCalpin and Nishenko, 1996). The data were then interpolated to a grid using a bi-cubic spline interpolation (Fig. 26a).

The resulting model reveals a generalized clockwise rotation in the direction of crustal motions (Fig. 26a). Southwest extension across the Yellowstone caldera at up to 4.3 ± 0.2 mm/yr drives southwest motion of the Snake River Plain at 2.1 ± 0.2 mm/yr (Puskas et al., 2007a). To the south, the direction of extension rotates from southwest to west in the eastern Basin-Range. The western Basin-Range marks a transition to shear deformation that is driven by relative shear between the North America and Pacific plates (Thatcher, 2003; Meade and Hager, 2005; Puskas et al., 2007b). In the western Basin-Range and Pacific Northwest, GPS ground deformation rates decrease from 14.6 ± 0.1 mm/yr in the Sierra Nevada to 2.9 ± 0.2 mm/yr in northeast Oregon, and the direction of deformation rotates from northwest to east (Puskas et al., 2008). Velocities decrease in northern Idaho and western Montana to 1 mm/yr or less, and deformation in this transition zone becomes difficult to resolve with available GPS data. The observed rotation of velocities requires shearing and/or rotation of the Idaho Batholith to accommodate the pattern of rotation.

Horizontal deviatoric stresses were calculated from the potential energy of the western U.S. lithosphere, which in turn was dependent on elevation and density structure (Flesch et al., 2000). In order to improve the detail of the model and resolve the effects of the Yellowstone hotspot, the standard global crustal density-thickness model (Bassin et al., 2000) was rescaled for the western U.S. using Moho depths from receiver functions from EarthScope (Crotwell and Owens, 2005). The Yellowstone crustal density structure, based on gravity-density modeling (Denasquo et al., 2008, this volume), was added to the model to account for volcanic reworking of the crust in the YSRP. With the addition of topographic and isostatic corrections, these steps produced a lithospheric density structure model that accurately reflected the tectonic provinces of the western U.S. (Puskas et al., 2007b).

The deviatoric stress modeling largely corroborates the observed velocity field (Fig. 26). Internal stresses arising from lateral mass variations in the lithosphere show a notable rotation of tension directions centered on the Yellowstone hotspot. Northeast-southwest tension at the

Yellowstone Plateau rotates to east-west tension in the eastern Basin-Range. The Basin-Range experiences primarily east-west uniaxial tensional stress with shear stress to the south and west. Stress orientations in the Basin-Range are strongly affected by the boundary conditions of the stress model, which incorporates the kinematic data to constrain the stress tensor orientations at the model boundaries and hence includes relative North America-Pacific plate motions (Puskas et al., 2007b). The Pacific Northwest is a region of compression and shear (Zoback and Zoback, 1991; McCaffrey et al., 2000; McCaffrey et al., 2007) associated with the subduction of the Juan de Fuca plate. Our stress model predicts compression and shear in Oregon and Washington but finds tensional stresses in northern Idaho and the Idaho Batholith. The high stresses at the Idaho Batholith do not correspond to high deformation rates. Both GPS measurements and kinematic models support low deformation rates of less than 1 mm/yr. The discrepancy can be accounted for by postulating a strong lithosphere, so that high stresses will result in very little strain (Puskas et al., 2007b).

## 9. Effects of Mantle on the Overriding Lithosphere

On a global scale, we compare our hypothesized Yellowstone plume with other hotspots by computing the buoyancy flux using properties derived from tomographic models after the method of Ritter (2004) (Fig. 27). The buoyancy flux is estimated from the width and elevation of the hotspot topographic or bathymetric anomalies, velocity of the overriding plate, and excess plume temperature (e.g., Davies, 1988; Sleep, 1990). Given the small (< 150 K) excess temperatures predicted for a dry mantle with low Q (estimated jointly from the $V_P$ and $V_S$ models), the Yellowstone buoyancy flux is at least one order of magnitude lower than previous estimates (Sleep, 1990; Smith and Braile, 1994; Lowry et al., 2000; Nolet et al., 2007; Schutt et al., 2008; Stachnik et al., 2008). Likewise the Yellowstone buoyancy flux is estimated to be an order of magnitude lower than its oceanic counterparts below Iceland and Hawaii, which have fluxes of 1.4 Mg/s and 8.7 Mg/s, respectively (Sleep, 1990). At 0.25 Mg/s, Yellowstone is comparable to the other continental hotspots with weak flux, calculated by Ritter (2004) to be 0.09 Mg/s at Eifel and 0.7 Mg/s at the Massif Central. A main consequence of such a weak flux is that the low volume of ascending magma and reduced excess temperature together produce less melting. The results are lower plume buoyancy and reduced impact on lithosphere uplift and magmatic volume (Waite, 2004).

If the anomaly is assumed to be a plume, there are two peculiarities that need to be addressed. One is the much larger volume and amplitude of the anomaly in the upper 200 km versus the lower 200 km of the upper mantle. The second is the northwest tilt of the anomaly with depth. The tilt is difficult to reconcile with plate motion and mantle flow models. Southeastward uppermost mantle flow can result in a plume dipping down to the northwest but predicts hotspot motion to the southeast. However, when combined with the plate motion vector, the base of the plume will be off to the NW of Yellowstone instead of along the Snake River Plain (Figure 29).

An alternate interpretation that cannot be ruled out is that the upper mantle velocity anomaly may be caused by magma rising along in a weak or thinned lithosphere. If lithosphere has been eroded along a preexisting structural weakness, then the upwelling could follow the path of least resistance to the surface. This idea has been invoked by some researchers to explain the dynamics of the Yellowstone system without a plume (e.g., Smith and Sbar, 1974; Favela and Anderson, 2000; Dueker et al., 2001; Christiansen et al., 2002).

The velocity anomaly in the upper 200 km is much larger than the anomaly in the range of 200 to 400 km depth. This type of contrast between the upper and lower 200 km of the upper mantle is not seen at Iceland, which is the best-imaged plume. Similarly, the Eifel plume has strong low $V_P$ anomaly to at least 400 km depth. It is possible that small-scale convection in the uppermost mantle may draw material up from greater depths below the YSRP. In fact, it may be necessary to draw material up, since the melt-depleted residuum is not expected to cycle back through the convection cell. It spreads laterally instead, making room for more mantle material to be drawn up. The extension of the Basin-Range enhances the effect and creates space for mantle to ascend.

Analog models of plumes by Whitehead (1982) showed that in a viscoelastic media plumes rise vertically. However, if the ascending material were bent over by more than 30° from the vertical, then the plume would break off from the original source, leaving a single, tilted feature that Whitehead (1982) called a “plumelet”. Such a scenario is consistent with mantle flow models and the geometry of the tomographically imaged Yellowstone plume. Steinberger and O’Connell (2000) constructed global maps of hotspot tracks in laterally varying large-scale mantle convection models and found that at transition zone depths beneath the western U.S. interior, the ascending flow geometry would have exceeded 30° tilt from the vertical, cutting off the heads of any pre-existing plumes. Thus Yellowstone may be a beheaded remnant of a stronger plume that could have originated at the core-mantle boundary. Such a feature would have originated in the lower mantle but was cut off by the high angle of tilt, leaving melt from a more limited thermal source in the transition zone. The remaining material would have a low buoyancy flux characteristic of a weaker plume.

The small buoyancy flux of the modeled Yellowstone plume is not enough to totally support the topography (e.g., Lowry et al., 2000). Compared with other hotspots, the eruption rate at Yellowstone is much too large to be attributed to its small buoyancy flux of 0.25 Mg/s. The same small-scale convection processes have been proposed for such features as Yellowstone, the St. George, UT, and Jemez, NM, volcanic trends, which are all parallel and trend to the northeast (Hernlund et al., 2008).

However, the buoyancy flux of Yellowstone is much larger than St. George and Jemez, as evidenced by the topographic features, eruptive volumes, and geoid anomaly. This suggests something different about Yellowstone, which can be satisfied by the plume component in the plume-convection hybrid model. The high $^3$He/$^4$He ratio, deep seismic anomaly, and thin transition zone are also satisfied by the plume component. The persistence of basaltic magmatism along the SRP for hundreds of kilometers from Yellowstone may be attributed to continued convection millions of years after the plate has passed the plume. A weak lineament in the lithosphere can help explain the apparent deflection of the plume, although we consider mantle flow a more plausible cause of deflection.

A model of plume-fed upper mantle convection generally agrees with our observations. However, other models argue for buoyant decompression melting instabilities in an extending lithosphere above regions of partially molten upper mantle (Lowry et al., 2000; Hernlund et al., 2008). These models have been proposed to account for some characteristics of intraplate volcanism in extensional lithospheric regimes including Yellowstone. Such models do not require spatially and temporally correlated volcanism and extension and may account for localized volcanic activity following Basin and Range extension in the western United States. We suggest that our seismic images of a conduit of melt from ~660 km argues for a plume geometry, not a shallow planar zone of decompression melting.

The well-known $^{87}Sr/^{86}Sr=0.706$ boundary (Farmer et al., 1983) separates accreted oceanic lithosphere to the west from continental cratonic lithosphere to the east. This boundary is also marked by sharp decreases in the normalized isotope ratios ∑Nd and ∑Hf found in Yellowstone silicic magmas, indicating a decrease in the mantle component of erupted materials (Nash et al., 2006). That is, as hotspot volcanism progressed from accreted to cratonic terrain, there was a fundamental change in magma composition, eruptive frequency, and temperature in association with the change in overriding lithosphere (Perkins and Nash, 2002). The configuration of subducting slab and thin oceanic lithosphere and thick continental lithosphere in the Pacific Northwest has important implications for the evolutions of Yellowstone hotspot volcanism.

In Fig. 28 we illustrate the development of the YSRPN in terms of the plume-convection model. The original voluminous plume head was vertical, rising from the deep mantle only to be entrained in westward return flow driven by the eastward subduction of the Juan de Fuca plate. The relatively weaker and thinner oceanic lithosphere allowed the plume head to spread out and protected the plume from the eastward currents that dominated upper mantle convective return flow below the thicker continental lithosphere to the east. As the North America plate progressed southwest it encountered the much thicker continental lithosphere and lost the protection of the back-arc geometry from large-scale mantle flow. Nash et al. (2006) showed that, based on geochemical data, the transition from accreted to cratonic lithosphere and a shift from westward to eastward mantle flow occurred at the Oregon-Idaho border. Here a plume with a conduit diameter of 70 km became caught in the mantle return flow, tilting it and smearing out the magma against the overriding lithosphere. This process was responsible for the YSRP hotspot track.

A further postulation of this model would be the southward offset of volcanism over time relative to the initial plume head position. The original Yellowstone-related silicic centers of volcanism proposed by several authors (Pierce and Morgan, 1992; Smith and Braile, 1994; Jordan et al., 2005) were associated with the McDermitt lava field of northern Nevada. Recent studies by Nash et al. (2006) and Camp and Ross (2004) argue for a more widely distributed area of initial silicic volcanism over southeastern Oregon. That is, later Yellowstone volcanism was offset to the south of initial volcanism in eastern Oregon. Alternately, if we assume a linear track for the base of the plume at 660 as well as the top of the plume, then the trace of the mantle source follows a southwest trend beneath the northern Rockies and the Idaho Batholith, ending below the western Snake River Plain, notably ~150 km north of the originally defined beginning of the YSRP, at the McDermitt, NV, volcanic field (Figure 29).

Our data and resulting model of the Yellowstone plume (Smith et al. 2003; Smith et al., 2005) is consistent with the area hypothesized by Camp and Ross (2004) to be affected by the plume head. This area encompasses much of the silicic volcanic area of the Oregon High Lava Plains and the southern part of the Columbia Plateau basalt field. This suggests that Columbia Plateau basalt outpouring that began at ~17 Ma may have had a common mantle source with the YSRP, i.e., the Yellowstone plume. This concept is also corroborated by the geochemical analysis of Hanan et al. (2008) who noted that the Steens basalt eruptive center may have been an early eruptive phase of the Columbia River basalts and is also located near our modeled location of the Yellowstone plume head at 17 Ma.

## 10. Concluding Remarks

The Yellowstone hotspot is a profound tectono-magmatic feature of the western U.S. that results from interaction of a mantle plume with the overriding North America plate. The hot, low-density Yellowstone plume head has sufficient buoyancy to induce a large topographic swell over the continental part of the hotspot track, now the Yellowstone swell. The high swell elevation imparts a high potential energy that causes southwest downhill flow of the lithosphere from Yellowstone driving compression along the eastern Snake River Plain and adding to the westward extension of the Basin-Range. Kinematically, the plume magma is sheared to the southwest against the southwest moving North American plate (Lowry et al., 2000) producing an elongate plume head beneath the SRP and Yellowstone. Regionally, lithospheric extension drives SW motion of the YSRP and is part of a larger kinematic pattern of clockwise rotation of the western U.S. whose motion is partially driven by the potential energy of the topographically high swell.

The southwest motion of the YSRP is one element of the gyre of clockwise rotation of deformation direction in the western U.S. The lithospheric extension associated with the Basin-Range tectonics further reduces the horizontal confining stress, amplifying magma ascent from plume to surface. Negative loading of the Snake River Plain by its mid crustal high density sill also produces flexure in the crust extending ~ 30 km SE beyond the SRP boundary. Along with lithospheric cooling, this contributes to systematic decrease in elevation with increasing age of silicic volcanism in a trend that extends from Yellowstone back to the hotspot origin in eastern Oregon.

Our results confirm that the Yellowstone volcanic field is the locus of the highest level of seismicity in the Rocky Mountains. Moreover it has experienced the largest historic earthquake, a1959 M7.5 event, of the Intermountain region. Local earthquake tomography images of Yellowstone confirm a low-Vp magma body beneath the caldera at 8-16 km, with 8-15% melts, i.e. the Yellowstone magma chamber. Heat flow of 2000 mW/m$^2$ and Yellowstone's Quaternary dominantly silicic volcanism from this crustal magma system drives Yellowstone's hydrothermal features.

Moreover, contemporary deformation of Yellowstone from geodetic measurements reveals an energetic system dominated by lithospheric extension of up to 4 mm/yr with superimposed volcanic uplift and subsidence with average rates of ~2 cm/yr. But the caldera has experienced an unexpected episode of accelerated uplift from 2004 to 2007 at up to 7 cm/yr that is attributed to magmatic recharge of the crustal magma system

Teleseismic tomography employing $V_p$ inversion imaged a P-wave low-velocity body from 80 to 250 km directly beneath Yellowstone, but continuing at a tilt of 60º northwest to the bottom of the transition zone at 660 km, 150 km west of Yellowstone. We interpret this body to be the Yellowstone plume. Dynamics of the plume reveal excess temperature of 85°-120°K and up to 1.5% melt with a relatively weak buoyancy flux of ~0.25 Mg/s that is several times smaller than oceanic plumes.

Employing the inclined plume-geometry and plate motion history, we extrapolate the Yellowstone mantle-source southwestward to its initial position at 17 million years beneath eastern Oregon and the southern part of the Columbia Plateau basalt field, which suggests a common source for the entire YSRPN system (Fig. 29). Our model is consistent with the original plume head rising vertically behind the subducting Juan de Fuca plate, but at ~12 million years it encountered cooler continental lithosphere and horizontal mantle flow, imparting the observed westward tilt.

Although this paper synthesizes a great deal of research to produce an integrated analysis of the Yellowstone plume and volcanic history of the Yellowstone hotspot, several issues still need to be addressed. The dynamics and mechanics of magma generation in the upper mantle and its subsequent transport from the tilted plume to the lithosphere and upper crust have not been resolved. The mantle plume contributes to the Yellowstone topographic swell and geoid anomaly, but the processes through which plume contributes regional extension at the surface and depth to allow magma emplacement requires further study. Hydrothermal activity is driven by heat from the crustal magma chamber, but the processes involved are poorly understood. More work needs to be done to understand the spatial distributions of thermal basins in the caldera, the changes in thermal activity that occur over time, and the thermal and mechanical connections between surface features and crustal magma. Changes in the caldera magmatic system through fluid transport (i.e., magma intrusion, dike injection, escape of volatiles, etc.) contribute to local deformation, and the resulting stress changes are hypothesized to affect nearby normal faults. Similarly, tectonic loading of Late Quaternary Yellowstone faults can affect the volcanic system. Stress interactions between faults and the volcanic system at short and long time scales remain poorly understood. As discussed in Section 4.4, the structure and thermal state of the lower crust is not known. All these topics are at present unknown, but they provide opportunities for investigation and quantitative modeling of the geochemical and geophysical characteristics of the Yellowstone hotspot.

The Yellowstone plume thus has had a profound effect on the western U.S. interior with hotspot-driven Cenozoic volcanism affecting lithospheric structure, stress state, deformation, and topography. Hotspot volcanism has produced the geology and environment that is used as the basis for designating the world’s first national park. The outstanding physical features of

Yellowstone National Park include its world-renowned hot springs and geysers.  These features are thermal phenomena that are driven by Yellowstone's extraordinarily high heat flow, which in turn is caused by its active magmatic sources.  For this reason we commonly say that "heat drives it all" in Yellowstone.  Moreover, we believe that our results demonstrate the dynamic properties of the Yellowstone hotspot.  Yellowstone caldera deformation and intense earthquake activity denote "a living, breathing, shaking" caldera.  In conclusion the contemporary volcanic and tectonic processes of Yellowstone demonstrate that it is truly "A Window into the Earth's Interior".

**Acknowledgements**

Collaborators in the Yellowstone Geodynamic Project included Eugene Humphreys, Paul Tackley, Paul Hernlund, and Ken Dueker.  Suzette Payne of the Idaho National Laboratory and Ronald Harris of Brigham Young University and their staffs, assisted with temporary GPS deployments.  Our project materially benefited with discussions and assistance from David Drobeck, Henry Heasler, Jake Lowenstern, David Lageson, Dan Dzurisin, Anthony Lowry, Barbara Nash, Michael Perkins, John Shervais, Lisa Morgan, Kenneth Pierce, Suzette Payne, David Rodgers, and Rick Hutchinson.  We appreciate the support with data acquisition of our Yellowstone projects from the National Science Foundation, the U.S. Geological Survey, Yellowstone and Grand Teton National Parks, the Idaho National Laboratory (INL), the Yellowstone Volcano Observatory and the Plate Boundary Observatory.  The University of Utah provided computational and technical assistance and the University of Utah Seismograph Stations supplied engineering support for seismic and GPS monitoring.  The IRIS-PASSCAL project portable seismographs and UNAVCO provided GPS instruments.  Our main Yellowstone hotspot project was primarily supported by the National Science Foundation Continental Dynamics program grants #EAR 9725431, 0314298, 9725431, and 9316289. Funding was also provided by William and Sue Carrico Foundation and by The Brinson Foundation.

**References**

Allen, R.M., Nolet, G., Morgan, W.J., Vogfjord, K., Bergsson, B.H., Erlendsson, P., Foulger, G.R., Jakobsdottir, S., Julian, B.R., Pritchard, M., Ragnarsson, S., Stefansson, R. 2002. Imaging the mantle beneath Iceland using integrated seismological techniques, J. Geophys. Res. 107: doi:10.1029/2001JB000595.

Anderson, D.L., J. L. Given, 1982. Absorption band Q model for the earth. J. Geophys. Res. 87: 3893-3904.

Anders M. H., Sleep N. H., 1992. Magmatism and extension: The thermal and mechanical effects of the Yellowstone hotspot. J. Geophys. Res. 97: 15,379–15,393.

Annen, C., Blundy, J. D., Sparks, R. S., 2006. The genesis of intermediate and silica magmas in deep crustal hot zones. J. Pet. 47: 505-539.

Armstrong, R. L., Leeman, W.P., Malde, H.E., 1975. K-Ar dating, Quaternary and Neogene volcanic rocks of the Snake River Plain, Idaho. Am. J. Sci. 275: 225-251.

Barth, A., Jordan, M., Ritter, J., 2007. Crustal and upper mantle structure of the French Massif Central plume. In: J.R.R. Ritter, U.R. Christensen, (Editors), Mantle Plumes - A Multidisciplinary Approach. Springer Verlag, Heidelberg, pp. 159-184.

Bassin, C., Laske, G., Masters, G., 2000. The current limits of resolution for surface wave tomography in North America. Eos Trans. AGU 81(48): F897.

Becker, T. W., Boschi, L., 2002. A comparison of tomographic and geodynamic mantle models. Geochem. Geophys. Geosys. 3(1): 1003, doi:10.1029/2001GC000168.

Becker, T.W., Chevrot, S., Schulte-Pelkum, V. Blackman, D.K., 2006. Statistical properties of seismic anisotropy predicted by upper mantle geodynamic models. J. Geophys. Res. 111: B08309, doi:10.1029/2005JB004095.

Bennett, R. A., Davis, J. L., Normandeau, J. E., Wernicke, B. P., 2001. Space geodetic measurements of plate boundary deformation in the western U.S. Cordillera. In: S. Stein, J. Freymueller (Editors), Plate Boundary Zones. AGU, Washington, D.C., pp. 27-55.

Beucler, E., Chevrot, S., Montagner, J. P. 1999. The Snake River Plain experiment revisited. Relationships between a Farallon plate fragment and the transition zone. Geophys. Res. Lett. 26: 2673-2676.

Bina C. R., Helffrich, G., 1994. Phase transition Clapeyron slopes and transition zone seismic discontinuity topography. J. Geophys. Res. 99: 15,853-15,860.

Birch, F., 1961. The Velocity of compressional waves in rocks to 10 kilobars, Part 2. J. Geophys. Res. 66(7): 2199-2224.

Blackwell, D. D., Negraru, P. T., Richards, M. C., 2006. Assessment of the enhanced geothermal system resource base of the United States. Nat. Resources Res. 15(4): 283-308, doi:10.1007/s11053-007-9028-7.

Boschi, L., Becker, T. W., Steinberger, B., 2007. Mantle plumes: Dynamic models and seismic images. Geochem. Geophys. Geosys. 8: Q10006, doi:10.1029/2007GC001733.

Braile, L. W., Smith, R.B., Ansorge, J., Baker, M. R. , Sparlin, M. A., Prodehl, C. M. Schilly, M.M., Healy, J. H. Mueller, S. Olsen, K. H. 1982. The Yellowstone Snake River Plain seismic profiling experiment: Crustal structure of the eastern Snake River Plain. J. Geophys. Res., 84: 2597-2610.

Burke, K., 1996. The African Plate. S. African J. Geol. 99: 339-409.

Burdick, S., Li, C., Martynov, V., Cox, T., Eakins, J., Mulder, T., Astiz, L., Vernon, F.L., Pavlis, G.L., van der Hilst, R., 2008. Upper mantle heterogeneity beneath North America from travel time tomography with global and USArray Transportable array data. Seismol. Res. Lettr. 79(3): 384-392.

Cammarano F., Goes S., Vacher P., Giardini D., 2003. Inferring upper mantle temperatures from seismic velocities. Phys. Earth Plan. Int., 138: 197-222.

Cammarano F., Romanowicz, B., 2007. Insights into the nature of the transition zone from physically constrained inversion of long-period seismic data. Proceedings Natl. Acad. Sci. U.S.A. 104(22): 9139-9144.

Camp, V. E., Ross, M. E., 2004. Mantle dynamics and genesis of mafic magmatism in the intermontane Pacific Northwest. J. Geophys. Res. 109: B08204, doi:10.1029/2003JB002838.

Carlson, R. W., Hart, W. K., 1988. Flood basalt volcanism in the northwestern United States. In: J. D. Macdougall (Editor), Continental Flood Basalts. Kluwer Academic Publishers, Dordrecht, The Netherlands, p. 35-61.

Chang, W. L., Smith, R. B., 2002. Integrated seismic-hazard analysis of the Wasatch Front, Utah. Bull. Seis. Soc. Am. 92(5): 1904-1922.

Chang, W. L., Smith, R. B., 2005, Lithospheric rheology from postseismic deformation of a M=7.5 normal-faulting earthquake with implications for continental kinematics. 2005 Salt Lake City Annual Meeting, Geol. Soc. Amer., Abs. 225-4.

Chang, W. L., Smith, R. B., 2008. Lithospheric rheology from postseismic deformation of a M=7.5 normal-faulting earthquake with implications for continental kinematics. J. Geophys. Res. in press.

Chang, W., Smith, R.B., Wicks, C., Puskas, C., Farrell, J., 2007. Accelerated uplift and source models of the Yellowstone caldera, 2004-2006, from GPS and InSAR observations, Science 318(5852): 952-956, doi:10.1126/science.1146842.

Christiansen, R. L., 2001. The Quaternary and Pliocene Yellowstone Plateau volcanic field of Wyoming, Idaho, and Montana. U. S. Geol. Surv. Prof. Pap. 729-G, U. S. Geol. Surv., Denver, CO, 120 pp.

Christiansen R. L., Foulger G. R., Evans J. R., 2002. Upper-mantle origin of the Yellowstone hotspot. GSA Bull. 114: 1245–1256.

Christiansen, R.L., McKee, E.H., 1978. Late Cenozoic volcanic and tectonic evolution of the Great Basin and Columbia intermontane regions. In: R. B. Smith, and G. P. Eaton (Editors), Cenozoic Tectonics and Regional Geophysics of the Western Cordillera: Geological Society of America Memoir 152. GSA, Boulder, CO, pp. 283-311.

Clawson, S. R., Smith, R. B. Benz, H.M., 1989. P-wave attenuation of the Yellowstone caldera from three-dimensional inversion of spectral decay using explosion source seismic data. J. Geophys. Res. 94: 7205-7222.

Craig, H., Lupton, J. E., Welhan, J. A., Poreda, R., 1978. Helium isotope ratios in Yellowstone and Lassen Park volcanic gases. Geophys. Res. Lett. 5(11): 897-900.

Crampin S., Chastin S., 2003. A review of shear wave splitting in the crack-critical crust. Geophys. J. Int. 155: 221-240.

Crotwell, H. P., Owens, T. J., 2005. Automated receiver function processing. Seis. Res. Lett. 76(6): 702-713.

Crough, S.T., 1978. Thermal origin of mid-plate hot-spot swells. Geophys. J. Royal Astron. Soc. 55: 451-469.

Davies, G. F., 1988. Dynamic Earth: Plates, Plumes and Mantle Convection. Cambridge University Press, Cambridge, 458 pp.

DeNosaquo, K., Smith, R.B., Lowry, A.R., 2008. Density and lithospheric strength models of the Yellowstone-Snake River Plain volcanic system from gravity and heat flow data, J. Vol. Geotherm. Res. (this volume).

Dietz, R.S., Holden, J. C., 1970. Reconstruction of Pangaea: Breakup and dispersion of continents, Permian to present. J. Geophys. Res. 75: 4939-4956

Doe, B. R., Leeman, W. P., Christiansen, R. L., Hedge, C. E., 1982. Lead and strontium isotopes and related trace elements as genetic tracers in the upper Cenozoic rhyolite-basalt association of the Yellowstone plateau volcanic field. J. Geophys. Res. 87(B6): 4785-4806.

Doser, D. I., 1985. Source parameters and faulting processes of the 1959 Hebgen Lake, Montana, earthquake sequence. J. Geophys. Res. 90: 4537-4555.

Dueker, K. G., Sheehan, A. F., 1997. Mantle discontinuity structure from mid-point stacks of converted P to S waves across the Yellowstone Hotspot Track. J. Geophys. Res. 102(B4): 8313-8327.

Dueker, K., Yuan, H., Zurek, B., 2001. Thick-structured Proterozoic lithosphere of the Rocky Mountain region. GSA Today 11: 4-9.

Dzurisin, D., Yamashita K. M., 1987. Vertical surface displacements at Yellowstone caldera, Wyoming, 1976-1986. J. Geophys. Res. 92: 13,753-13,766.

Evans, J.R., Achauer, U., 1993. Teleseismic velocity tomography using the ACH-method. Theory and application to continental scale studies. In: H.M. Iyer and K. Hirahara (Editors), Seismic Tomography Theory and Practice. Chapman and Hall, London, pp. 319–360.

Farmer, G., DePaolo, D. 1983. Origin of Mesozoic and Tertiary Granite in the Western United States and Implications for Pre-Mesozoic Crustal Structure 1. Nd and Sr Isotopic Studies in the Geocline of the Northern Great Basin. J. Geophys. Res. 88(B4): 3379-3401.

Farnetani, C. G., Samuel, H., 2005. Beyond the thermal plume paradigm. Geophys. Res. Lett. 32: L07311, doi:10.1029/2005GL022360.

Farrell, J. M., 2007. Space-time seismicity and development of a geographical information system database with interactive graphics for the Yellowstone region. Masters Thesis, University of Utah, Salt Lake City, Utah.

Favela, J., Anderson, D. L., 2000. Extensional tectonics and global volcanism. In: E. Boschi, G. Ekstrom, A. Morelli, (Editors), Problems in geophysics for the new millennium. Editrice Compositori, Bologna, pp. 463–498.

Fee, D., Dueker K., 2004. Mantle transition zone topography and structure beneath the Yellowstone hotspot. Geophys. Res. Lett. 31: L18603, doi:10.1029/2004GL020636.

Faul, U. H., Toomey, D. R., Waft, H. S., 1994. Late granular basaltic melt is distributed in thin, elongated inclusions. Geophys. Res. Lett. 21: 29-32.

Flesch, L. M., Holt, W. E., Haines, A. J., Shen-Tu, B., 2000. Dynamics of the Pacific-North American plate boundary zone in the western United States. Science 287: 834-836.

Fournier, R. O., 1989. Geochemistry and dynamics of the Yellowstone National Park hydrothermal system. Ann. Rev. Earth Plan. Sci. 17: 13-53.

Fournier, R. O., Pitt, A. M., 1985. The Yellowstone magmatic-hydrothermal system, U.S.A. In: C. Stone (Editor), 1985 International Symposium on Geothermal Energy. Geothermal Resource Center, Davis, CA, pp. 319-327.

Geist, D., Richards, M., 1993. Origin of the Columbia Plateau and Snake River Plain: Deflection of the Yellowstone plume. Geology 21: 789-792.

Grand, S. P., van der Hilst, R. D., Widiyantoro, S., 1997. Global seismic tomography: A snapshot of convection in the Earth. GSA Today 7: 1–7.

Griffiths, R. W., Campbell, I. H., 1990. Stirring and strucutre in mantle starting plumes. Earth. Plan. Sci. Lett. 99(1-2): 67-78.

Gripp, A. E., Gordon, R. G., 2002. Young tracks of hotspots and current plate velocities. Geophys. J. Int. 150: 321-361.

Hager, B. H., O’Connell, R. J., 1979. Kinematic models of large-scale flow in the earth’s mantle. J. Geophys. Res. 84(B3): 1031-1048.

Hager, B. H., O’Connell, R. J., 1981. A simple global model of plate dynamics and mantle convection. J. Geophys. Res. 86(B6): 6003-6015.

Haines, A. J., Holt, W. E., 1993. A procedure for obtaining the complete horizontal motions within zones of distributed deformation from the inversion of strain rate data. J. Geophys. Res. 98(B7): 12,057-12,082.

Haines, A. J., Jackson, J. A., Holt, W. E., Agnew, D. C., 1998. Representing distributed deformation by continuous velocity fields. Sci. Rept. 98/5. Inst. Of Geol. and Nucl. Sci., Wellington, New Zealand.

Haller, K. M., Wheeler, R. L., Rukstales, K. S., 2002. Documentation of changes in fault parameters for the 2002 National Seismic Hazard Maps-Conterminous United States except California, U. S. Geol. Surv. Open-File Rep. 02-467. U. S. Geol. Surv., Denver, CO, 34 pp.

Hammond, W.C., Humphreys, E.D., 2000. Upper mantle seismic wave velocity: Effects of realistic partial melt geometries. J. Geophys. Res. 105: 10,975-10,986.

Hanan, B. B., Shervais, J. W., Vetter, S. K., 2008. Yellowstone plume-continental lithosphere interaction beneath the Snake River Plain. Geology 36: 51-54.

Hart, W.K., Carlson, R.W., 1987. Tectonic controls on magma genesis and evolution in the northwestern United States. J. Volc. Geotherm. Res. 32: 119–135.

Hernlund, J.W., Tackley, P.J., Stevenson, D.J., 2008. Bouyant melting instabilities beneath extending lithosphere:1 Numerical models. J. Geophy. Res. 113: B04405, doi:10.1029/2006JB004862.

Hill, D. P., 1992. Temperatures at the base of the seismogenic crust beneath the Long Valley caldera, California, and the Phlegrean fields caldera, Italy. In: P. Gasparini (Editor), Proceedings in Volcanology: Volcanic Seismology Vol. 3. Springer-Verlag, Berlin, pp. 432-460.

Hill, D. P., Reasenberg, P. A., Michael, A., Arabasz, W. J., Beroza, G., Brumbaugh, D., Brune, J. N., Castro, R., Davis, S., dePolo, D., Ellsworth, W. L., Gomberg, J., Harmsen, S., House, L., Jackson, S. M., Johnston, M. J. S., Jones, L., Keller, R., Malone, S., Munguia, L., Nava, S., Pechmann, J. C., Sanford, A., Simpson, R. W., Smith, R. B., Stark, M., Stickney M., Vidal, A., Walter, S., Wong, V., Zollweg, J., 1993. Seismicity Remotely Triggered by the Magnitude 7.3 Landers, California, Earthquake. Science, 260(5114): 1617-1623, doi:10.1126/science.260.5114.1617.

Hildreth, W., Halliday, A.N. and Christiansen, R.L., 1991. Isotopic and chemical evidence concerning the genesis and contamination of basaltic and rhyolitic magma beneath the Yellowstone Plateau volcananic field. J. Pet. 32: 63-138.

Holdahl, S. R., Dzurisin, D., 1991. Time-dependent models of vertical deformation for the Yellowstone-Hebgen Lake region, 1923-1987. J. Geophys. Res. 96(B2): 2465-2483.

Humphreys, E. D., Dueker, K. G., Schutt, D. L., Smith, R. B., 2000. Beneath Yellowstone: Evaluating plume and nonplume models using teleseismic images of the upper mantle. GSA Today 10(12): 1-7.

Husen, S., Smith, R. B., 2004. Probabilistic earthquake relocation in three-dimensional velocity models for the Yellowstone National Park Region, Wyoming. Bull. Seis. Soc. Am. 94(3): 880-896.

Husen, S., Smith, R. B., Waite, G. P., 2004. Evidence for gas and magmatic sources beneath the Yellowstone volcanic field from seismic tomographic imaging. J. Volc. and Geotherm. Res. 131: 397-410, doi:10.1016/S0377-0273(03)00416-5.

Husen, S., Taylor, R., Smith, R. B., Healser, H., 2004. Changes in geyser behavior and remotely triggered seismicity in Yellowstone National Park produced by the 2002 M7.9 Denali fault earthquake. Geology 32: 537-540.

Husen, S., Weimer, S., Smith, R. B., 2004. Remotely triggered seismicity in the Yellowstone National Park region by the 2002 MW 7.9 Denali Fault Earthquake, Alaska. Bull. Seism. Soc. Am. 94(6B): S317-S331.

Ito, G., van Keken, P.E., 2007. Hotspots and melting anomalies. In: D. Bercovici (Editor), Mantle Dynamics, Treatise on Geophysics v. 7. Elsevier Press, Amsterdam, The Netherlands.

Iyer, H.M., Evans, J. R., Zandt, G., Stewart, R. M., Coakley, J. M., Roloff, J. N., 1981. A deep low-velocity body under the Yellowstone caldera, Wyoming: Delineation using teleseismic P-wave residuals and tectonic interpretation: Summary. Geol. Soc. of Am. Bull., 92,(11): 792-798.

Jackson, I., Paterson, M. S., Fitzgerald, J. D., 1992. Seismic wave dispersion and attenuation in Aheim dunite: an experimental study. Geophys. J. Int. 108: 517-534.

Jordan, M., 2003. JI-3D A new approach to high resolution regional seismic tomography: theory and applications. PhD thesis, University of Göttingen, Göttingen, Germany.

Jordan, M., Smith, R. B., Waite, G. P., 2004. Tomographic Images of the Yellowstone Hotspot Structure. Eos Tran. AGU 85(47), Fall Meet. Suppl., Abstract V51B-0556.

Jordan, M., Smith, R. B., Puskas, C., Farrell, J., Waite, G., 2005. The Yellowstone hotspot and related plume: volcano-tectonics, tomography, kinematics and mantle flow. Eos Trans. AGU, 86(52), Fall Meet. Suppl., Abstract T51D-1388.

Karato, S., 1993. Importance of anelasticity in the interpretation of seismic tomography. Geophys. Res. Lett. 20: 1623-1626.

Karato S., Jung, H., 1998. Water, partial melting and the origin of the seismic low velocity and high attenuation zone in the upper mantle. Earth Planet. Sci. Lett. 157: 193–207.

Kawamoto T., Holloway, J., 1997. Melting temperature and partial melt chemistry of H2O–saturated mantle peridotite to 11 gigapascals. Science 276: 240–243.

Kennedy, B.M., Lynch, M.A., Reynolds, J.H., Smith, S.P., 1985. Intensive sampling of noble gases in fluids at Yellowstone: I. Early overview of the data; regional patterns. Geochim. Cosmochim. Acta 49: 1251–1261.

Kennett, B. L. N. Engdahl, E. R., 1991. Traveltimes for global earthquake location and phase identification. Geophy. J. Int. 105(2): 429–465, doi:10.1111/j.1365-246X.1991.tb06724.x.

King, S. D., Anderson, D. L., 1995. An alternative mechanism of flood basalt formation. Earth and Plan. Sci. Lett. 136(3-4): 269-279.

Leeman, W.P., 1982. Development of the Snake River Plain-Yellowstone Plateau province, Idaho and Wyoming: An overview and petrologic model. In: B. Bonnichsen and R.M. Breckenridge (Editors), Cenozoic Geology of Idaho: Idaho Bureau of Mines and Geology Bulletin 26. Idaho Bureau of Mines and Geology, Moscow, ID, pp. 155-178.

Lees, J., VanDecar, J., 1991. Seismic tomography constrained by bouguer gravity anomalies: Applications in western Washington, Pure App. Geophys. 135: 31-52.

Lehman, J. A., Smith, R.B., Schilly, M.M, Braile, L.W., 1982. Crustal structure of the Yellowstone caldera from delay-time analyses and correlation with gravity data. J. Geophys. Res. 84: 2713-2730.

Lowenstern, J. B., Hurwitz, S., 2008. Monitoring a supervolcano in repose: Heat and volatile flux at the Yellowstone caldera, Elements, DOI: 10.2113/GSELEMENTS.4.1.35.

Lynch, D., Smith, R. B., Benz, H. M., 1997. Three-dimensional tomographic inversion of crust and upper mantle structure of the eastern Basin Range-Rocky Mountain transition from earthquake and regional refraction data. Abstracts from the 9th Annual IRIS Workshop, IRIS Consortium, Breckenridge, CO.

Lowry, A. R., Ribe, N. M., Smith, R. B., 2000. Dynamic elevation of the Cordillera, western United States. J. Geophys. Res. 105(B10): 23,371-23,390.

McCaffrey, R., 2000. Rotation and plate locking at the southern Cascadia subduction zone. Geophys. Res. Lett. 27(19): 3117-3120.

McCaffrey, R., Qamar, A. I., King, R. W., Wells, R., Ning, Z., Williams, C. A., Stevens, C. W., Vollick, J. J., Zwick, P. C., 2007. Plate coupling, block rotation and crustal deformation in the Pacific Northwest. Geophys. J. Int., in press.

McCalpin, J. P., Nishenko, S. P., 1996. Holocene paleoseismicity, temporal clustering, and probabilities of future large (M>7) earthquakes on the Wasatch fault zone, Utah. J. Geophys. Res. 101: 6233-6253.

Meade, B. J., Hager, B. H., 2005. Block models of crustal motion in southern California constrained by GPS measurements. J. Geophys. Res. 110: B03403, doi:10.1029/2004JB003209.

Megnin, C., Romanowicz, B., 2000. The three-dimensional shear velocity structure of the mantle from the inversion of body, surface and higher-mode waveforms. Geophys. J. Int. 143(3): 709-728, doi:10.1046/j.1365-246X.2000.00298.x.

Milbert, D.G., 1991. Computing GPS-derived orthometric heights with the GEOID90 geoid height model. Technical Papers of the 1991 ACSM-ASPRS Fall Convention. American Congress on Surveying and Mapping, Washington, D.C., pp. A46-55.

Miller, D. S., Smith, R. B., 1999. P and S velocity structure of the Yellowstone volcanic field from local earthquake and controlled-source tomography. J. Geophys. Res. 104: 15,105-15,121.

Montelli, R., Nolet, G., Dahlen, F., Masters, G., Engdahl, E. R. & Hung, S. H., 2004. Finite-frequency tomography reveals a variety of plumes in the mantle. Science 303: 338-343, doi:10.1126/science.1092485.

Morgan, W.J., 1972. Plate motions and deep mantle convection. Geol. Soc. Am. Memoir 132: 7-22.

Morgan, J. P., Morgan, W. J., Price, E., 1995. Hotspot melting generates both hotspot volcanism and a hotspot swell? J. Geophys. Res. 100: 8045-8062.

Morgan, P. Blackwell, ., D. D., Spafford R. E., Smith, R.B., 1977. Heat flow measurements in Yellowstone Lake and the thermal structure of the Yellowstone Caldera. J. Geophys. Res. 82: 379-3732.

Mueller, I.I., 1991. The International GPS Geodynamics Service. GPS Bull. 4: 7-16.

Nabelek, J., Xia, G., 1995. Moment-tensor analysis using regional data: application to the 25 March, 1993, Scotts Mills, Oregon, earthquake. Geophys. Res. Lett. 22(1): 13–16.

Nash, B. P., Perkins, M. E., Christensen, J. N., Lee, D. C., Halliday, A, 2006. The Yellowstone hotspot in space and time: Nd and Hf isotopes in silicic magmas. Earth and Plan. Sci. Lett. 247(1-2): 143-156.

Nolet, G. R. Allen, D. Zhao, D., 2007. Mantle plume tomography. Geochem. Geol. 241: 248-263, doi: 10.1016/j.chemgeo.2007.01.022.

Nolet, G., Karato. S., Montelli, R., 2006. Plume fluxes from seismic tomography. Earth and Plan. Sci. Lett. 248: 685-699.

Olson, P., Singer, H., 1985. Creeping plumes. J. Fluid Mech. 158: 511-531.

Parsons, T., Thompson, G. A., Smith, R. P., 1998. More than one way to stretch: a tectonic model for extension along the plume track of the Yellowstone hotspot and adjacent Basin and Range Province. Tect. 17(2): 221-234.

Pelton, J.R., Smith, R.B., 1982. Contemporary vertical surface displacements in Yellowstone National Park. J. Geophys. Res. 87: 2745-2761.

Peng, X. and Humphreys, E.D., 1998. Crustal velocity structure across the eastern Snake River Plain and the Yellowstone swell. J. Geophys. Res., 103: 7171-7186.

Perkins, M. E., Nash, B. P., 2002. Explosive silicic volcanism of the Yellowstone hotspot: the ash fall tuff record. Geol. Soc. Am. Bull. 114(3): 367-381.

Pierce, K. L., Morgan, L. A., 1992. The track of the Yellowstone hot spot: Volcanism, faulting, and uplift. In: P.K. Link, M.A. Kuntz, L.B. Platt (Editors), Regional Geology of Eastern Idaho and Western Wyoming: Geological Society of America Memoir 179. Geological Society of America, Boulder, CO, pp. 1-53.

Pitt, A. M., Weaver, C. S., Spence, W., 1979. The Yellowstone Park earthquake of June 30, 1975. Bull. Seismol. Soc. Am. 69: 187-205.

Priestly, K., Orcutt, J., 1982. Extremal travel time inversion of explosion seismology data from the eastern Snake River Plain, Idaho. J. Geophys. Res. 87: 2634-2642.

Puskas, C. M., Smith, R. B., Meertens, C. M., Chang, W. L., 2007. Crustal deformation of the Yellowstone-Snake River Plain volcanic system: campaign and continuous GPS observations, 1987-2004. J. Geophys. Res. 112: B03401, doi:10.1029/2006JB004325.

Puskas, C. M., Smith, R. B., Flesch, L. M., Settles, K,. 2007. Effects of the Yellowstone Hotspot on western U.S. Stress and Deformation. Eos Trans. AGU 88(52), Fall Meet. Suppl., Abstract V51F-04.

Puskas, C. M., Smith, R. B., 2008. Intraplate Deformation and Microplate Tectonics of the Yellowstone Hotspot. Earth Plan. Sci. Lett., (submitted).

Richards, M. A., Griffiths, R. W., 1988. Deflection of plumes by mantle shear flow: experimental results and a simple theory. Geophys. J. Int. 94(3): 367-376, doi:10.1111/j.1365-246X.1988.tb02260.x.

Ritter, J. R. R., 2004. Small-scale mantle plumes: imaging and geodynamic aspects. In: K. Fuchs, F. Wenzel (Editors), Challenges for Earth Sciences in the 21st Century. Springer Verlag, Berlin.

Rodgers, D. W., Hackett, W. R., Ore, H. T., 1990. Extension of the Yellowtone Plateau, eastern Snake River Plain, and Owyhee plateau. Geol. 18: 1138-1141.

Ruppel, E.T., 1972. Geology of pre-Tertiary rocks in the northern part of Yellowstone National Park, Wyoming, with a section on Tertiary laccoliths, sills, and stocks in and near the Gallatin Range, Yellowstone National Park. Geology of Yellowstone National Park: U.S. Geol. Surv. Prof. Pap. 729-A, U.S. Geolo. Surv., Denver, CO, 66 pp.

Saltzer, R. L., Humphreys, E. D., 1997. Upper mantle P wave velocity structure of the eastern Snake River Plain and its relationship to geodynamic models of the region. J. Geophys. Res. 102: 11,829-11,841.

Schmitz, M., Heinshohn, W. D., Schilling, F. R., 1997. Seismic, gravity and petrological evidence for partial melt beneath the thickened Central Andean crust (21-23°S). Tectonophys. 270(3-4): 313-326, doi:10.1016/S0040-1951(96)00217-X.

Schutt D. L., K. Dueker, H. Yuan, 2008. Crust and upper mantle velocity structure of the Yellowstone hot spot and surroundings. J. Geophys. Res. 113: B03310, doi:10.1029/2007JB005109.

Schutt, D.L., Humphrey, E.D., 2004. P and S wave velocity and V-P/V-S in the wake of the Yellowstone hot spot. J. Geophys. Res. 109: B01305, doi:10.1029/2003JB002442.

Shervais, J.W., Vetter, S.K. and Hanan, B.B., 2006. Layered mafic sill complex beneath the eastern Snake River Plain: Evidence from cyclic geochemical variations in basalt. Geology, 34: 365-368.

Sigloch, K., McQuarrie, N., Nolet, G., 2008. Two-stage subduction history under N. America inferred from multiple-frequency tomography. Nature Geoscience, (in press).

Sillard, P., Altamimi, Z., Boucher, C., 1998. The ITRF96 realization and its associated velocity field. Geophys. Res. Lett. 25: 3223-3226, doi: 10.1029/98GL52489.

Simmons, N. A., Forte, A. M., Grand, S. P., 2006. Constraining mantle flow with seismic and geodynamic data: a joint approach. Earth Plan. Sci. Lett. 46: 109-124.

Sleep, N. H., 1990. Hotspots and mantle plumes: some phenomenology. J. Geophys. Res. 95(B5): 6715-6736.

Smith, R. B., 1977. Intraplate tectonics of the Western North American Plate. Tectonophys. 37: 323-336.

Smith, R. B., Braile, L. W., Schilly, M. M., Ansorge, J., Prodehl, C., Baker, M. Healey, J. H. Mueller, S. Greensfelder, R., 1982. The Yellowstone- eastern Snake River Plain seismic profiling experiment: Crustal structure of Yellowstone, J. Geophys. Res., 84, 2583-2596.

Smith, R. B., Arabasz, W. J., 1991. Seismicity of the Intermountain Seismic Belt. In: D.B. Slemmons, E.R. Engdahl, M.L. Zoback, and D.D. Blackwell (Editors), Neotectonics of North America. Geological Society of America, Boulder, CO, pp. 185-228.

Smith, R. B., Braile, L. W. 1993. Topographic signature, space-time evolution, and physical properties of the Yellowstone-Snake River Plain volcanic system: the Yellowstone hotspot, In: A. W. Snoke, J. Steidtmann, S. M. Roberts (Editors), Geology of Wyoming: Geological Survey of Wyoming Memoir No. 5, Wyoming State Geological Survey, Laramie, WY, p. 694-754.

Smith, R. B., Braile, L. W., 1994. The Yellowstone hotspot. J. Volc. and Geotherm. Res. 61: 121-187.

Smith, R. B., Bruhn, R. L., 1984. Intraplate extensional tectonics of the eastern Basin-Range: inferences on structural style from seismic reflection data, regional tectonics, and thermal-mechanical models of brittle-ductile deformation. J. Geophys. Res. 89(B7): 5733-5762.

Smith, R.B., Siegel, L., 2000. Windows into the Earth's interior; The geologic story of Yellowstone and Grand Teton National Parks, Oxford University Press, 242 pp.

Smith, R. B., Jordan, M., Puskas, C., Waite, G. Farrell, J., 2005. Geodynamic models of the Yellowstone Hotspot constrained by seismic and GPS imaging and volcano-tectonic data. 2005 Salt Lake City Annual Meeting, Geol. Soc. Amer., Abstract 54-2.

Smith, R.B. Sbar, M., 1974. Contemporary tectonics and seismicity of the Western United States with emphasis on the Intermountain Seismic Belt. Geol. Soc. Am. Bull. 85: 1205-1218.

Smith, R. B., Blackwell, D.D., 2000. Heat flow and energetics of Yellowstone Lake hydrothermal systems. Eos Trans. AGU 81(48), Fall Meet. Suppl., Abstract V22F-17.

Smith, R. B., G. P. Waite, C. M. Puskas, D.L. Shut and E.D. Humphreys, 2003, Dynamic and kinematic models of the Yellowstone Hotspot constrained by seismic anisotropy, GPS measurements and fault slip rates. Eos. Trans. AGU 84(86), Fall Meet. Suppl., Abstract T51G-05.

Smith, R. P., Jackson, S. M. and Hackett W. R., 1996. Paleoseismology and seismic hazards evaluations in extensional volcanic terrains. J. Geophys. Res. 101(B3): 6277–6292.

Sparlin, M. A., Braile, L. W., Smith, R. B., 1982. Crustal structure of the eastern Snake River Plain determined from ray trace modeling of seismic refraction data. J. Geophys. Res. 87(B4): 2619-2633.

Steck, L.K., Prothero, W.A., 1991. A 3-D raytracer for teleseismic body-wave arrival times. Bull. Seis. Soc. Am. 81: 1332–1339.

Steinberger, B., 2000. Plumes in a convecting mantle: models and observations from individual hotspots. J. Geophys. Res. 105: 11,127-11,152.

Steinberger, B., Antretter, A., 2006. Conduit diameter and buoyant rising speed of mantle plumes: implications for the motion of hot spots and shape of plumr conduits. Geochem. Geophys. Geosys. 7: Q11018, doi:10.1029/2006GC001409.

Steinberger, B., Calderwood, A. R., 2006. Models of large-scale viscous flow in the Earth's mantle with constraints from mineral physics and surface observations. Geophys. J. Int. 167: 1461-1481.

Steinberger, B., O'Connell, R.J., 1998. Advection of plumes in mantle flow; implications for hot spot motion, mantle viscosity and plume distribution. Geophys. J. Int. 132: 412-434.

Steinberger, B., O'Connell, R. J., 2000. Effects of mantle flow on hotspot motion. Geophys. Mono. 121: 377-398

Steinberger, B., Sutherland, R., O'Connell, R. J., 2004. Prediction of Emperor-Hawaii seamount locations from a revised model of global plate motion and mantle flow. Nature 430: 167-173.

Tarantola, A., Valette, B., 1982. Generalized nonlinear inverse problems solved using the least squares criterion. Rev. Geophys. Space Phys. 20: 219–232.

Tapley, B., Ries, J., Bettadpur, S., Chambers, D., Cheng, M., Condi, F., Gunter, B., Kang, Z., Nagel, P., Pastor, R., Pekker, T., Poole, S., Wang, F., 2005. GGM02 – An improved Earth gravity field model from GRACE. J. Geod. 79: 467-478, doi:10.1007/s00190-005-0480-z.

Thatcher, W., 2003. GPS constraints on the kinematics of continental deformation. Int. Geol. Rev. 45: 191-212.

Tsuboi, C., 1954. A new and simple method for calculating the deflections of the vertical from gravity anomalies with the aid of BESSEL FOURIER series, Proceedings of the Japan Academy 30(6): 461-466.

van der Hilst, R.D., De Hoop, M.V., 2005. Banana-doughnut kernels and mantle tomography. Geophys. J. Int. 163: 956– 961.

Vasco, D.W., Johnson, L. R., Goldstein, N. E., 1988. Using surface displacement and strain observations to determine deformation at depth, with an application to Long Valley Caldera, California. J. Geophys. Res. 93: 3232-3242.

Vasco, D. W., Puskas, C. M., Smith, R. B., Meertens, C. M., 2007. Crustal deformation and source models of the Yellowstone volcanic field from geodetic data. J. Geophys. Res. 112: B07402, doi:10.1029/2006JB004641.

Vasco, D. W., Smith, R., Taylor, C., 1990. Inversion of Yellowstone vertical displacements and gravity changes, 1923 to 1975-1977 to 1986. J. Geophys. Res. 95: 19,839-19,856.

Waite, G. P., 1999. Seismicity of the Yellowstone Plateau: Space-time patterns and stresses from focal mechanism inversion. M.S. thesis, University of Utah, Salt Lake City, UT.

Waite, G. P., 2004. Upper mantle structure of the Yellowstone hotspot from teleseismic body-wave velocity tomography and shear-wave anisotropy. Ph.D dissertation, University of Utah, Salt Lake City, Utah.

Waite, G. P., Chang, W., 2007. Shear-wave splitting from local earthquakes as an indicator of crustal stress at Yellowstone. Eos Trans. AGU 88(52), Fall Meet. Suppl., Abstract V3B-1319.

Waite, G. P., Schutt, D. L., Smith R. B., 2005. Models of lithosphere and asthenosphere anisotropic structure of the Yellowstone hot spot from shear wave splitting. J. Geophys. Res. 110: B11304, doi:1029/2004JB003501.

Waite, G. P., Smith, R. B., 2002. Seismic evidence for fluid migration accompanying subsidence of the Yellowstone caldera. J. Geophys. Res. 107(B9): 2177, doi:10.1029/2001JB000586.

Waite, G. P., Smith R. B., 2004. Seismotectonics and stress field of the Yellowstone volcanic plateau from earthquake first motions and other indicators. J. Geophys. Res. 109: B02301, doi:1029/2003JB002675.

Waite, G. P., Smith, R. B., Allen, R. M., 2006. Vp and Vs structure of the Yellowstone hot spot: evidence for an upper mantle plume. J. Geophys. Res. 111(B4): B04303, doi:10.1029/2005JB003867.

Wells D. L. Coppersmith K. J., 1994. New empirical relationships among magnitude, rupture length, rupture width, rupture area, and surface displacement. Bull. Seis. Soc. Am. 84: 974-1002.

White, B. J. P., Smith, R. B., Farrell, J., Husen, S., Wong, I., 2008. Seismicity and earthquake hazard analysis of the Teton-Yellowstone region, Wyoming. J. Vol. Geotherm. Res., (this volume).

Whitehead, J. A., 1982. Instabilities of fluid conduits in a flowing Earth: are plates lubricated by the asthenosphere? Geophys. J. R. Astr. Soc. 70: 415–433.

Whitehead, J. A., Luther, D. S., 1975. Dynamics of laboratory diapir and plume models. J. Geoophys. Res. 80(B5): 705-717.

Wicks, C., Thatcher, W., Dzurisin, D., 1998. Migration of fluids beneath Yellowstone caldera inferred from satellite radar interferometry. Science 282(5388): 458-462, doi:10.1126/science.282.5388.458.

Wicks, C., Thatcher, W., Dzurisin, D., Svarc, J., 2006. Uplift, thermal unrest and magma intrusion at Yellowstone caldera. Nature 440: 72-75, doi:10.1038/nature04507.

Wilson, J. T., 1963. A possible origin of the Hawaiian Islands. Can. J. Phys. 41: 863-870.

Wolfe, C. J., Solomon, S. C., Silver, P. G., VanDecar, J. C. and Russo, R. M., 2002. Inversion of body-wave delay times for mantle structure beneath the Hawaiian islands: results from the PELENET experiment. Earth Planet. Sci. Lett. 198: 129-145.

Wüllner, U., Christensen, U. R., M. Jordan, 2006. Joint geodynamical and seismic modeling of the Eifel plume. Geophys. J. Int. 165(1): 357–372, doi:10.1111/j.1365-246X.2006.02906.x

Xue, M., R.M. Allen, 2007. The fate of the Juan de Fuca plate: Implications for a Yellowstone plume head. Earth Planet. Sci. Lett., 264(1): 266-276.

Yuan, H., Dueker, K., 2005. Teleseismic P-wave tomogram of the Yellowstone plume. Geophys. Res. Lett. 32: L07304, doi:10.1029/2004FL022056.

Zeyen, H., Achauer, U., 1997. Joint inversion of teleseismic delay times and gravity anomaly data for regional structures: theory and synthetic examples. In: K. Fuchs (Editor), Upper Mantle Heterogeneities from Active and Passive Seismology. Kluwer Academic Publishers, Dordrecht, Netherlands, pp. 155-168.

Zoback, M. D., Zoback, M. L., 1991. Tectonic stress field of North America and relative plate motions. In: D. B. Slemmons, E. R. Engdahl, M. D. Zoback, D. D. Blackwell (Editors), Neotectonics of North America. Geological Society of America, Boulder, CO, p. 339-366.

**Table Captions**

**Table 1.** Table of the B-values and density variations based on the geoid modelling and the results of the optimized tomographic inversion. The B-values and density deviations are given for the optimum result (No.1), and further examples of plausible results at calculation numbers 500 and 1000.

**Figure Captions**

Fig. 1. Global signatures of the Yellowstone hotspot. (a) Global free-air gravity anomaly of some notable hotspots including Hawaii, Iceland, and Yellowstone in Mgal. These anomalies have wavelengths the order of 1000 km long and relative amplitudes of +20 to +40 Mgal; and (b) North America geoid map showing the Yellowstone -7 geoid anomaly. Yellowstone has a ~1000 km wide topographic swell.

Fig. 2. Track of the Yellowstone hotspot (Y) showing the relative motion of age-transgressive SRP silicic volcanic centers at 180° to the direction of the direction North American plate motion. The topographically low area occupied by the Snake River Plain is outlined in green. Centers of post-17 Ma silicic volcanism (in yellow) contain multiple caldera-forming eruptions. Red dots are historic earthquake epicenters, taken from compilations of the University of Utah and the USGS of M1.5 – 7.5 earthquakes. Late Quaternary faults are shown by black lines; Cenozoic basaltic dikes (age in Ma) are shown in yellow and orange; $^{87}Sr/^{86}Sr$ isotope boundary for the 0.706 value is shown as a black-dashed line; and the YSRP tectonic parabola is defined by the bow-shaped pattern of high topography and seismicity surrounding the YSRP (yellow dashed lines). The relative motion vector of the North American Plate over the mantle at 2.2 cm/yr is noted as a large arrow. The Newberry-Oregon trend of silicic volcanism extends NW across southeast Oregon to the Newberry caldera (N).

Fig. 3. Space view of Grand Teton and Yellowstone National Parks from Landsat satellite images overlain on digital elevation data. The 2.4 km-high Yellowstone caldera was produced by a giant volcanic eruption 630 000 years ago. The caldera occupies a 60 by 40-km-wide area of central Yellowstone. The Teton fault bounds the east side of the Teton Range and raised the mountains high above Jackson Hole's valley floor. From Smith and Siegel (2000).

Fig. 4. Map of the seismic and GPS stations deployed for the 1999-2003 Yellowstone Hotspot Geodynamic project. The networks contain 166 seismic stations (broadband and short-period), 15 permanent GPS and 150 campaign GPS stations. Note the linear distribution of stations in 600 km long arrays with a NW azimuth designed to best record earthquakes at teleseismic distances (>1000 km) from the major seismic belts of the western Pacific and South America.

Fig. 5. Volcanic and tectonic features of Yellowstone and surrounding area. Yellowstone calderas I (2.1 Ma), II (1.2 Ma) and III (0.64 Ma)are shown as black lines and labeled. The two resurgent domes Mallard Lake (ML) and Sour Creek (SC) are shown with dashed black lines. Yellow stars mark post-caldera volcanic vents of 640 000 to 70 000 years in age. Late Quaternary faults are heavy black lines with ticks on downthrown side. Fault abbreviations are EGF=eastern Gallatin fault, HLF=Hebgen Lake fault, MF=Madison fault, CF=Centennial fault, TF=Teton fault, MSF=Mount Sheridan fault, YLF=Yellowstone Lake fault, BFF=Buffalo Fork fault, UYF=Upper Yellowstone Valley fault. Areas of hydrothermal features, including geysers, fumaroles, and hotsprings, are shown in orange.

Fig. 6. (a) Heatflow of the Yellowstone and the Snake River Plain, with heatflow of the SRP averaging ~ 150 $mWm^{-2}$; (b) Yellowstone Plateau averaged heat flow ~2000 $mWm^{-2}$; and (c) very high heatflow of Yellowstone Lake ranges from ~100 $mWm^{-2}$ to extraordinarily high 30 000 $mWm^{-2}$ (after Blackwell and Richards, 2006).

Fig. 7. Photographs of prominent hydrothermal features of Yellowstone. (a) Aerial view of a rare eruption of Steamboat Geyser in Norris Geyser Basin, July 6, 1984. It the largest geyser in the world, sending water up to 250 m high. Steamboat Geyser erupts sporadically at decadal scales but has erupted 7 times in 2006-2007. (b) The Hot Springs Basin group of fumaroles and hot springs is the largest hydrothermal area of Yellowstone and is located 15 km north of the caldera boundary, between the Sour Creek dome and the Mirror Plateau. Pictures by Robert B. Smith.

Fig. 8. Station map of Yellowstone National Park and surrounding area showing seismograph, GPS, and borehole strainmeter networks. Seismic stations consist of broadband and short-period seismometers operated by the University of Utah. GPS sites include 26 permanent and 90 temporarily occupied (campaign) sites operated by the University of Utah and EarthScope PBO. Borehole strainmeter sites also contain downhole seismometers and are operated by the EarthScope PBO project. All data from these instruments are available in real-time and online.

Fig. 9. Seismicity of the Yellowstone Plateau (1975-2007). Epicenters are located by employing a three-dimensional P-wave velocity model of Husen and Smith (2004). Locations of the M7.5 1959 Hebgen Lake Mt and M6.1 Norris Jct are highlighted as a large red star and large circle, respectively.

Fig. 10. Photographs of active faults of the Yellowstone Plateau: (a) the Hebgen Lake fault broke vertically during the M7.5 Hebgen Lake, MT, earthquake with as much as 5.7 m of vertical offset; and (b) caldera-boundary faults on the Mirror Plateau, northeast Yellowstone, with a maximum offset of ~30 on the left, SW-facing fault. Note three antithetic NW-facing faults to right, creating a graben occupied by Mirror Lake. Pictures by Robert B. Smith.

Fig. 11. Maximum focal depths of the Hebgen Lake-Yellowstone area serve as a proxy for conductive temperature: (a) well-located hypocenters (red dots) along 10-km wide windows corresponding to profiles in map view (b). The 80$^{th}$ percentile maximum focal depth is marked by the dashed line. This depth is interpreted as the brittle-ductile transition at ~400°C. (b) Contoured map of focal depths showing the very shallow focal depths in the caldera produced by high temperatures. The thin seismogenic layer of the caldera, ~5 km thick, restricts the maximum earthquake magnitude to Mw 6.5.

Fig. 12. Isosurfaces of anomalously low P-wave bodies are determined from local earthquake tomography of the Yellowstone caldera and reveal the Yellowstone magma chamber. The shallow anomaly plotted in blue is interpreted to be a gas-saturated body. The red anomaly is interpreted to be 5% to 15% partial melt corresponding to a crystallizing magma body that feeds the surface silicic and basaltic magmatism of Yellowstone (from Husen and Smith, 2004).

Fig. 13. Crustal deformation of the Yellowstone Plateau deformation from leveling and GPS observations (after Pelton and Smith, 1982; Puskas et al., 2007a; Vasco et al., 2007). Color backgrounds represent vertical motion measured from (a) leveling surveys between 1923 and 1987 and (b)-(d) GPS campaigns between 1987 and 2003. Red circles represent campaign GPS

sites, yellow circles represent permanent GPS stations, and arrows are the direction of motion. Time windows correspond to the distinct periods of caldera uplift and subsidence.

Fig. 14. Stress field of Yellowstone and the Snake River Plain illustrating dominant lithospheric NE-SW extension: (a) directions of stress in the YSRP from focal mechanism T axes, minimum horizontal principals stresses ($\sigma_3$), slip directions of normal faults ($\phi$), post-caldera volcanic vent alignments, and GPS- derived strain tensors; and b) similar stress directions of the Yellowstone Plateau (Waite and Smith, 2004).

Fig. 15. Temporal history of deformation and earthquakes of Yellowstone. Earthquakes are sorted by date into quarters to obtain the total number of earthquakes per three-month period. Specific leveling and GPS surveys are shown as black squares and white circles, respectively. Dates when InSAR images were taken are shown as gray diamonds. Deformation rates are averaged for periods of homogeneous deformation, either uplift or subsidence (from Chang et al., 2007).

Fig. 16. Unprecedented uplift of the Yellowstone caldera revealed by GPS and InSAR data (2004-2007) modified from Chang et al. (2007). (a) Map view of the uplift with GPS vertical and horizontal vectors and background showing line of sight (nearly vertical) deformation in 28 mm displacement bands. Note the maximum 7 cm/yr of uplift of the caldera compared to up to 1.5 cm/yr of subsidence of the Norris Geyser basin area. (b) Cross section of modeled 10° SE-dipping sill that is interpreted to be inflating at 0.1 $km^3$ per year, consistent with the modeled rate of inflation from the heatflow and geochemical data. Color contours are Coulomb stress increase (red) or decrease (blue) caused by inflation of the sill. Hypocenters of earthquakes that occurred during the period of accelerated uplift are shown as black dots.

Fig. 17. P-wave velocity slices (km/s) from tomographic inversion of teleseismic data for the Yellowstone hotspot (after Jordan et al., 2005; Waite et al., 2006). Data consisted of P-wave arrivals of 115 earthquakes recorded at 86 stations with 3399 P and 380 PKIPK arrivals. Maps are horizontal slices of P-wave velocity at selected depths with corresponding relative decrease (red) and increase (blue) velocities. Note the low-velocity anomaly beneath Yellowstone is displaced to the west as depth increases. A high-velocity zone is located to the east of Yellowstone. Profile lines for Fig. 18 are shown in the 30 km and 330 km depth slices.

Fig. 18. Two-dimensional cross sections of the Yellowstone P-wave low velocity anomalies corresponding to Fig. 17 (Jordan et al., 2005). (a) NW-SE cross-section across western Montana and western Wyoming, and b) NE-SW profile along the YSRP. Significantly these profiles reveal a 60° west-dipping low-velocity anomaly of up to -1.5%. The anomaly extends to 660 km in the NW-SE profile, but does not extend deeper than 200 km beneath Yellowstone in the NE-SW profile.

Fig. 19. Seismic image of the Yellowstone plume as a 60° west-dipping, rising column of molten rock of up to -1.5% melt originating in the mantle transition zone. The plume is represented by a three-dimensional P-wave velocity isosurface of the ~-1% value. The top of this upper mantle plume underlies Yellowstone to depths of ~250 km, but the deeper part to the northwest is at a depth of ~650 km, at the bottom of the mantle transition zone. (Also see 3D

animation of the University of Utah Yellowstone hotspot project results: earthquakes, geysers, faults, GPS sites, volcanoes, calderas, topography and other geo-located geologic features of the Yellowstone-Teton region http://siovizcenter.ucsd.edu/library/objects/detail.php?ID=210. The iView viewer is free and can be downloaded from: http://www.ivs3d.com/download/iview3d_download.html )

Fig. 20. One-dimensional geodynamic model of the Yellowstone plume plotted in two dimensions for realism. Effect of two-dimensional extrapolation is negligible for the low relative velocities. Model of excess temperature (°K) is constrained by seismic P-wave velocity and relative attenuation of P-waves ($Q_p$) in $Q^{-1}$, for wet and dry models of Cammarano et al. (2003, 2007). $Q^{-1}$ is the relative attenuation of seismic waves for P- and S-waves modified for Yellowstone by Clawson et al., (1989) and converted to $Q_s$ by standard methods.

Fig. 21. Computed regional mantle density structure and flow beneath North America and the northeastern Pacific for tomography model mean (mean shear wave) with viscosity structure VM1 from Fig. 22. (a) Mantle cross-section showing density structure along the line shown in the bottom panel. The relatively dense subducted Farallon plate is located beneath the eastern U.S. at depths of 1000 to 1900 km. (b) Map view of upper mantle flow at 359 km depth. Vectors represent horizontal components of flow and color background represents vertical flow.

Fig. 22. Computed horizontal upper mantle flow in the vicinity of the Yellowstone hotspot at various depths. Viscosity models VM1 and VM2, used as the basis of the mantle flow models, are shown in the upper right panel. Model VM1 constrains the tomography model of Fig. 21. Bottom left panel also includes fixed-hotspot tracks (0-15 Ma) for four different models of North American "absolute" plate motion.

Fig. 23. Models of hotspot plume conduits for (a) plumes ascending from the mantle transition zone (660 km), and (b) initially vertical plumes ascending from the core-mantle boundary. The upper panels in (a) and (b) show the surface hotspot tracks and the progression of surface volcanism over time (0-15 Ma) from Steinberger et al. (2004). Gray shaded areas represent provinces of basaltic volcanism in the Columbia Plateau and eastern Snake River Plain. The lower panels show the projection of the plume conduits into map view and plume displacement with depth. Colored lines represent plume conduit models corresponding to mantle flow models from Fig. 22.

Fig. 24. Cross-section of western North America mantle S-wave velocity structure from mantle tomography (Grand, 1997). Mantle flow directions represented by vectors. Yellowstone mantle plume is superimposed as thick orange line, with hypothesized lower mantle extension shown as a dashed line.

Fig. 25. (a) Geoid map of Western U.S. from GEOID2003 model with profile line AA', (b) parameterized Yellowstone plume model, and (c) forward models of the geoid based on plume parameterizations (blue lines) compared to the filtered geoid (red lines) in the area of the Yellowstone hotspot swell. Geoid data were shifted relative to background geoid values so that modeled heights ranged from +7 to +30 m. The black line represents the unfiltered geoid and the white lines are selected models discussed in Section 8. The plume in panel (b) was initially

parameterized into nine sections, but only the uppermost four segments contributed to the solution. Density perturbations and P-wave velocities for the best-fit model are included in the plot.

Fig. 26. (a) Velocity field based on kinematic modeling, and (b) total stress field of western U.S. from dynamic modeling of the lithosphere. The velocity field is interpolated from GPS velocities and fault-slip rates. The stress field is calculated from a detailed lithosphere density structure model that includes the YSRP. Boundary stresses are constrained to match the strain tensors from kinematic modeling.

Fig. 27. Comparison of buoyancy flux estimates for oceanic and continental hotspots plotted as a function of plume radii and excess temperature. White circles approximate the uncertainty. Radius and excess temperature estimates of Eifel (E), Massif Central (MC), and Yellowstone (Y) from tomographic images are used to estimate the buoyancy flux using the method of Ritter (2004). The buoyancy fluxes for Iceland (I) and Hawaii (H) is taken from Sleep (1990). The buoyancy flux is calculated for a potential mantle temperature of 1300º C. If the mantle beneath Yellowstone were 200º C hotter, then it would yield a buoyancy flux 10 times larger.

Fig. 28. Schematic diagram of the Yellowstone plume progression. (a) Behind-arc plume-head phase located beneath the accreted oceanic plate of the Columbia Plateau and behind the descending Juan de Fuca plate, and (b) sheared and tilted plume head entrained in mantle flow. Note the depleted upper-mantle residuum body above the plume interacting with a continental lithosphere.

Fig. 29. Track of the Yellowstone plume tail originating at ~650 km depth and 150 km west of Yellowstone. At its origin at 15 Ma, the plume had a vertical ascending path beneath the Columbia Plateau to the west of the Sr 0.706 boundary and coincident with the implied outline of the plume head by Camp (2004). The plume was tilted 60º to the SE by mantle flow, so that the plume base (red circles) was offset from surface silicic volcanic centers (yellow circles). Ages of silicic and basaltic volcanic centers are also shown on the map. The initial plume head spread out beneath the thin oceanic lithosphere to the west of the Sr 0.706, and the extend of spreading at 15 Ma and present day is shown by shaded areas.

**Supplementary figures**

Fig. S1 – Time series for station WLWY (White Lake, WY) in Yellowstone National Park.

Fig. S2 – Resolution test for a -1% reduction in the upper mantle.

Fig. S3 – Resolution test for a -3% reduction in the upper mantle.

Fig. S4 – Resolution test for a -1% reduction in the transition zone.

Fig. S5 – Resolution test for a -1% reduction in the sub transition zone.

Fig. S6 – The parameterization scheme of the optimized tomography.

**Figure 01**

**Click here to download high resolution image**

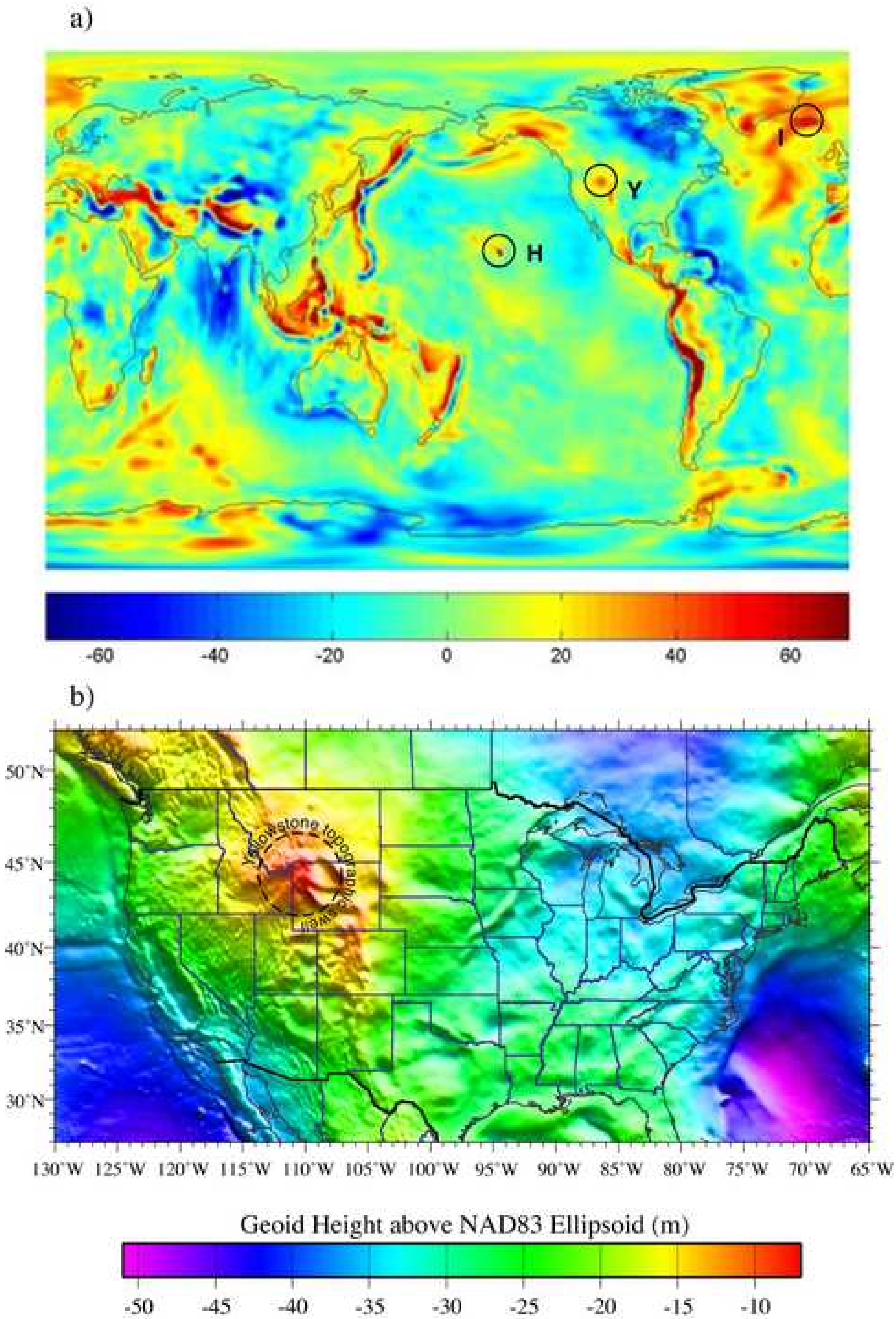

**Figure 02**

Click here to download high resolution image

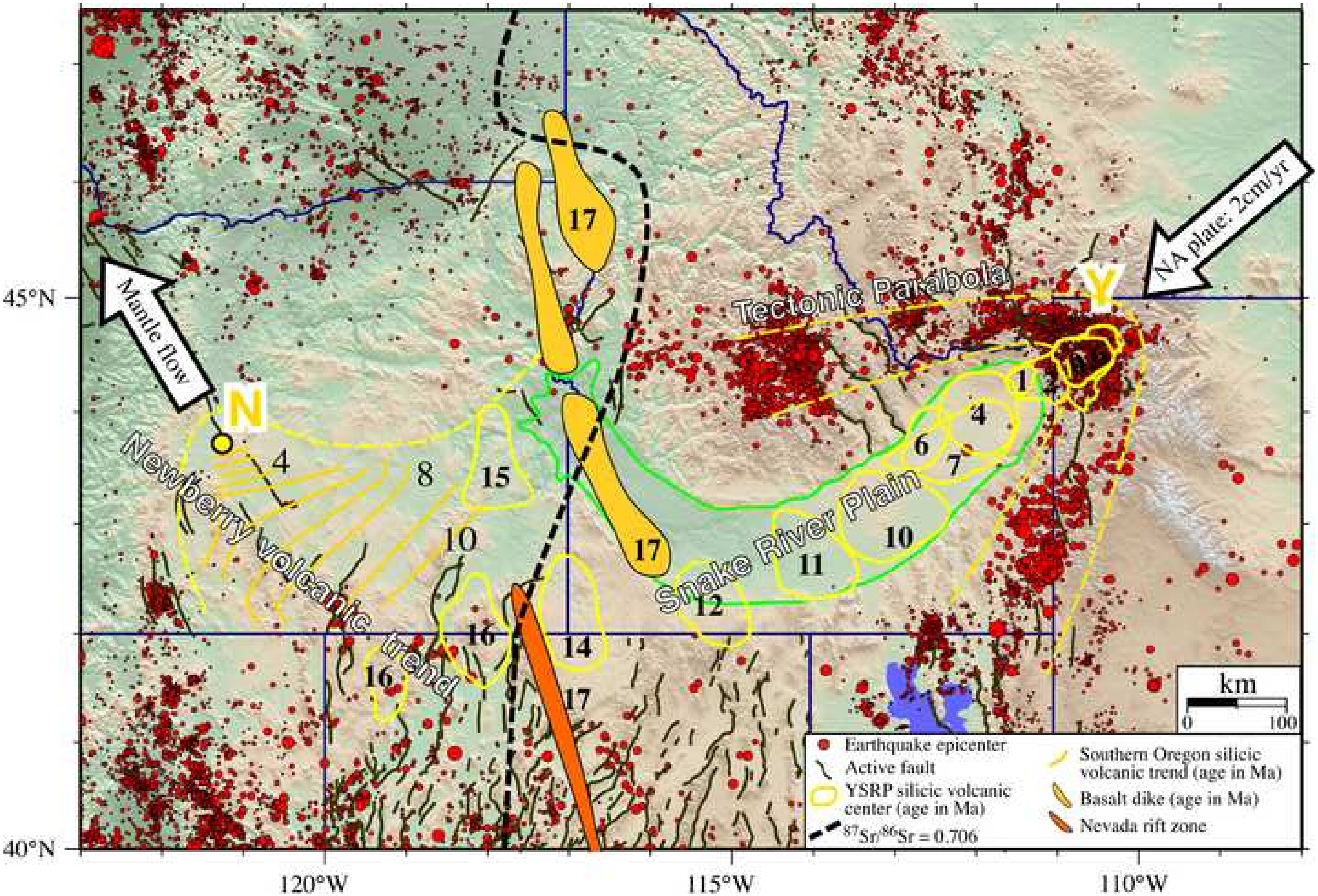

Figure 03

Click here to download high resolution image

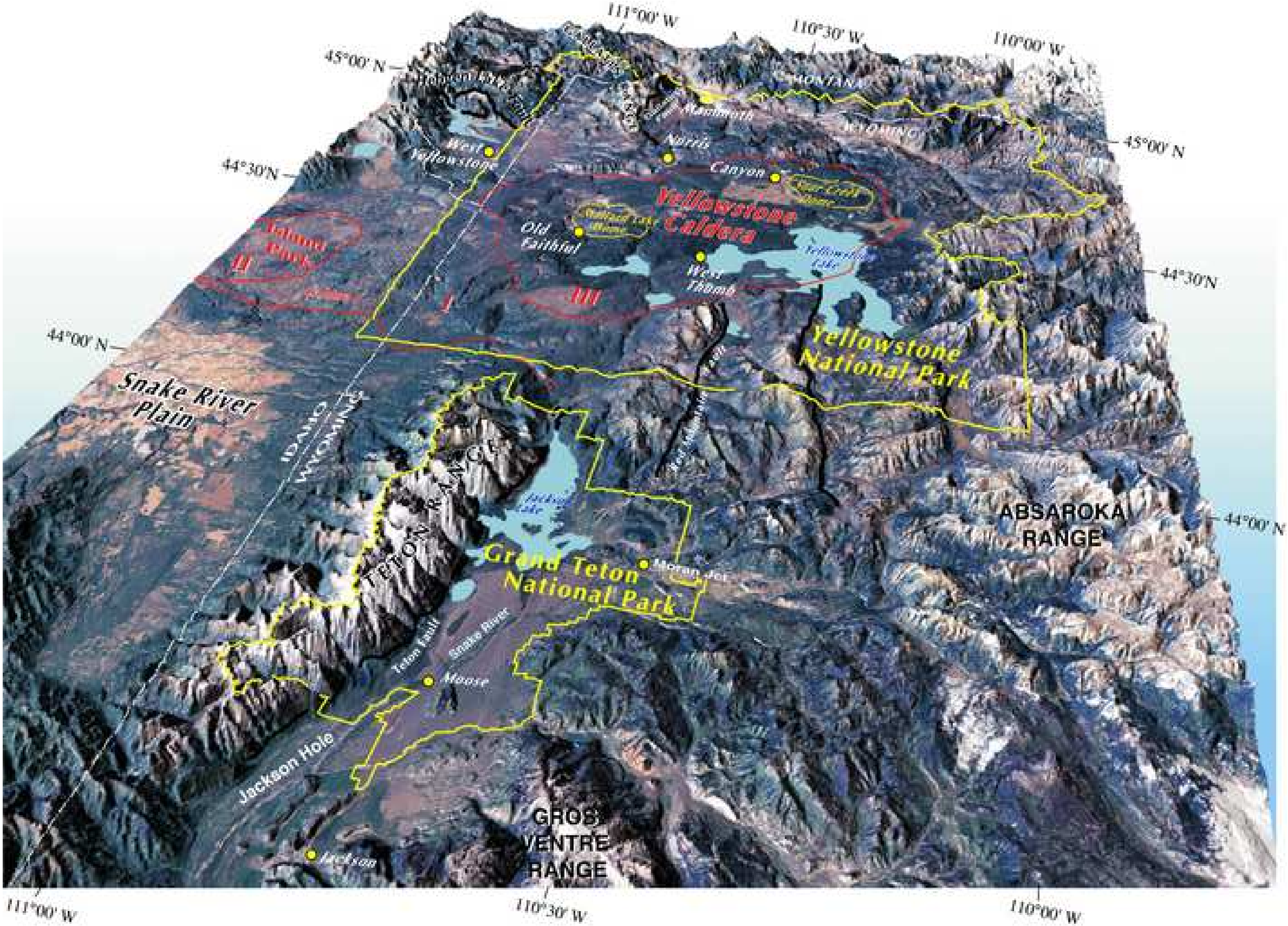

Figure 04

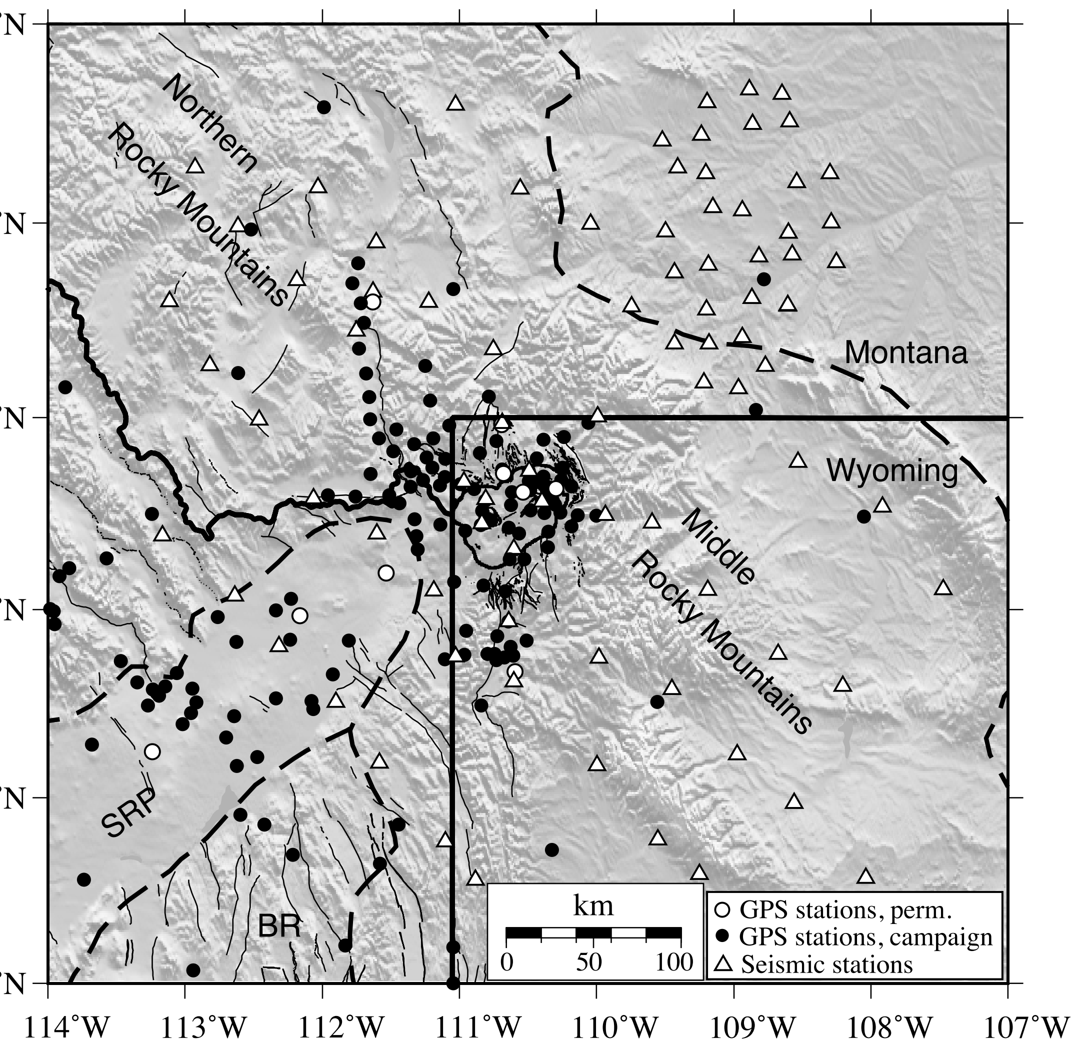

47°N
46°N
45°N
44°N
43°N
42°N
114°W
113°W
112°W
111°W
110°W
109°W
108°W
107°W
Northern
Rocky Mountains
Montana
Wyoming
Middle
Rocky Mountains
SRP
BR
km
0
50
100
GPS stations, perm.
GPS stations, campaign
Seismic stations

**Figure 05**
**Click here to download high resolution image**

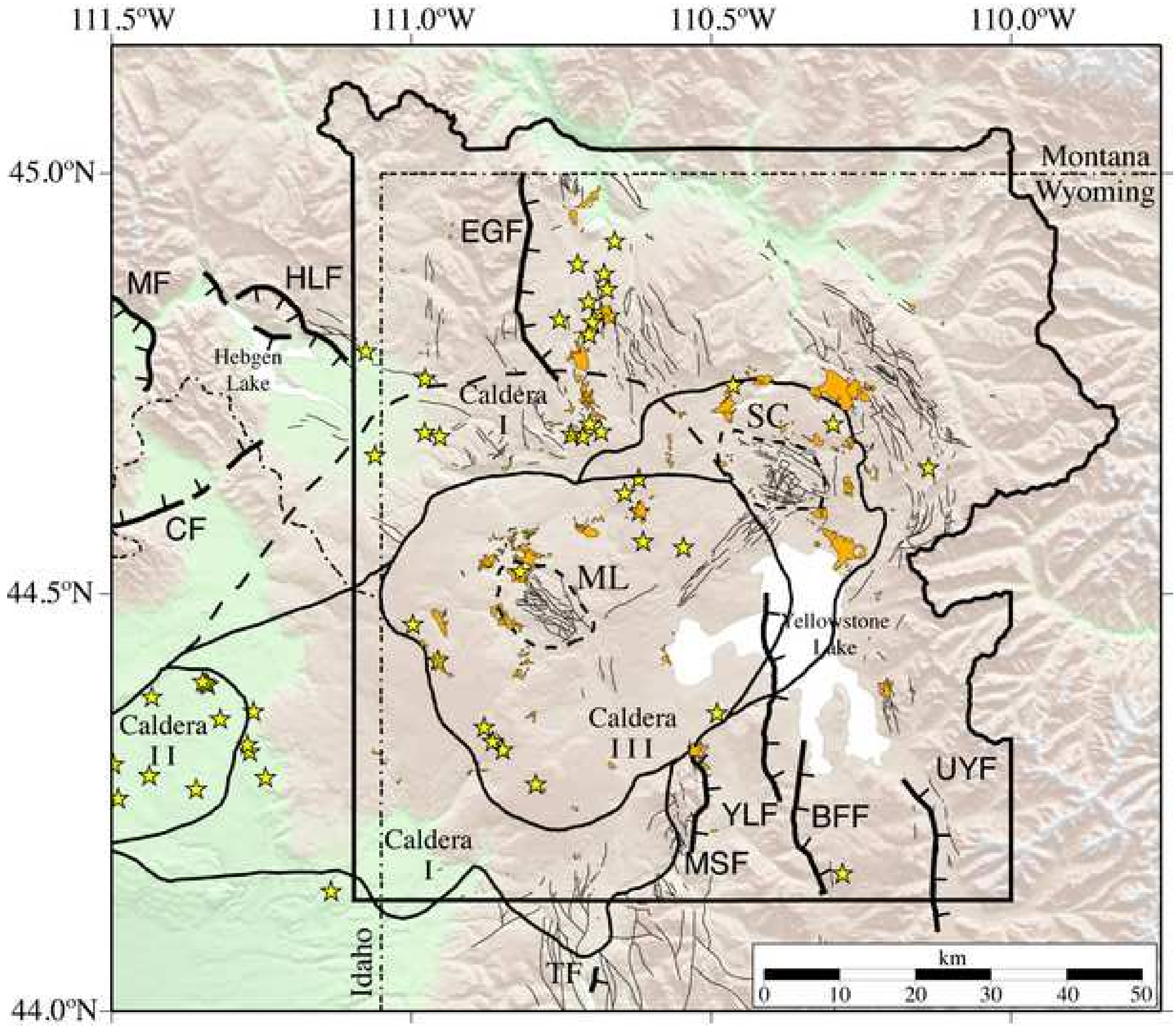

**Figure 06**

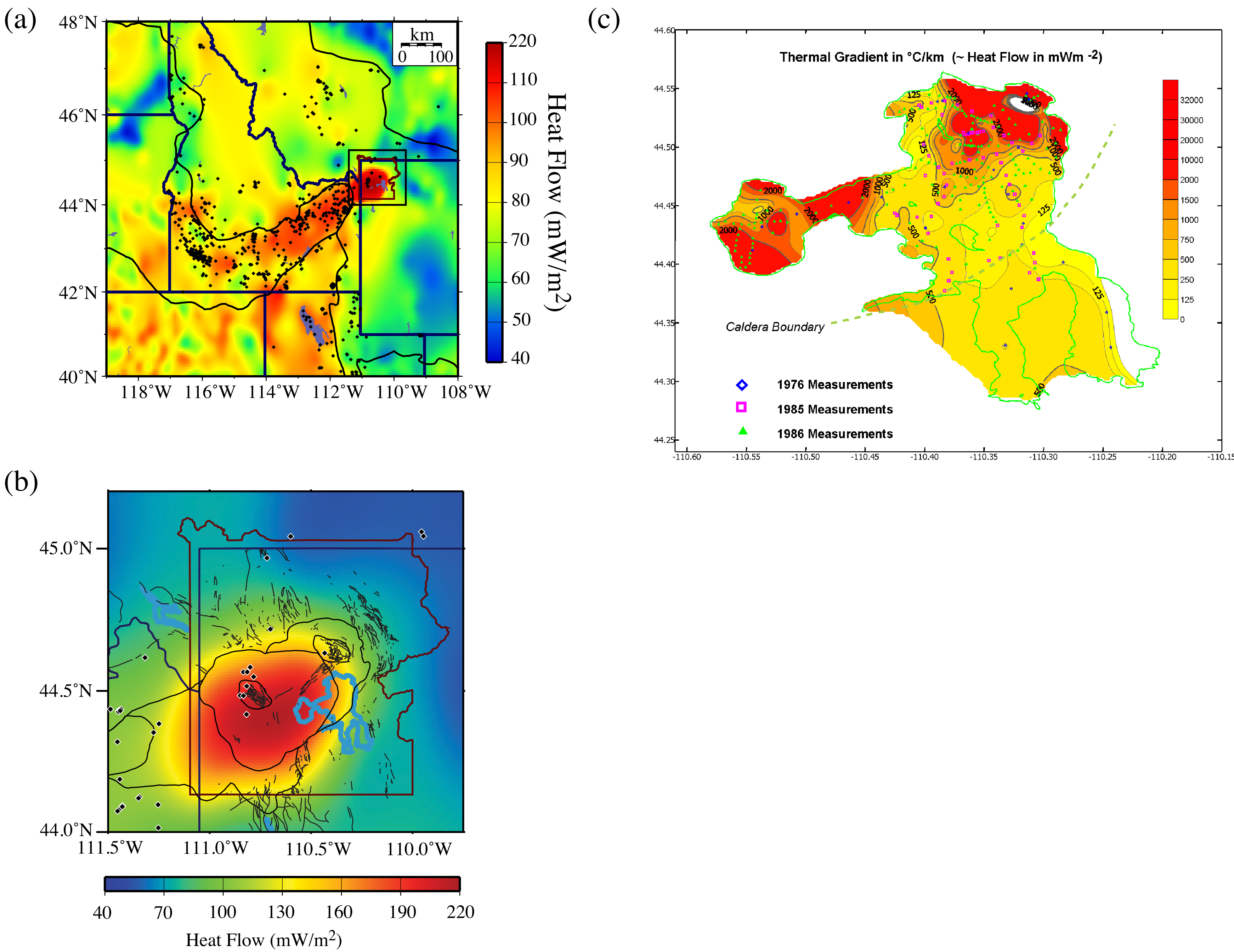

(a)
48°N
46°N
44°N
42°N
40°N
118°W
116°W
114°W
112°W
110°W
108°W
km
0
100
Heat Flow (mW/m$^2$)
220
110
100
90
80
70
60
50
40
(b)
45.0°N
44.5°N
44.0°N
111.5°W
111.0°W
110.5°W
110.0°W
40
70
100
130
160
190
220
Heat Flow (mW/m$^2$)
(c)
Thermal Gradient in °C/km (~ Heat Flow in mWm $^{-2}$)
32000
30000
20000
10000
2000
1500
1000
750
500
250
125
0
Caldera Boundary
1976 Measurements
1985 Measurements
1986 Measurements
44.60
44.55
44.50
44.45
44.40
44.35
44.30
44.25
-110.60
-110.55
-110.50
-110.45
-110.40
-110.35
-110.30
-110.25
-110.20
-110.15

Figure 07
Click here to download high resolution image

a)

b)

Figure 08
Click here to download high resolution image

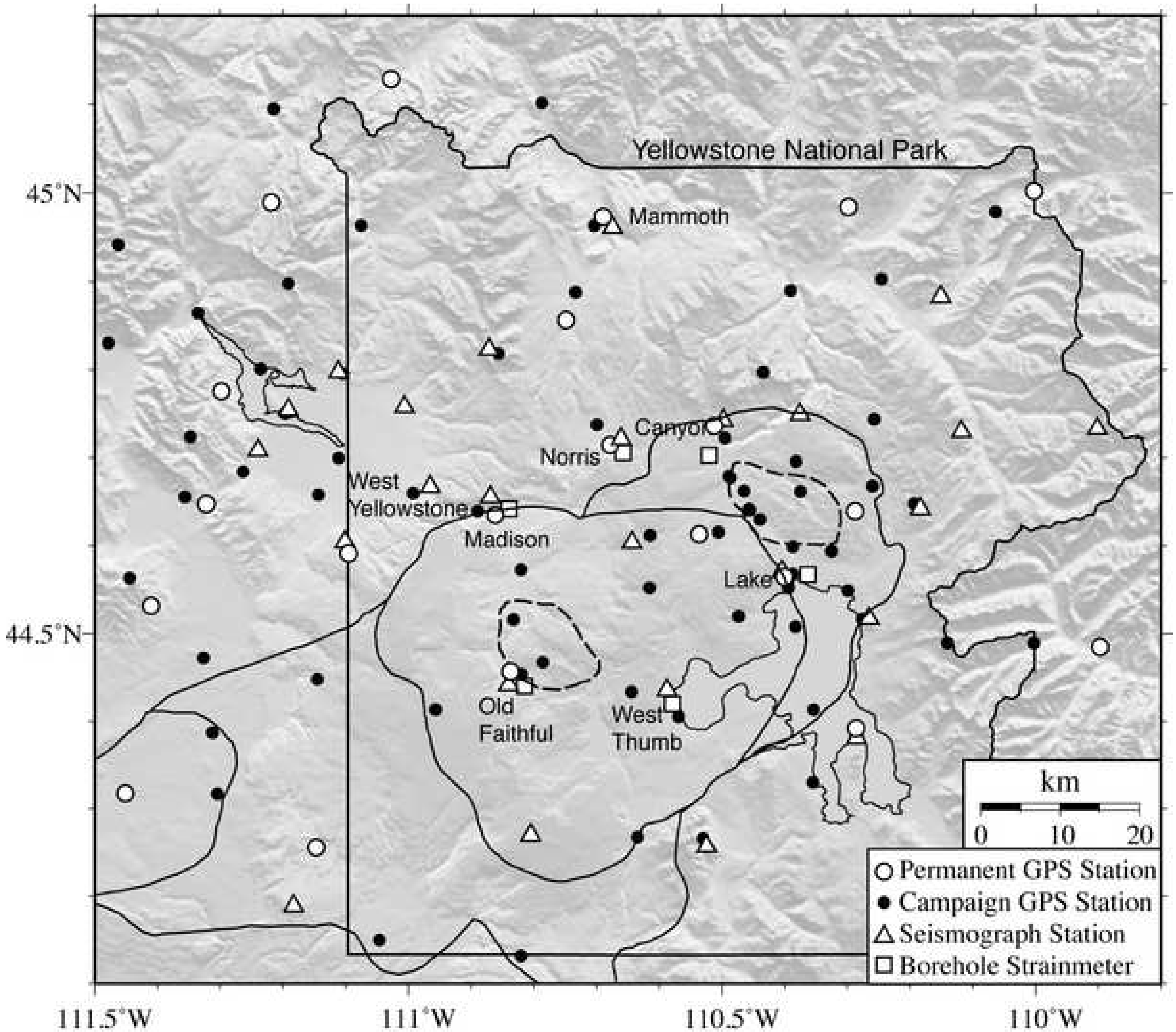

Figure 09
Click here to download high resolution image

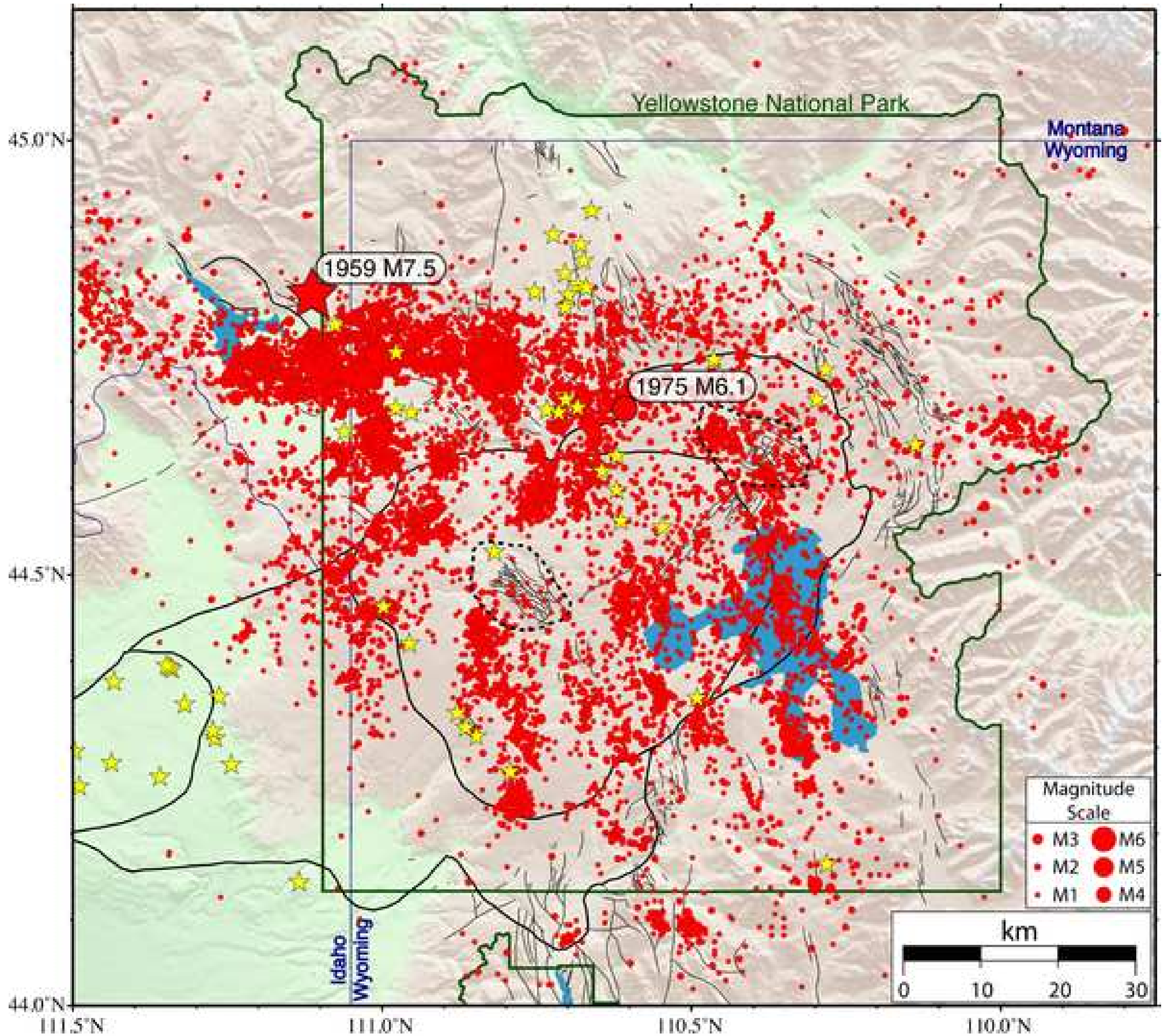

**Figure 10**
**Click here to download high resolution image**

a)

b)

Figure 11
Click here to download high resolution image

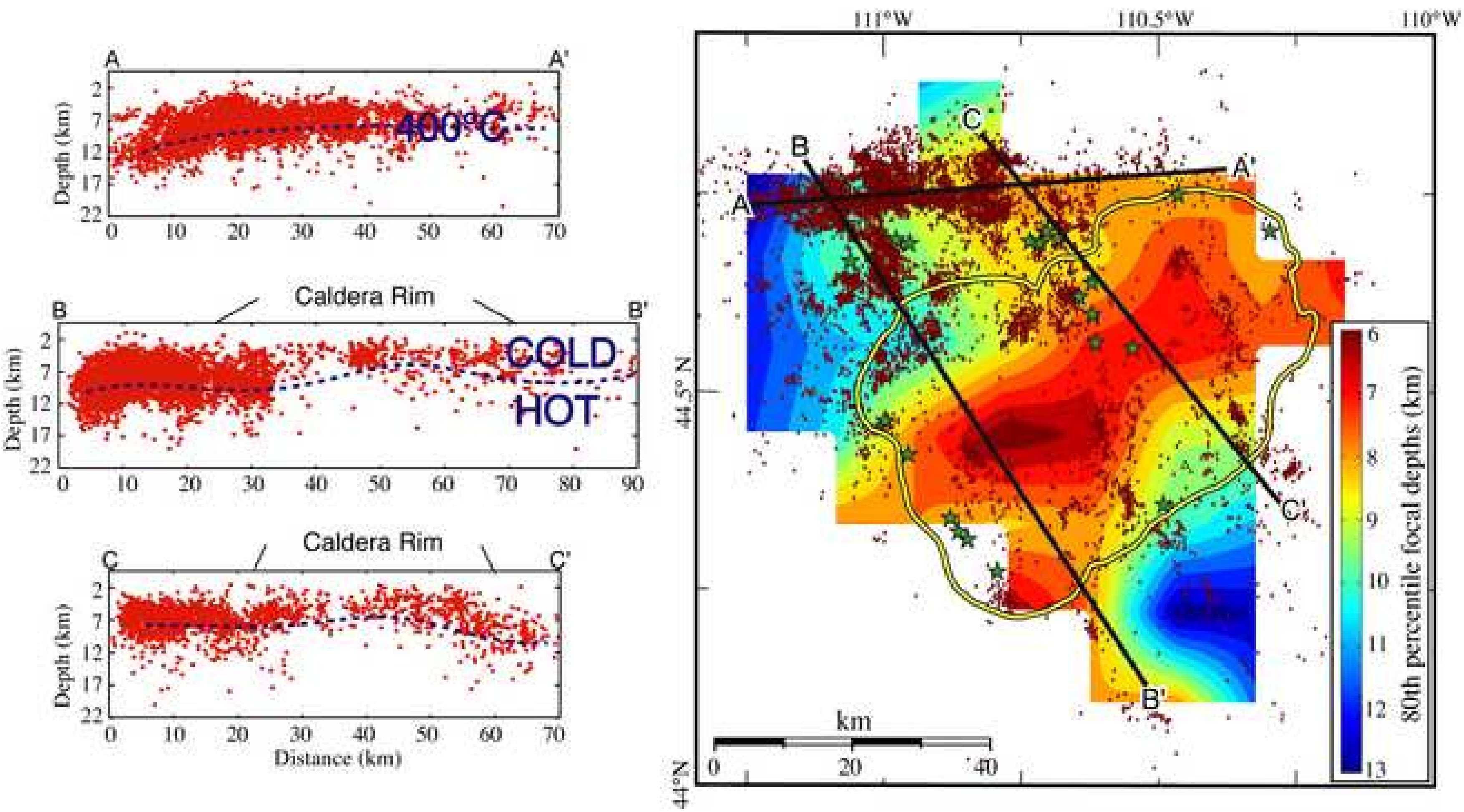

Figure 12

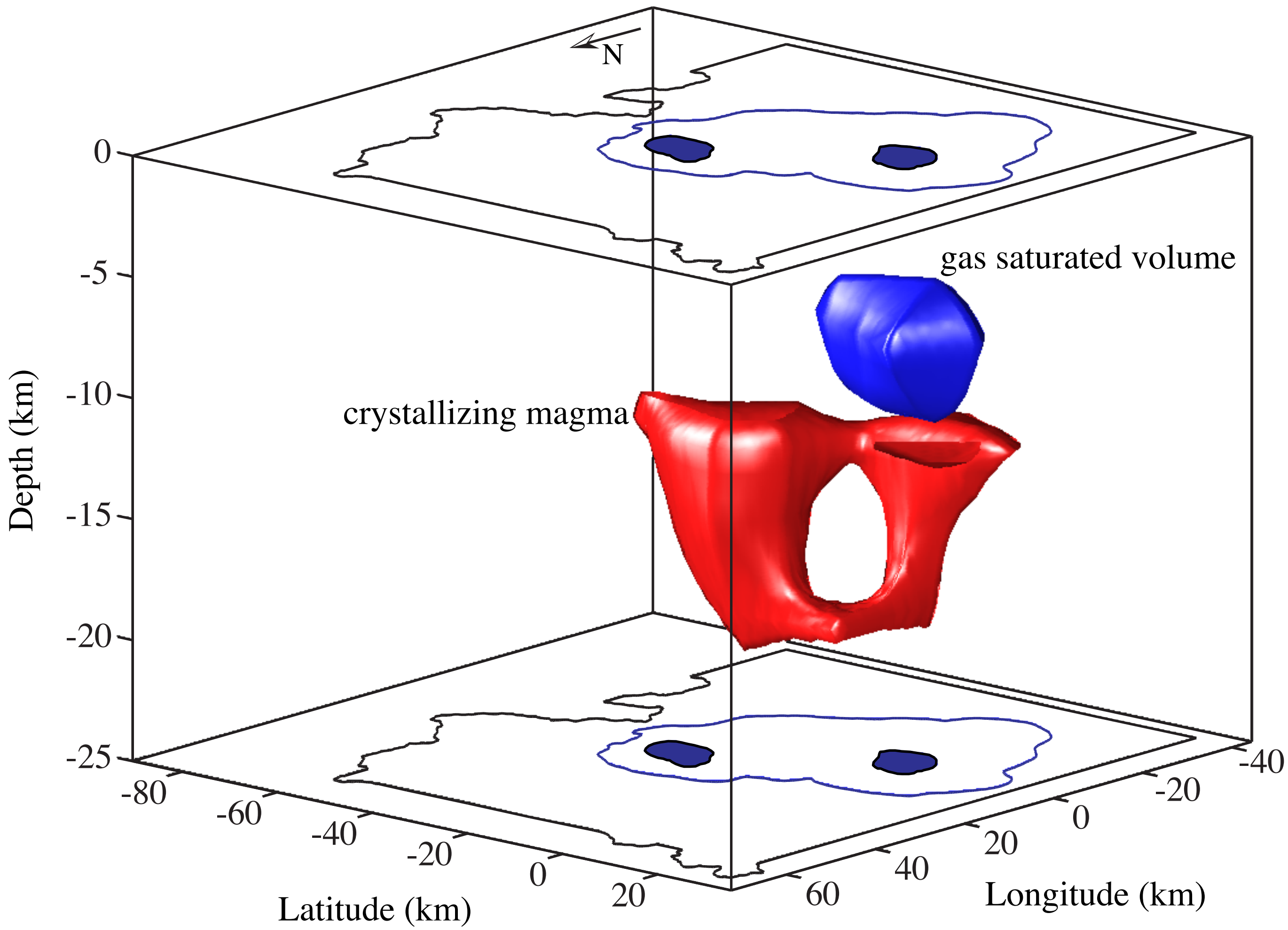
N
0
-5
-10
-15
-20
-25
Depth (km)
gas saturated volume
crystallizing magma
-80
-60
-40
-20
0
20
Latitude (km)
-40
-20
0
20
40
60
Longitude (km)

Figure 13

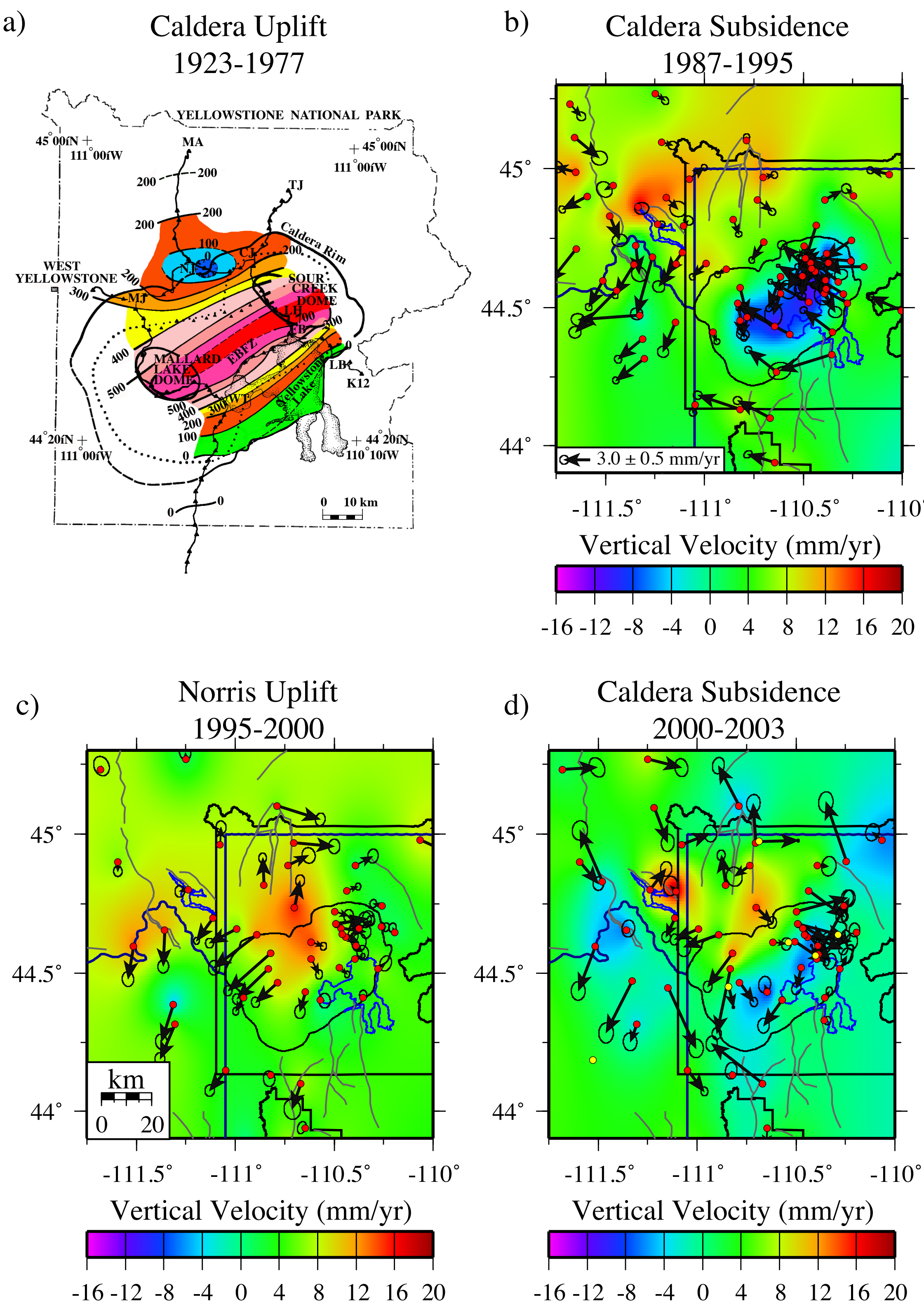
a)
Caldera Uplift
1923-1977
YELLOWSTONE NATIONAL PARK
WEST YELLOWSTONE
MALLARD LAKE DOME
SOUR CREEK DOME
Caldera Rim
Yellowstone Lake
EBFZ
MA
TJ
LB
K12
0 10 km
b)
Caldera Subsidence
1987-1995
3.0 ± 0.5 mm/yr
Vertical Velocity (mm/yr)
c)
Norris Uplift
1995-2000
km
0 20
Vertical Velocity (mm/yr)
d)
Caldera Subsidence
2000-2003
Vertical Velocity (mm/yr)
-111.5° -111° -110.5° -110°
45° 44.5° 44°
-16 -12 -8 -4 0 4 8 12 16 20

Figure 14

Click here to download high resolution image

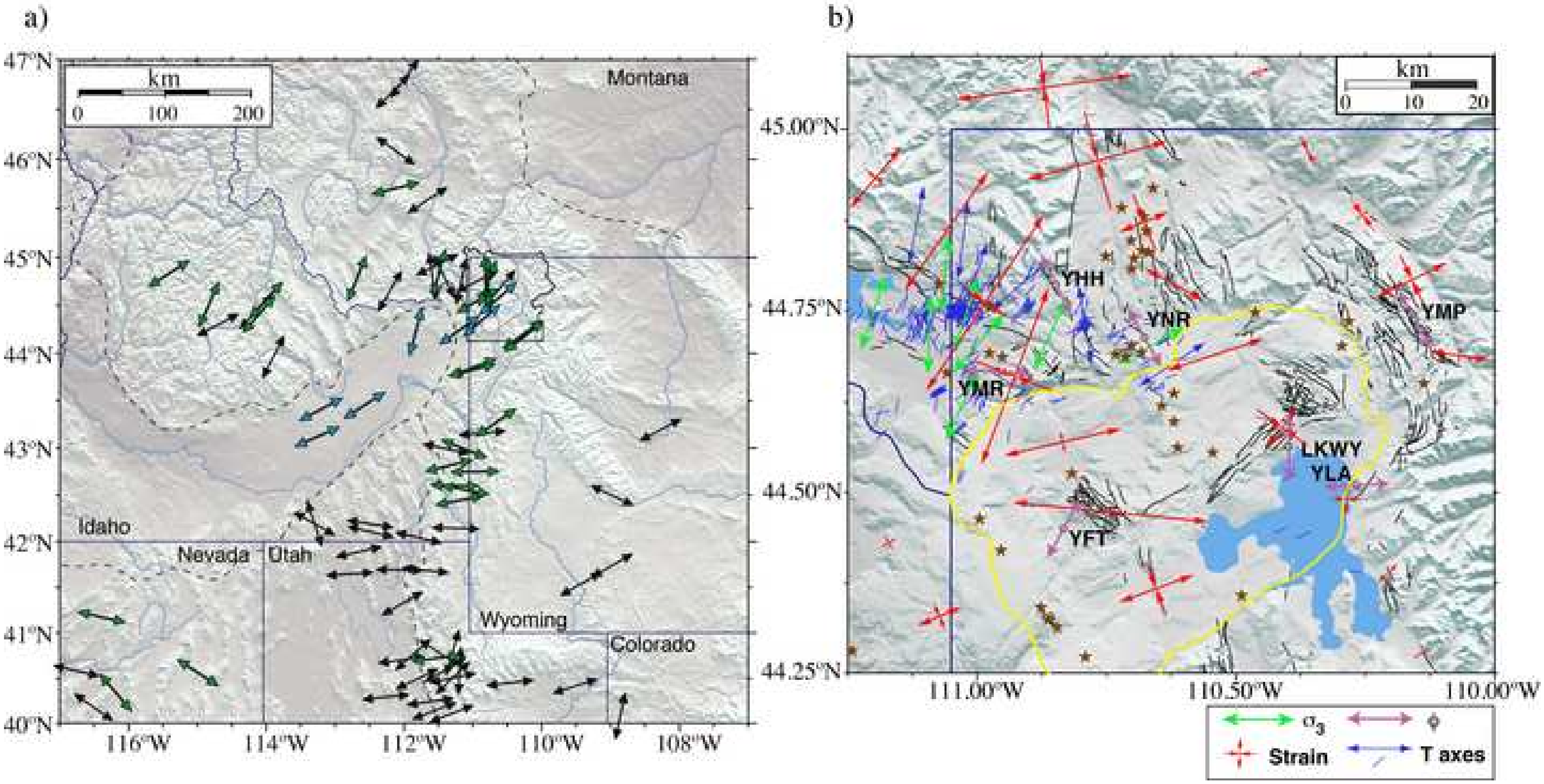

**Figure 15**

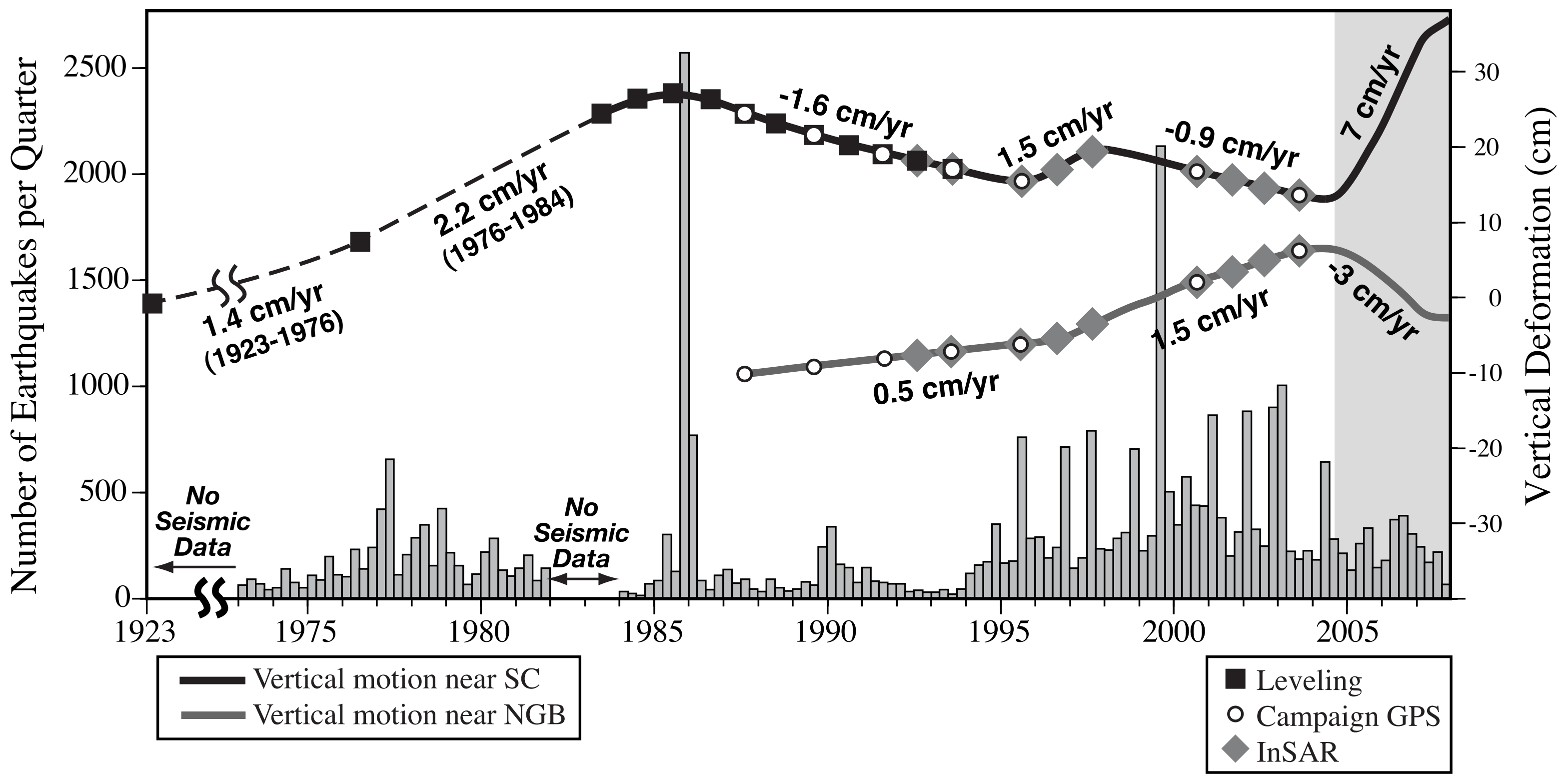

Number of Earthquakes per Quarter
Vertical Deformation (cm)
1.4 cm/yr
(1923-1976)
2.2 cm/yr
(1976-1984)
-1.6 cm/yr
1.5 cm/yr
-0.9 cm/yr
7 cm/yr
-3 cm/yr
1.5 cm/yr
0.5 cm/yr
No Seismic Data
No Seismic Data
1923
1975
1980
1985
1990
1995
2000
2005
Vertical motion near SC
Vertical motion near NGB
Leveling
Campaign GPS
InSAR

Figure 16

Click here to download high resolution image

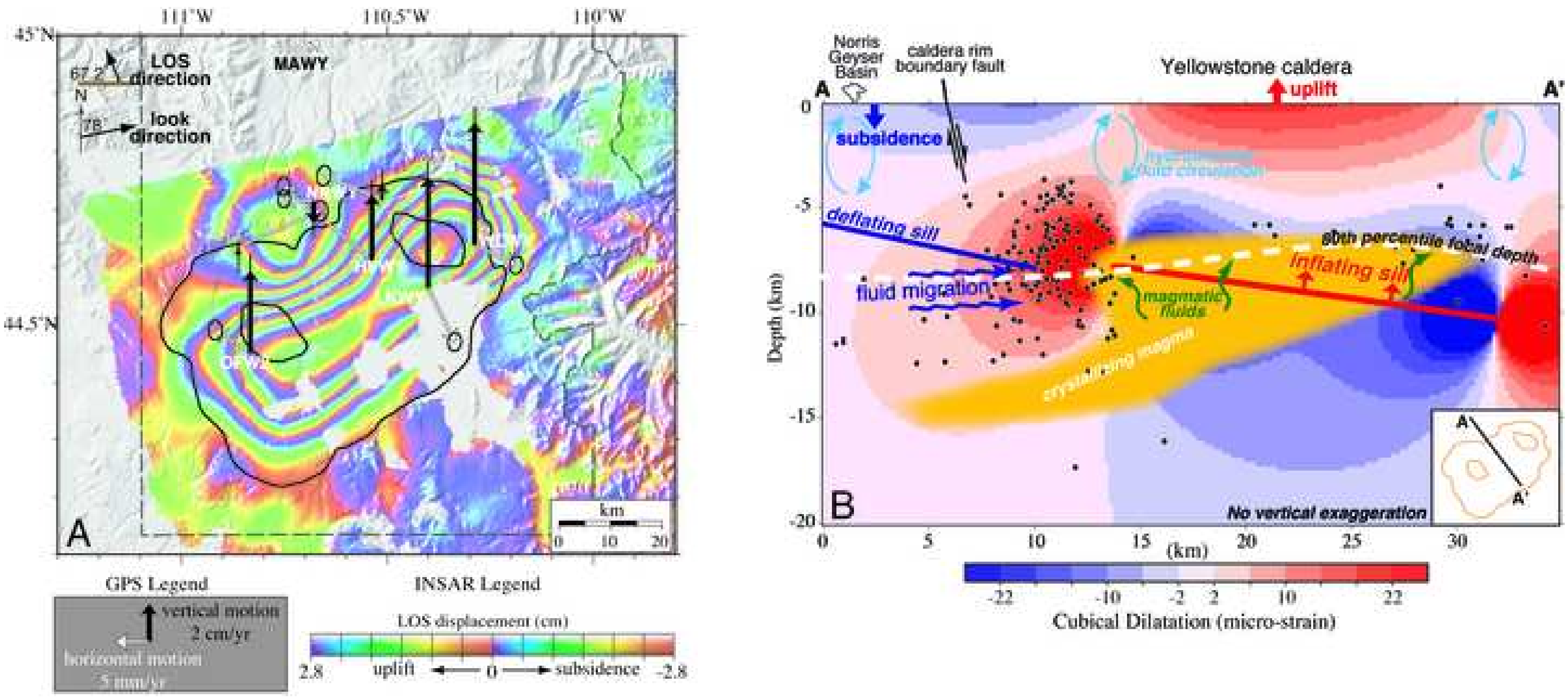

Figure 17

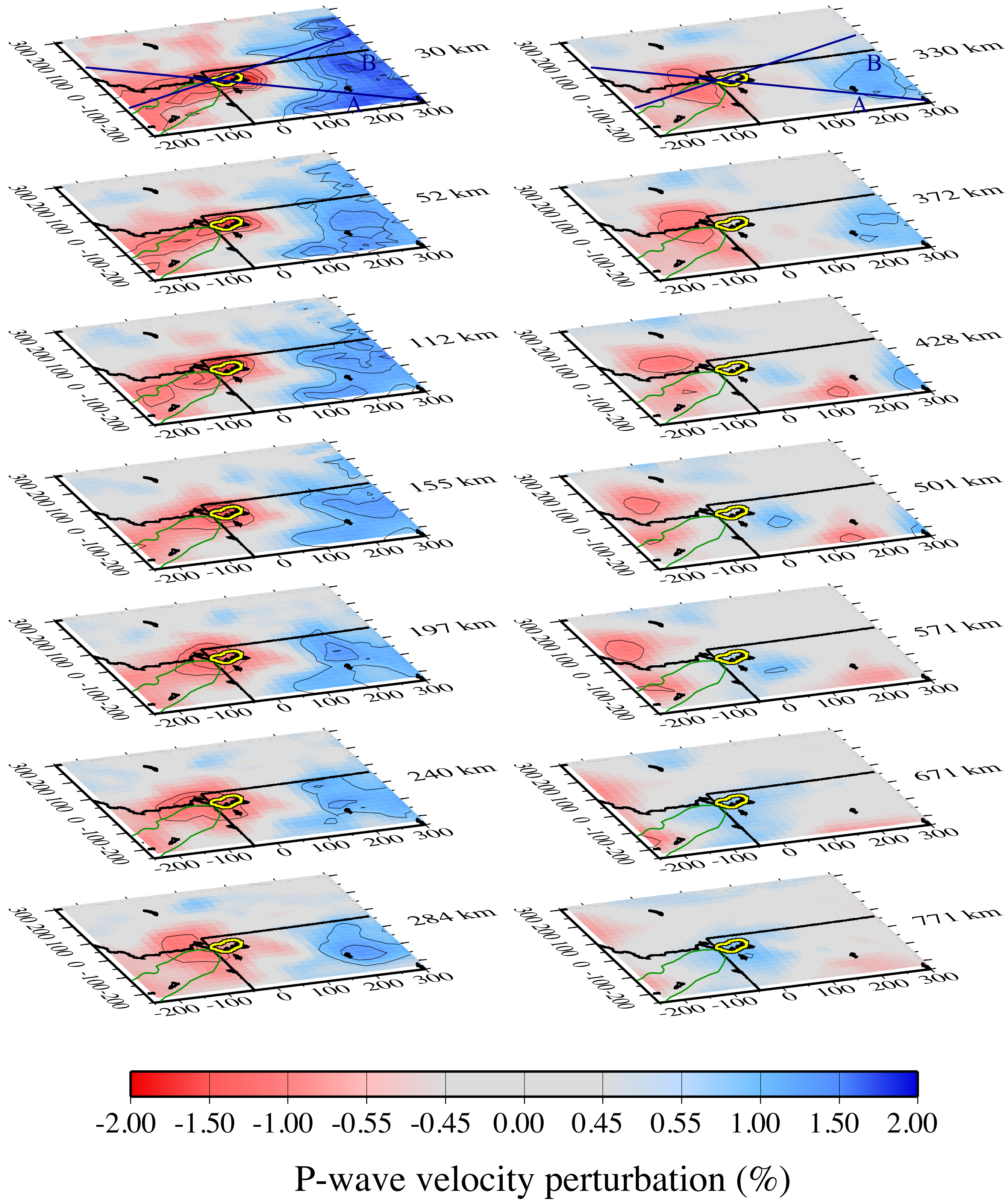
30 km
52 km
112 km
155 km
197 km
240 km
284 km
330 km
372 km
428 km
501 km
571 km
671 km
771 km
A
B
-2.00 -1.50 -1.00 -0.55 -0.45 0.00 0.45 0.55 1.00 1.50 2.00
P-wave velocity perturbation (%)

Figure 18

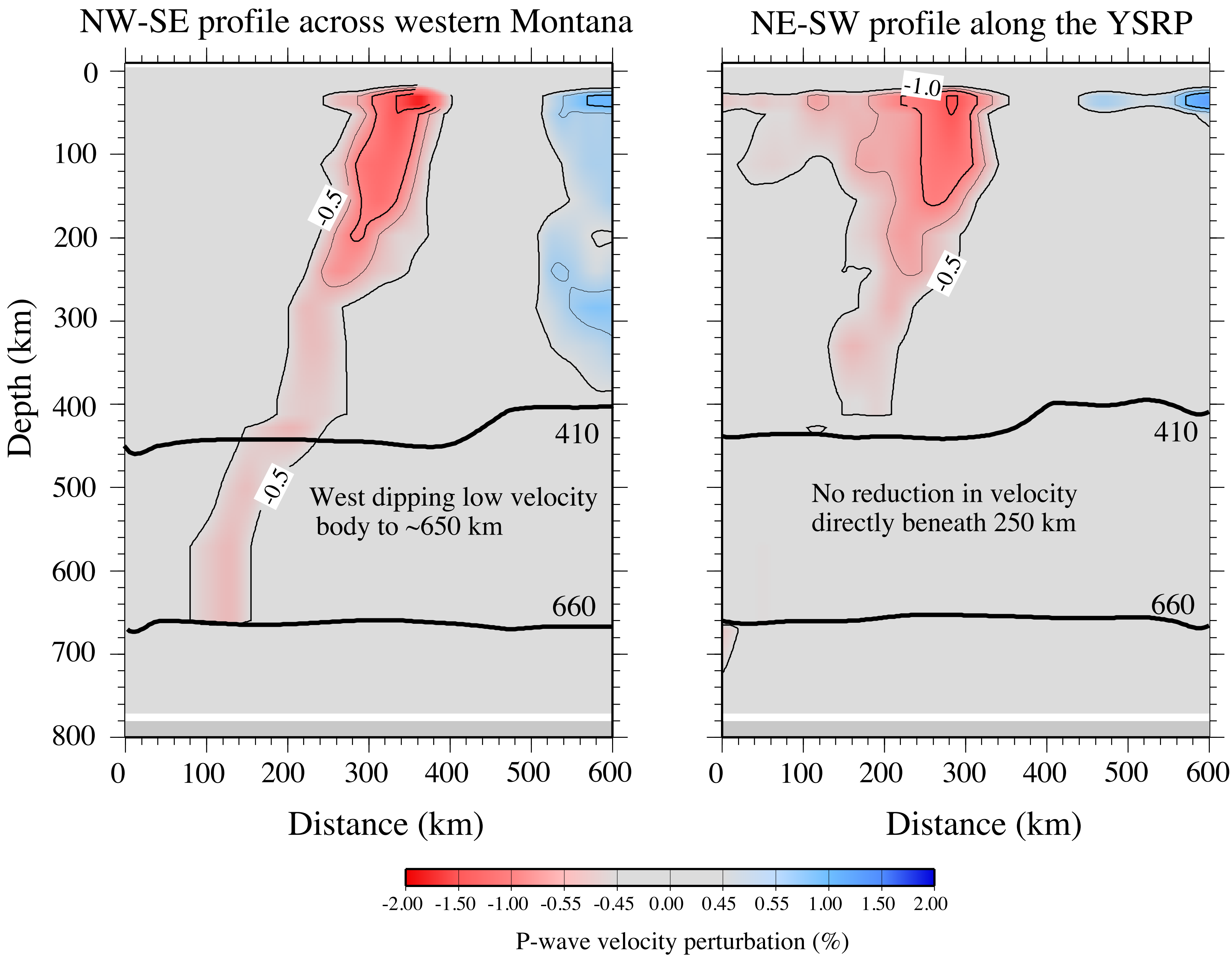
NW-SE profile across western Montana
NE-SW profile along the YSRP
Depth (km)
0
100
200
300
400
500
600
700
800
-0.5
-1.0
410
660
West dipping low velocity
body to ~650 km
No reduction in velocity
directly beneath 250 km
0
100
200
300
400
500
600
Distance (km)
-2.00
-1.50
-1.00
-0.55
-0.45
0.00
0.45
0.55
1.00
1.50
2.00
P-wave velocity perturbation (%)

Figure 19

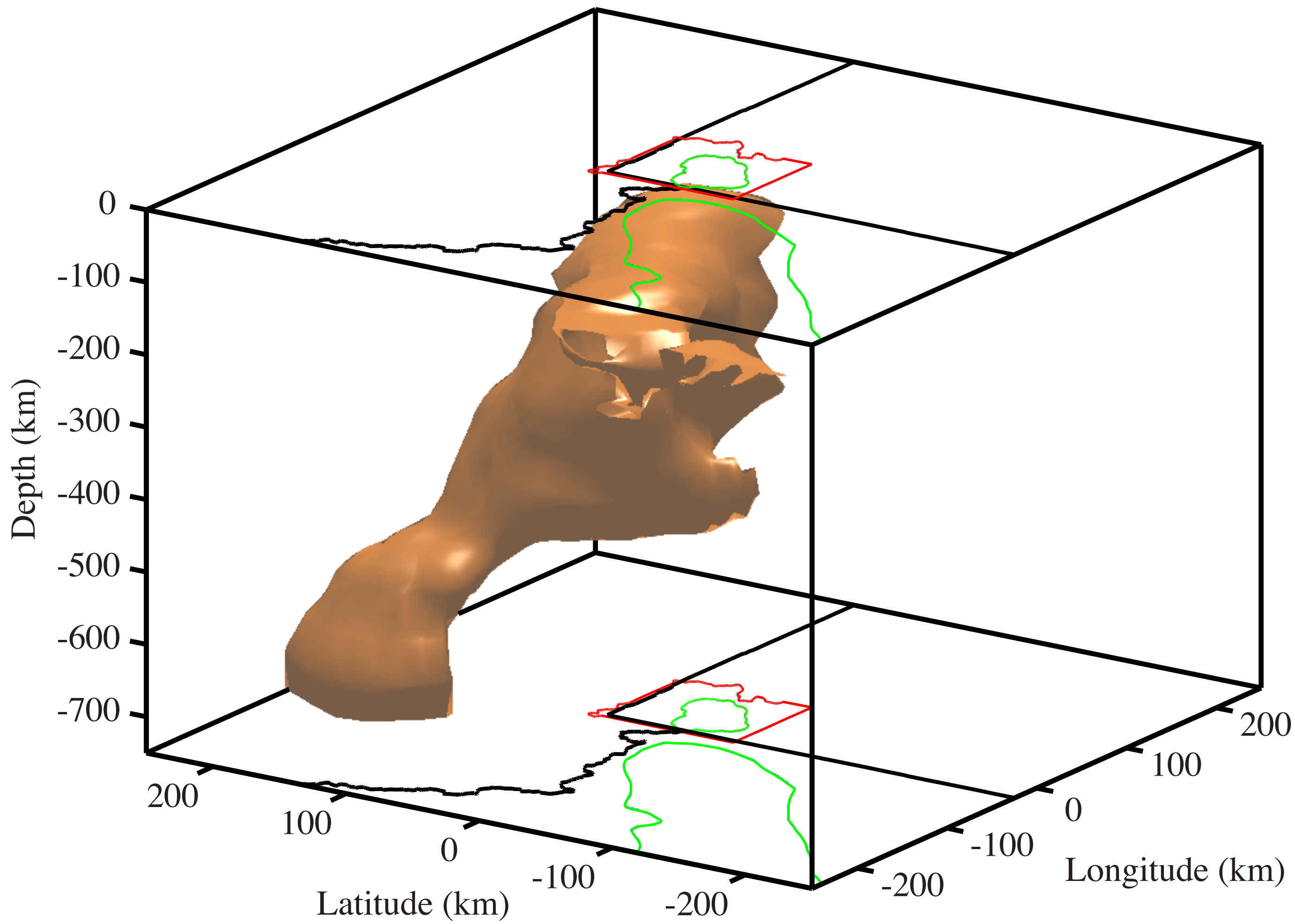
0
-100
-200
-300
-400
-500
-600
-700
Depth (km)
200
100
0
-100
-200
Latitude (km)
200
100
0
-100
-200
Longitude (km)

Figure 20

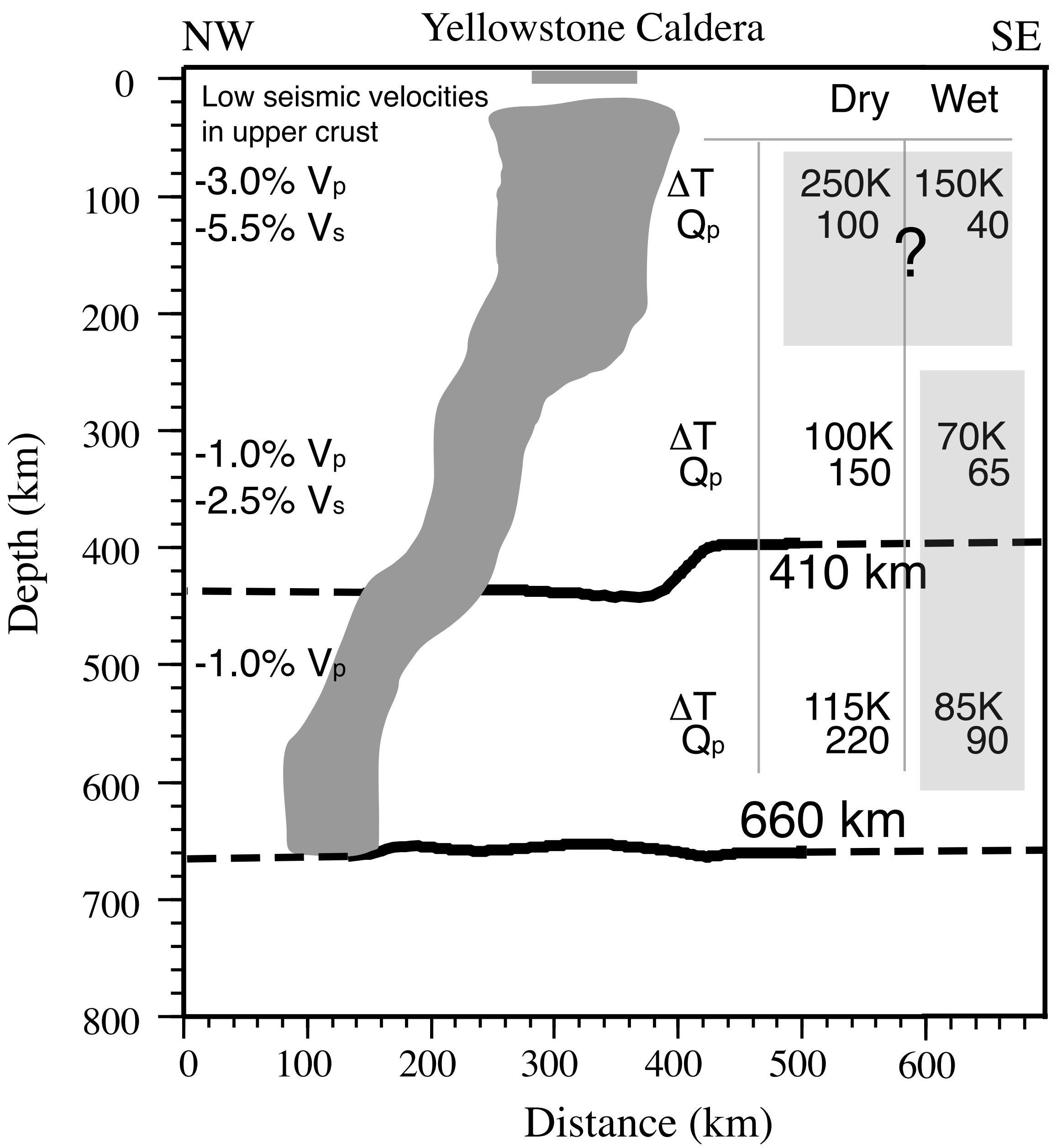
NW
Yellowstone Caldera
SE
Low seismic velocities
in upper crust
-3.0% Vp
-5.5% Vs
-1.0% Vp
-2.5% Vs
-1.0% Vp
Dry
Wet
ΔT
Qp
250K
150K
100
40
?
ΔT
Qp
100K
70K
150
65
410 km
ΔT
Qp
115K
85K
220
90
660 km
Depth (km)
Distance (km)
0
100
200
300
400
500
600
700
800

Figure 21
Click here to download high resolution image

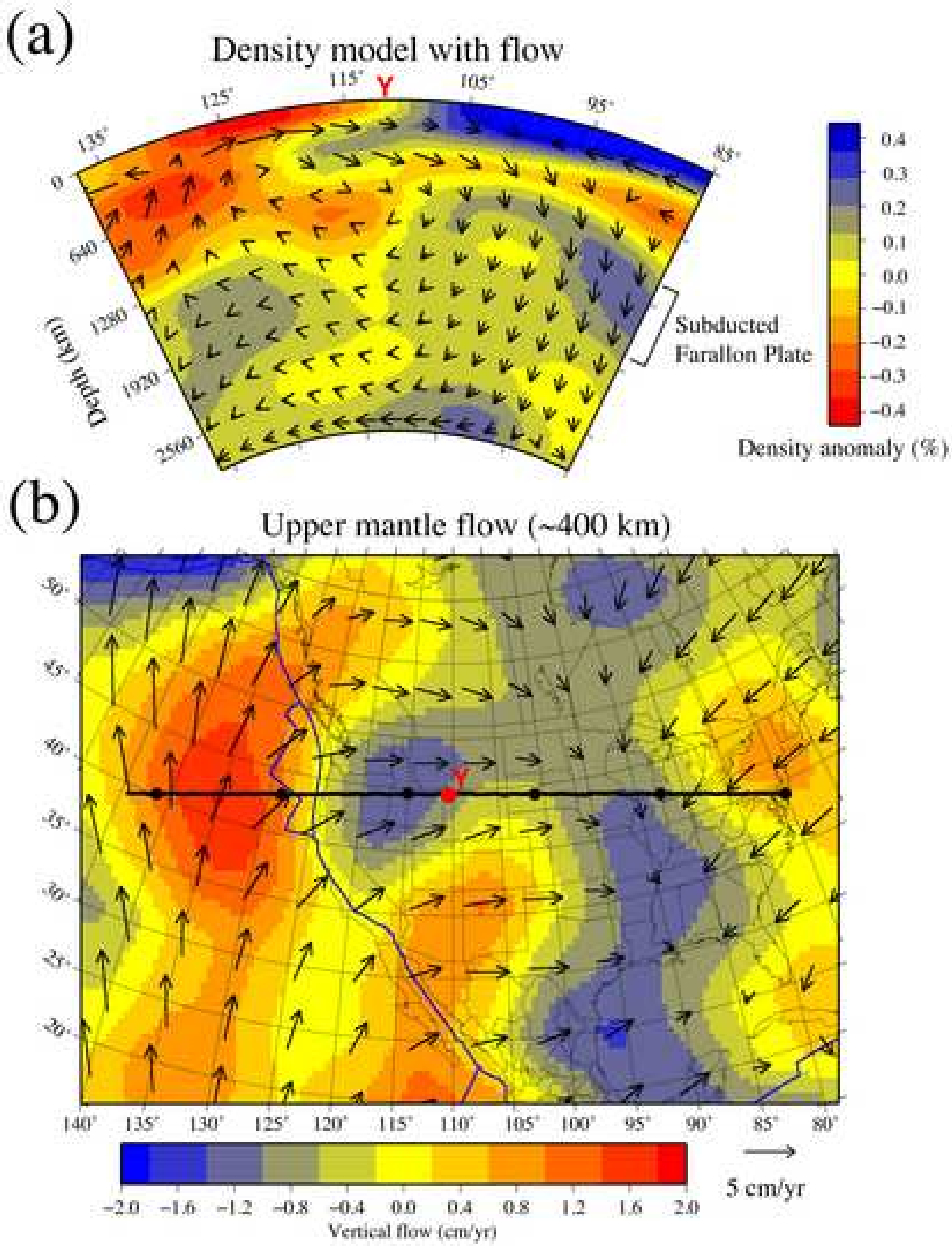

Figure 22

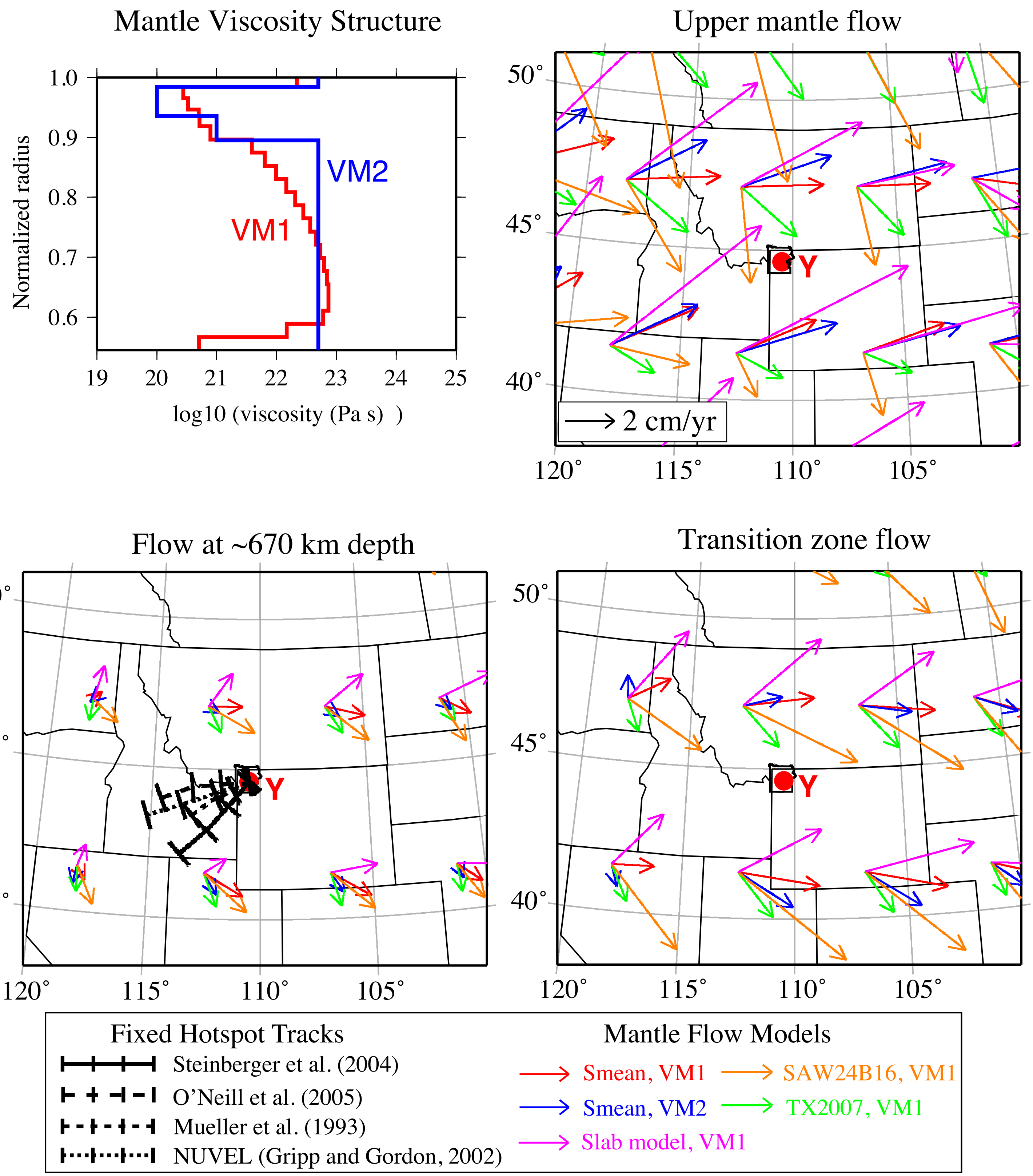

Mantle Viscosity Structure
Normalized radius
log10 (viscosity (Pa s) )
VM1
VM2
Upper mantle flow
2 cm/yr
Y
Flow at ~670 km depth
Transition zone flow
Fixed Hotspot Tracks
Steinberger et al. (2004)
O'Neill et al. (2005)
Mueller et al. (1993)
NUVEL (Gripp and Gordon, 2002)
Mantle Flow Models
Smean, VM1
SAW24B16, VM1
Smean, VM2
TX2007, VM1
Slab model, VM1

Figure 23

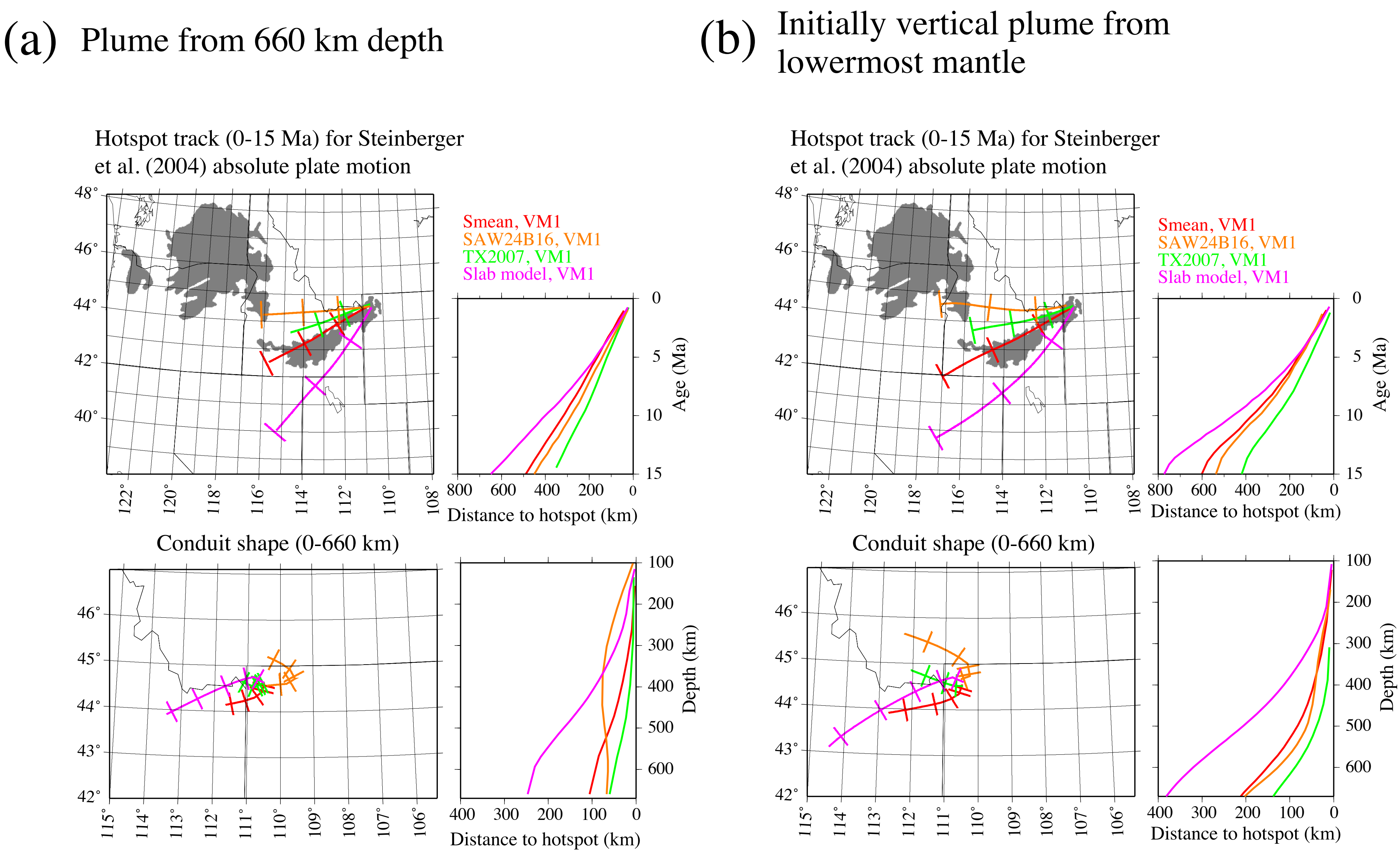

(a) Plume from 660 km depth
(b) Initially vertical plume from lowermost mantle
Hotspot track (0-15 Ma) for Steinberger et al. (2004) absolute plate motion
Smean, VM1
SAW24B16, VM1
TX2007, VM1
Slab model, VM1
Distance to hotspot (km)
Age (Ma)
Conduit shape (0-660 km)
Depth (km)

**Figure 24**

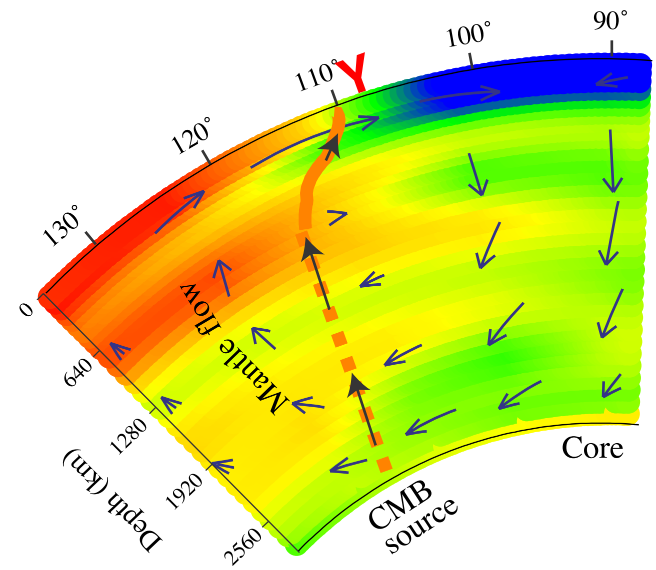

90°
100°
110°
Y
120°
130°
0
640
1280
1920
2560
Depth (km)
Mantle flow
Core
CMB
source

Figure 25

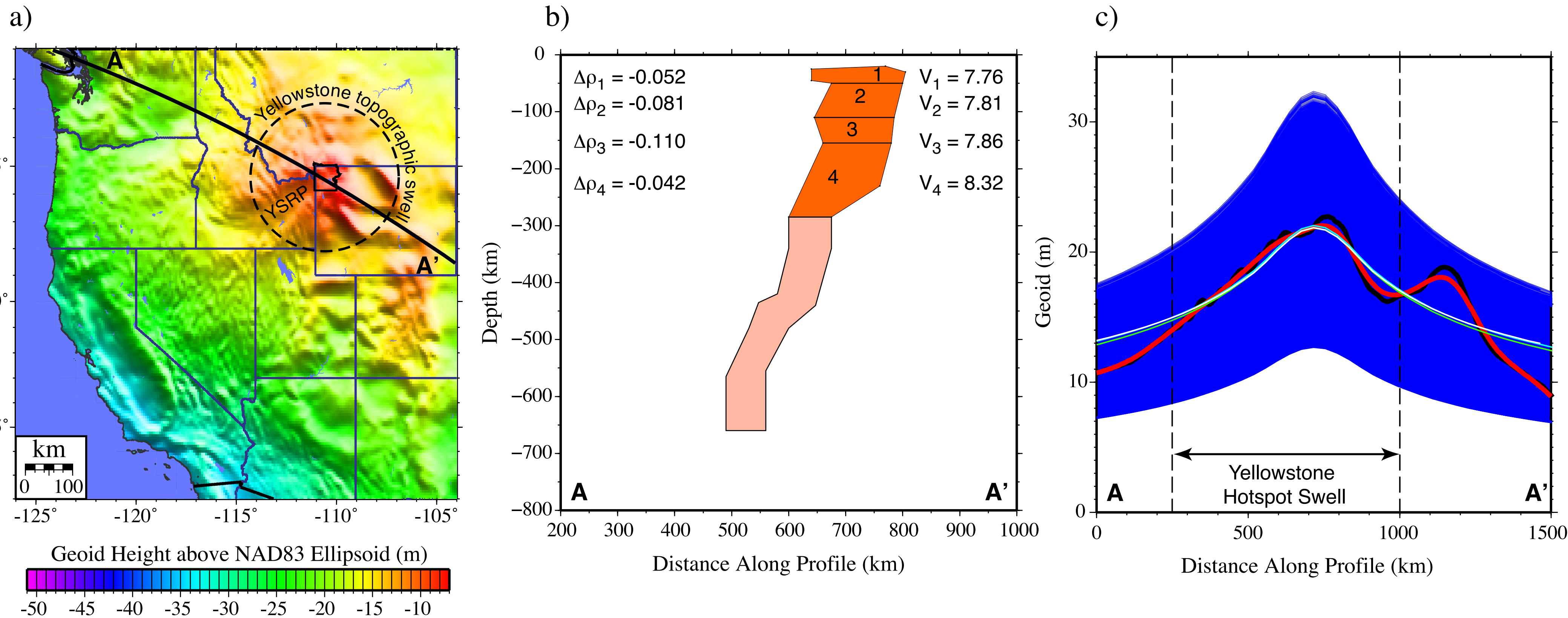
a)
A
A'
Yellowstone topographic swell
YSRP
km
0 100
45°
40°
35°
-125°
-120°
-115°
-110°
-105°
Geoid Height above NAD83 Ellipsoid (m)
-50 -45 -40 -35 -30 -25 -20 -15 -10
b)
Δρ1 = -0.052
Δρ2 = -0.081
Δρ3 = -0.110
Δρ4 = -0.042
V1 = 7.76
V2 = 7.81
V3 = 7.86
V4 = 8.32
1
2
3
4
Depth (km)
Distance Along Profile (km)
A
A'
c)
Geoid (m)
Yellowstone Hotspot Swell
A
A'
Distance Along Profile (km)

Figure 26

Click here to download high resolution image

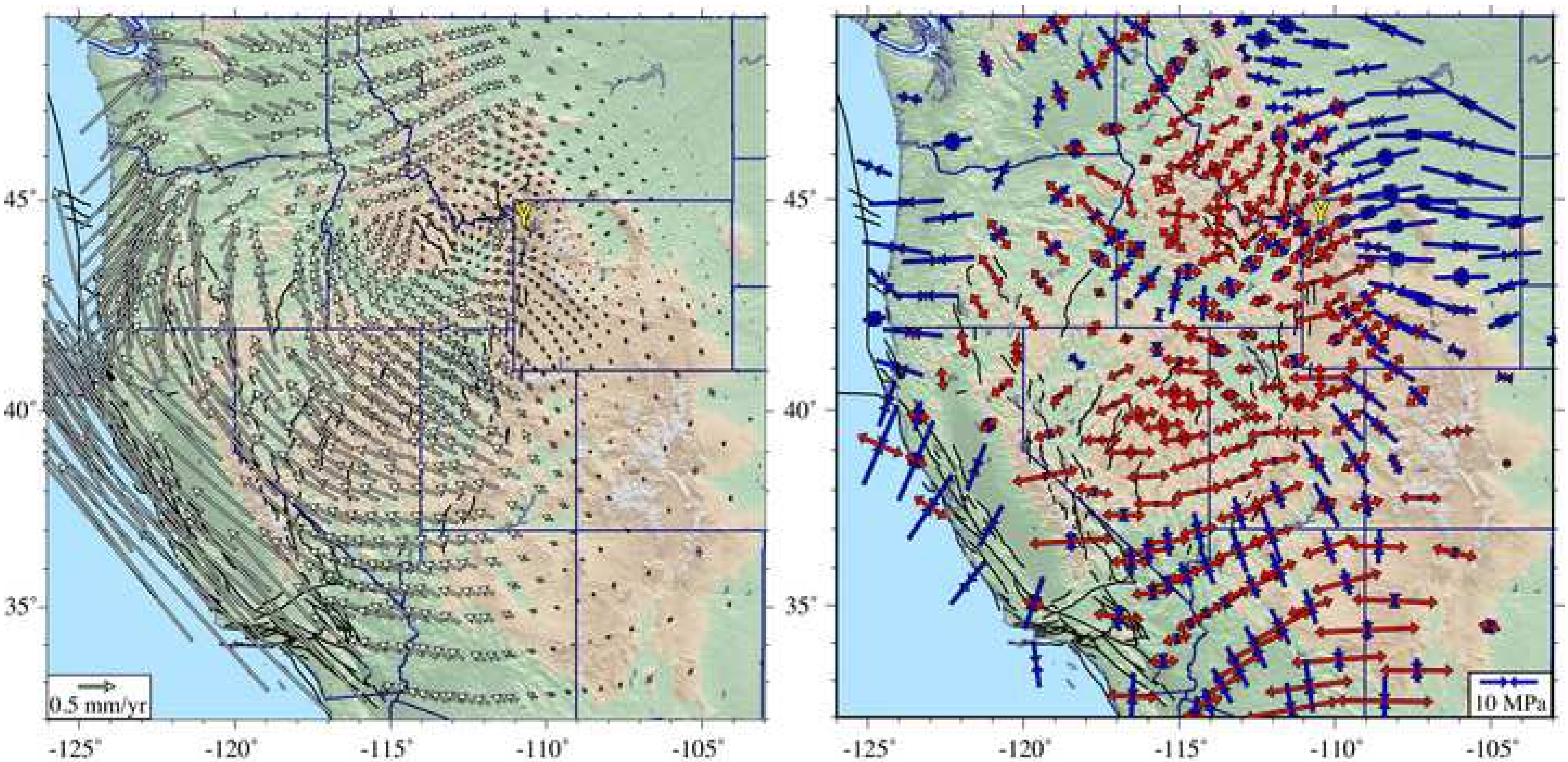

Figure 27

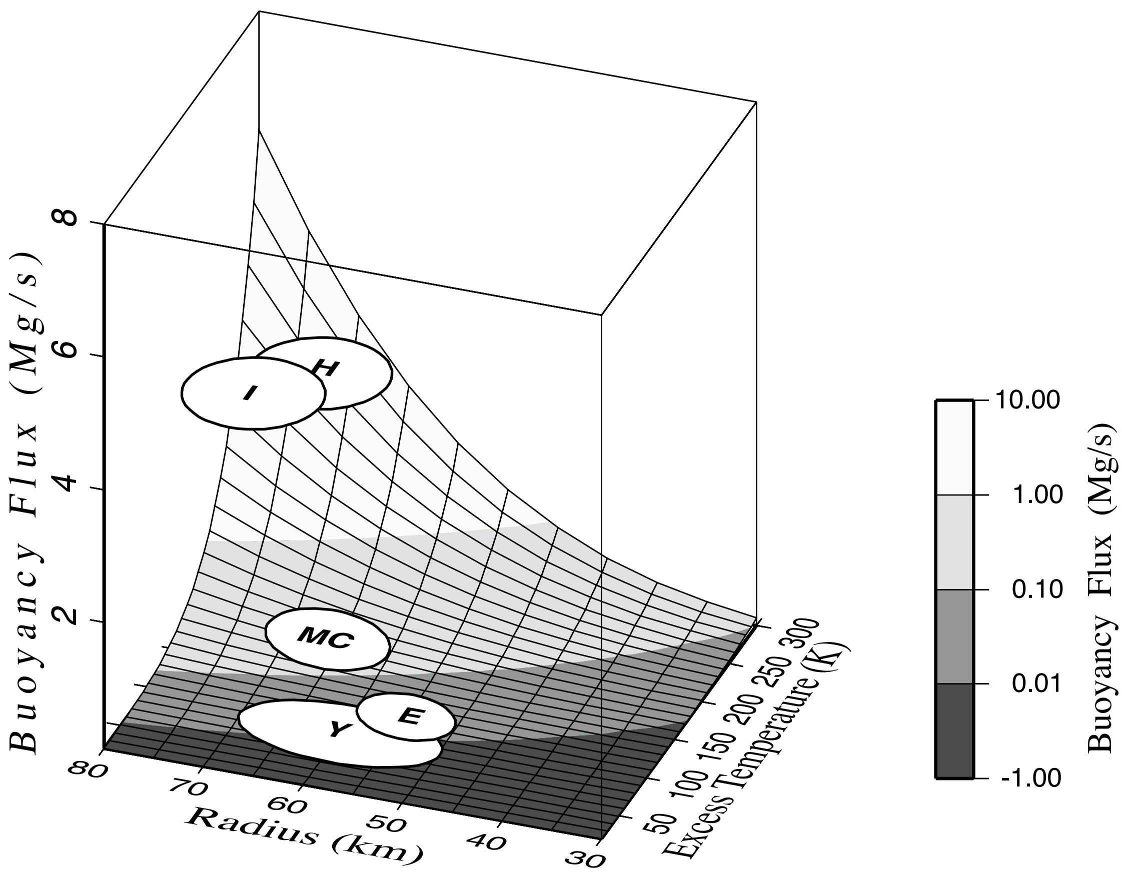

Buoyancy Flux (Mg/s)
8
6
4
2
H
I
MC
E
Y
80
70
60
50
40
30
Radius (km)
50
100
150
200
250
300
Excess Temperature (K)
10.00
1.00
0.10
0.01
-1.00
Buoyancy Flux (Mg/s)

**Figure 28**

a)

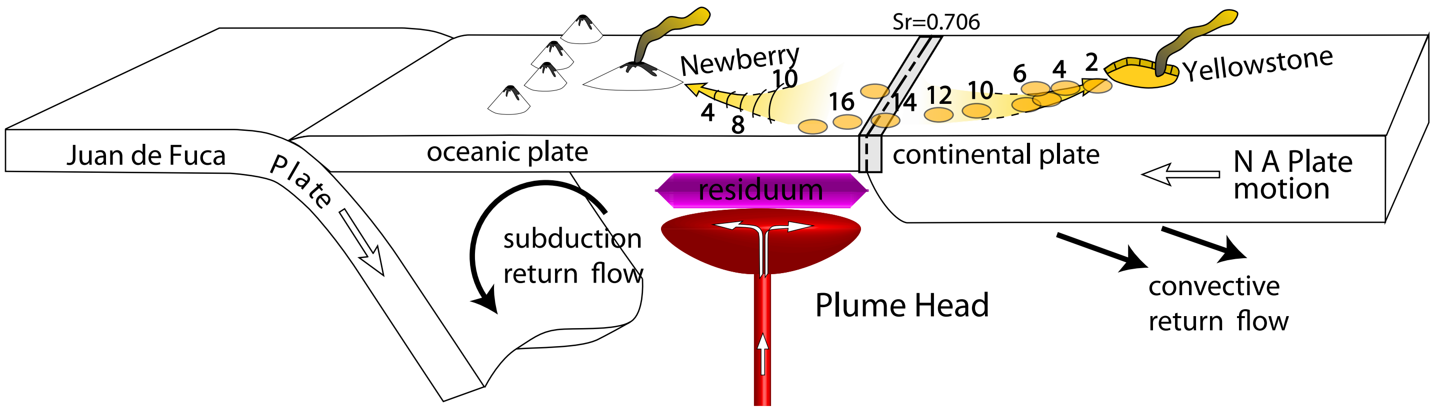
Sr=0.706
Newberry
10
4
8
16
14
12
10
6
4
2
Yellowstone
Juan de Fuca
Plate
oceanic plate
continental plate
N A Plate
motion
residuum
subduction
return flow
Plume Head
convective
return flow

b)

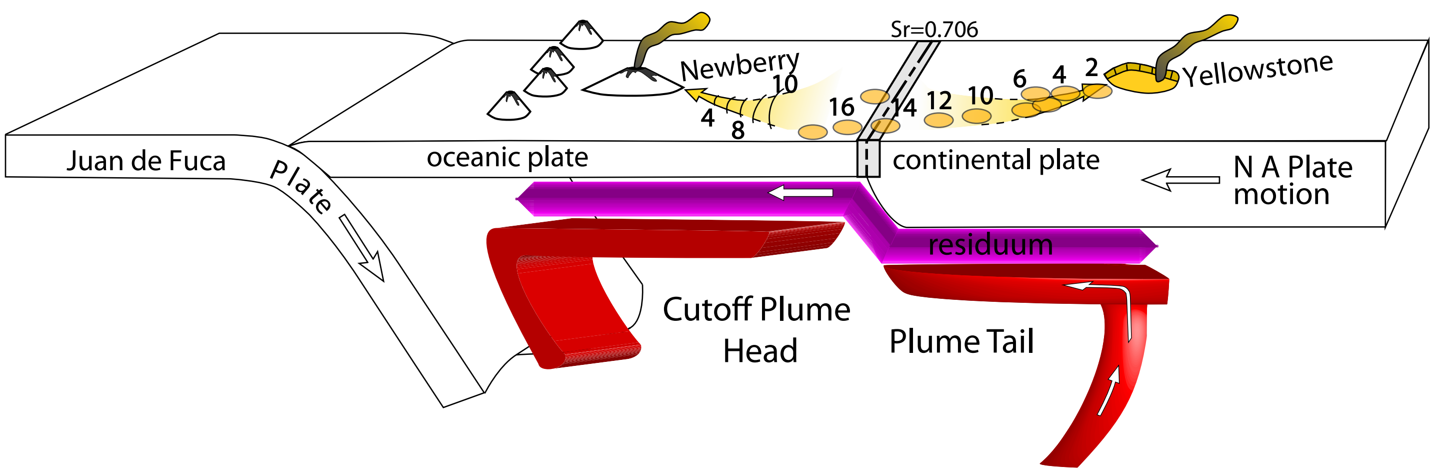
Sr=0.706
Newberry
10
4
8
16
14
12
10
6
4
2
Yellowstone
Juan de Fuca
Plate
oceanic plate
continental plate
N A Plate
motion
residuum
Cutoff Plume
Head
Plume Tail

Figure 29

Click here to download high resolution image

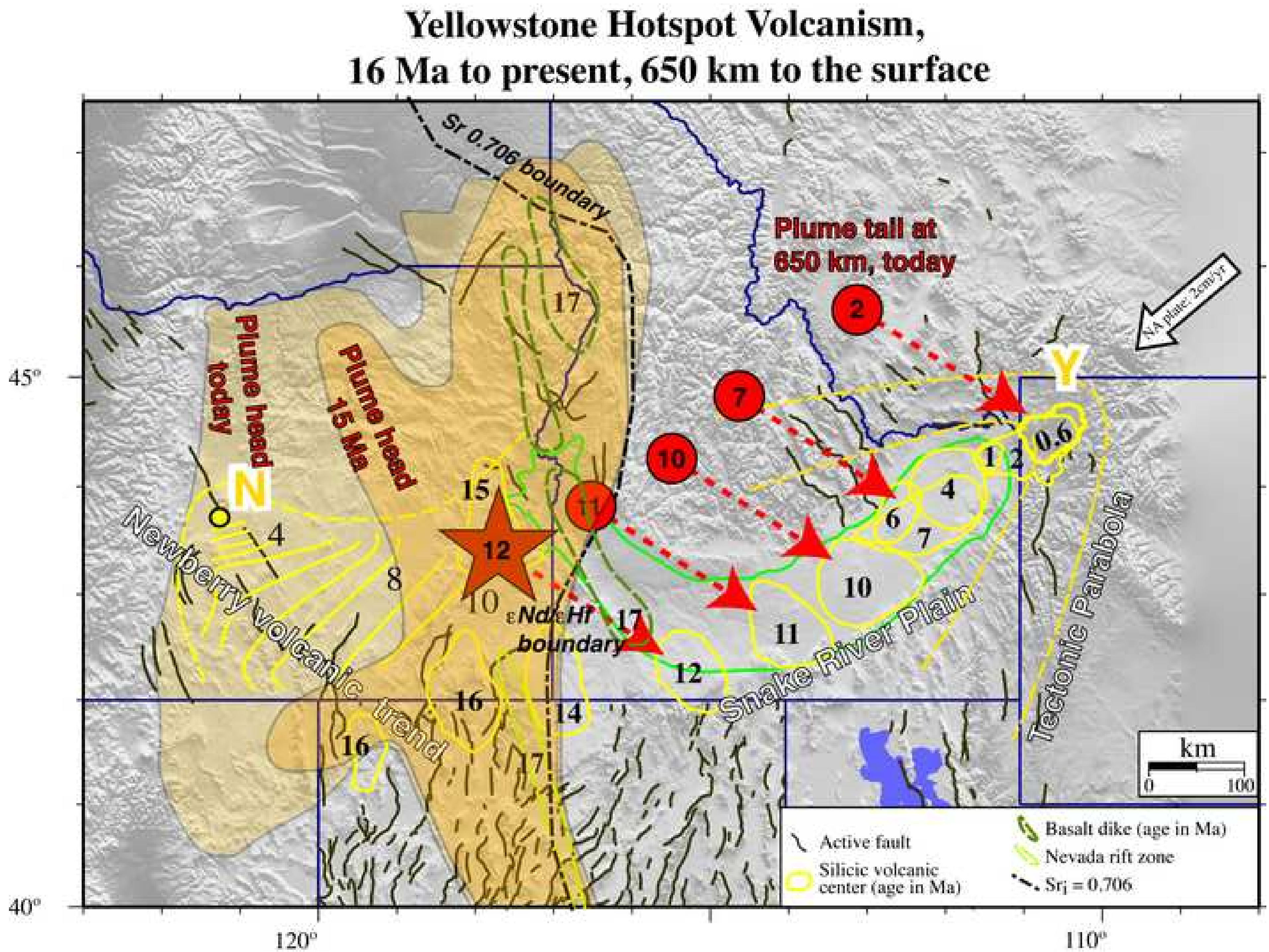

Table 01
Click here to download Table: Table01_Bvalues.pdf

**Table 1.**

| Body # | depth min [km] | depth max [km] | B Model 1 | Δρ [kg/dm³] Model 1 | B Model 500 | Δρ [kg/dm³] model 500 | B Model 1000 | Δρ [kg/dm³] Model 10000 |
|---|---|---|---|---|---|---|---|---|
| 1 | 25 | 50 | 4.6 | -0.052 | 4.0 | -0.060 | 3.4 | -0.071 |
| 2 | 50 | 110 | 3.0 | -0.081 | 3.2 | -0.076 | 3.8 | -0.064 |
| 3 | 110 | 155 | 2.2 | -0.110 | 2.6 | -0.093 | 3.0 | -0.081 |
| 4 | 155 | 285 | 2.0 | -0.042 | 2.2 | -0.038 | 3.2 | -0.026 |

Figure s1

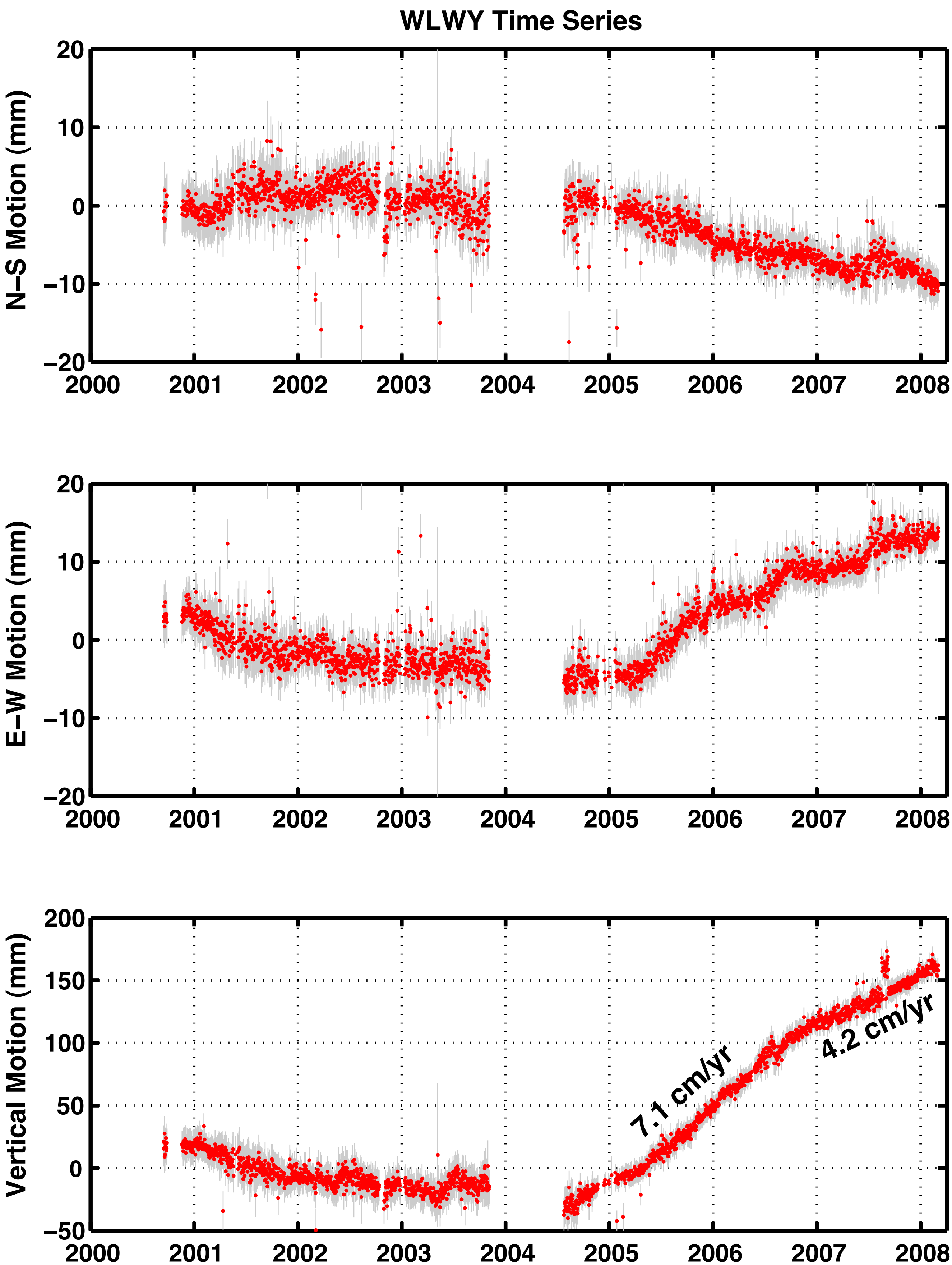
WLWY Time Series
N–S Motion (mm)
20
10
0
−10
−20
2000
2001
2002
2003
2004
2005
2006
2007
2008
E–W Motion (mm)
20
10
0
−10
−20
2000
2001
2002
2003
2004
2005
2006
2007
2008
Vertical Motion (mm)
200
150
100
50
0
−50
2000
2001
2002
2003
2004
2005
2006
2007
2008
7.1 cm/yr
4.2 cm/yr

Figure s2

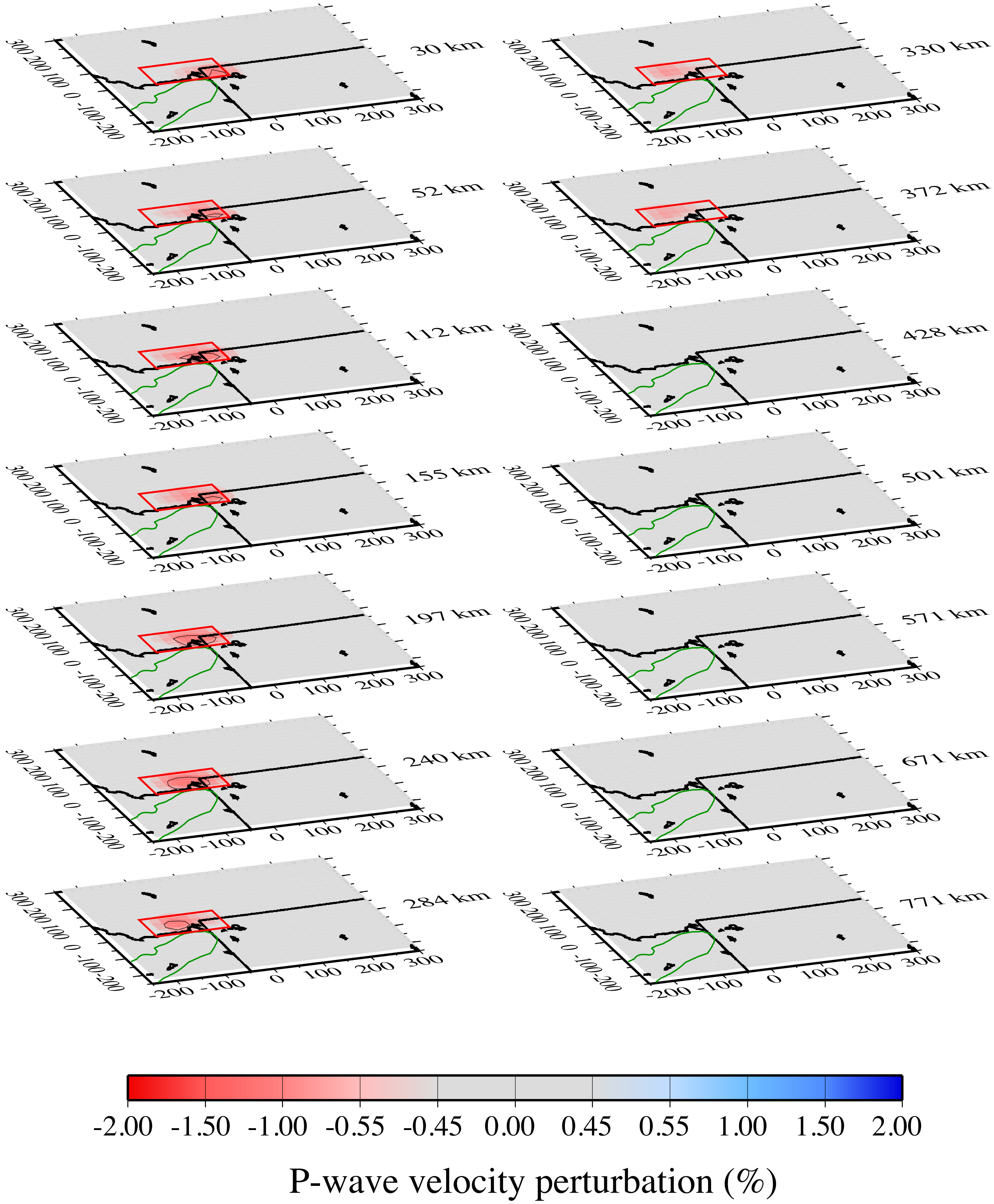
30 km
52 km
112 km
155 km
197 km
240 km
284 km
330 km
372 km
428 km
501 km
571 km
671 km
771 km
-2.00 -1.50 -1.00 -0.55 -0.45 0.00 0.45 0.55 1.00 1.50 2.00
P-wave velocity perturbation (%)

Figure s3

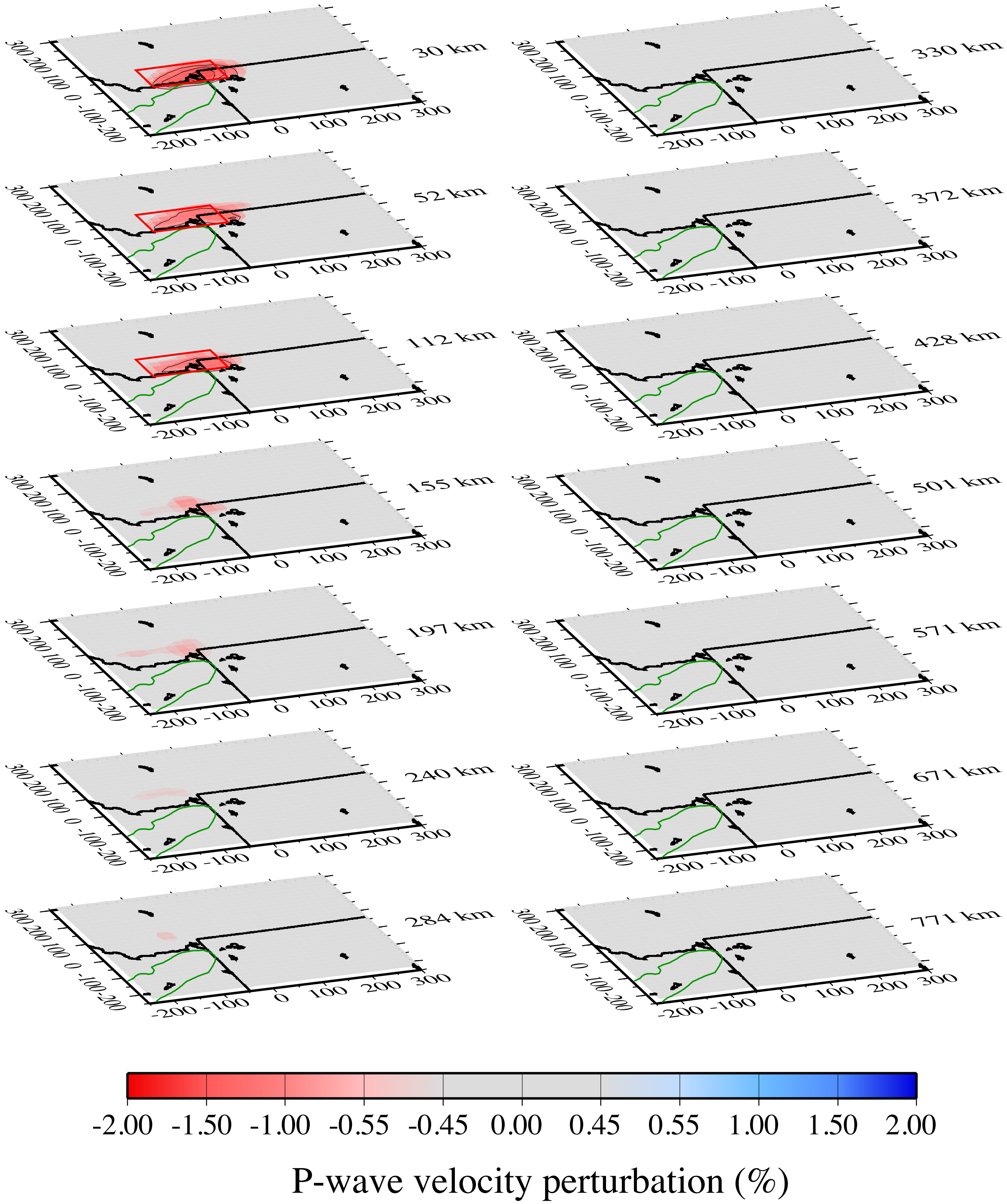

30 km
52 km
112 km
155 km
197 km
240 km
284 km
330 km
372 km
428 km
501 km
571 km
671 km
771 km
-2.00 -1.50 -1.00 -0.55 -0.45 0.00 0.45 0.55 1.00 1.50 2.00
P-wave velocity perturbation (%)

Figure s4

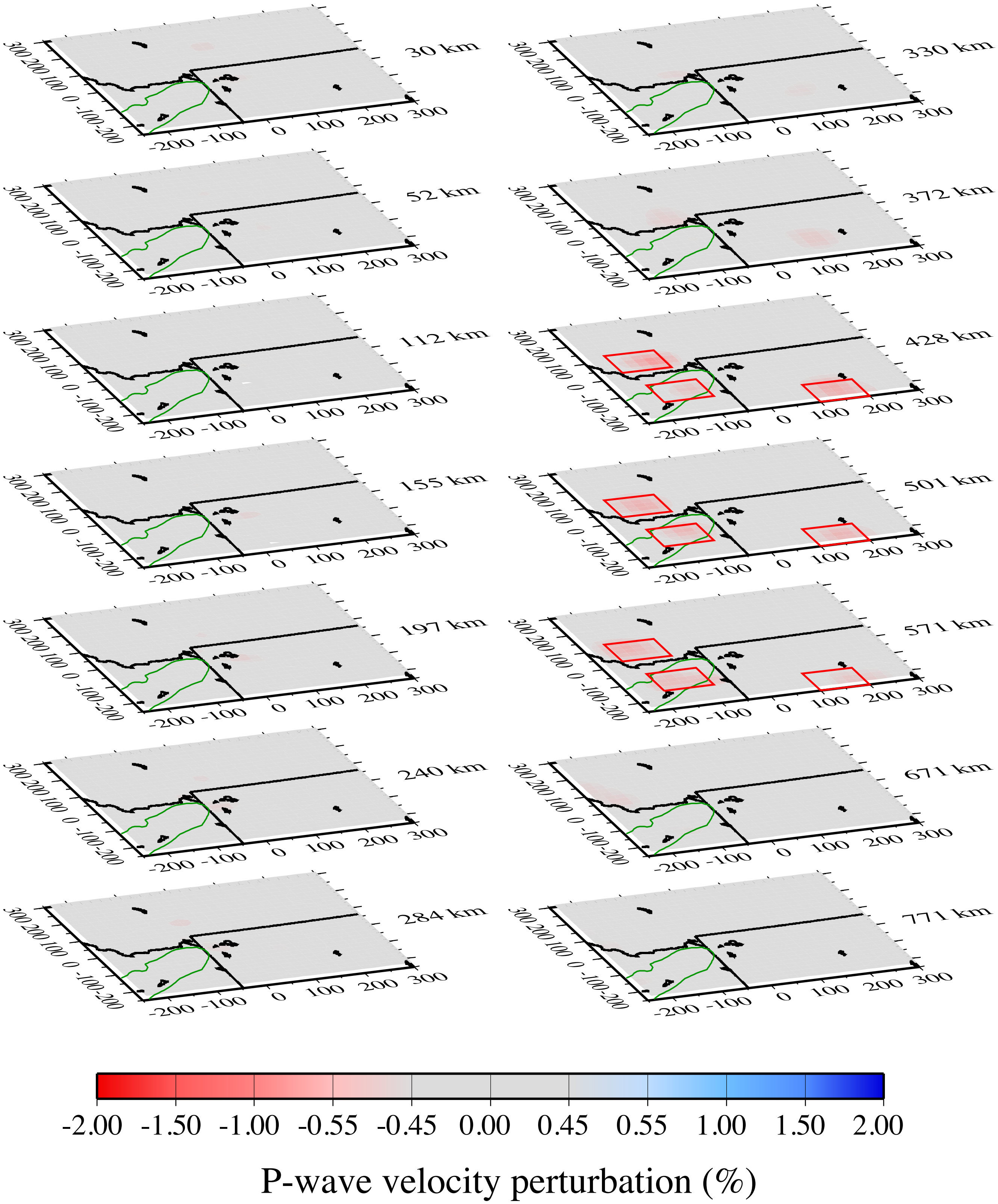
30 km
52 km
112 km
155 km
197 km
240 km
284 km
330 km
372 km
428 km
501 km
571 km
671 km
771 km
-2.00 -1.50 -1.00 -0.55 -0.45 0.00 0.45 0.55 1.00 1.50 2.00
P-wave velocity perturbation (%)

Figure s5

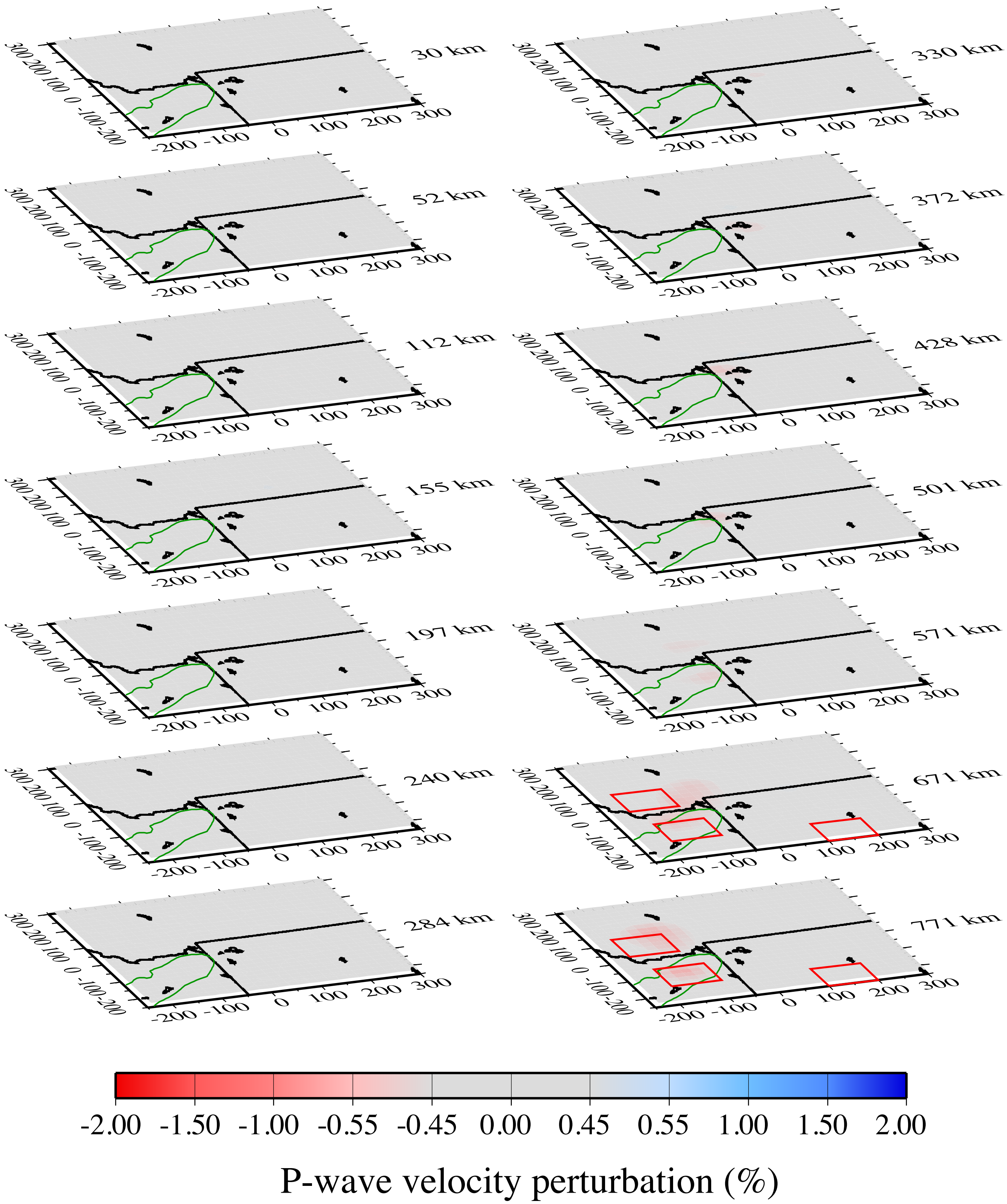
30 km
52 km
112 km
155 km
197 km
240 km
284 km
330 km
372 km
428 km
501 km
571 km
671 km
771 km
-200 -100 0 100 200 300
300 200 100 0 -100 -200
-2.00 -1.50 -1.00 -0.55 -0.45 0.00 0.45 0.55 1.00 1.50 2.00
P-wave velocity perturbation (%)

Figure s6

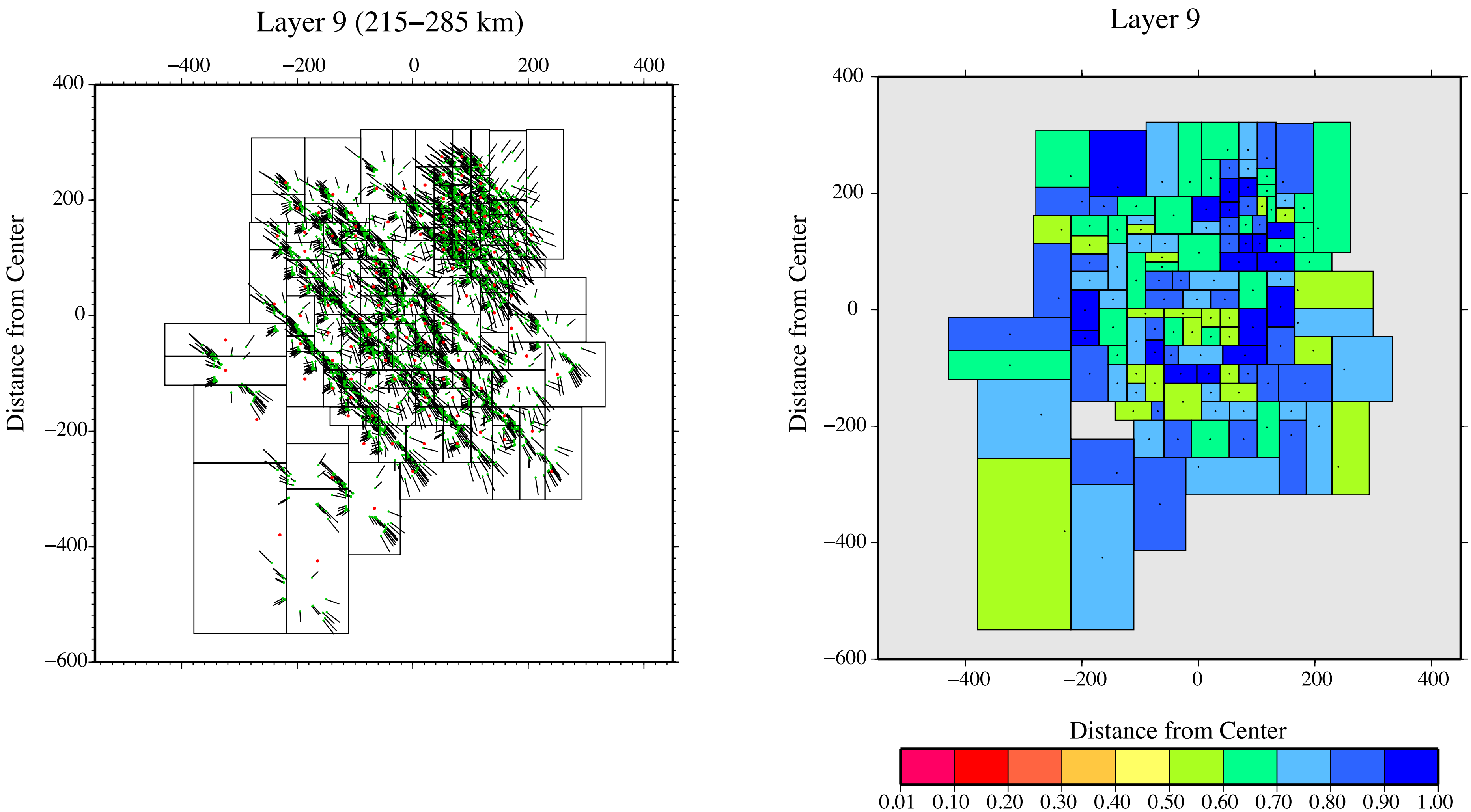
Layer 9 (215–285 km)
Distance from Center
400
200
0
−200
−400
−600
−400
−200
0
200
400
Layer 9
Distance from Center
400
200
0
−200
−400
−600
−400
−200
0
200
400
Distance from Center
0.01
0.10
0.20
0.30
0.40
0.50
0.60
0.70
0.80
0.90
1.00